

Scuola di Scienze
Dipartimento di Fisica e Astronomia
Corso di Laurea Magistrale in Fisica

Search for CP violation with the
singly-Cabibbo-suppressed decays
 $D^+ \rightarrow \phi\pi^+$ and $D_s^+ \rightarrow K_S^0\pi^+$ at LHCb

Relatore:
Prof. Angelo Carbone

Presentata da:
Alessandro Santucci

Correlatrice:
Dott.ssa Serena Maccolini

Anno Accademico 2019/2020

To my Family

Abstract

In this thesis work is described a preliminary measurement of the search for direct CP-violation in the singly-Cabibbo-suppressed decays $D_s^+ \rightarrow K_s^0 \pi^+$ e $D^+ \rightarrow \phi \pi^+$ reconstructed using proton-proton collision recorded by the LHCb detector at a centre-of-mass energy of 13 TeV during the 2018 data taking campaign. The analysed data correspond to an integrated luminosity of about 2 fb^{-1} . The measurements of the CP asymmetries, A_{CP} , are determined from the so-called raw asymmetries obtained from fits to the invariant mass distribution of the Cabibbo-suppressed $D_s^+ \rightarrow K_s^0 \pi^+$ and $D^+ \rightarrow \phi \pi^+$ decays. The adopted fitting model is obtained by studying a large data sample of simulated events and represents a novelty for this measurement. Thanks to this study, the systematic uncertainties related to the fitting model improves with respect to the previous analysis performed by LHCb on a different data sample. The values of A_{CP} are determined using the Cabibbo favourite $D^+ \rightarrow K_s^0 \pi^+$ and $D_s^+ \rightarrow \phi \pi^+$ decays. Given that A_{CP} can be considered negligible, these decays allow to constrain the D^+ production and the π^+ detection asymmetries. The final results are

$$\begin{aligned} A_{CP}(D_s^+ \rightarrow \phi \pi^+) &= -(0.57 \pm 0.04)\% \\ A_{CP}(D_s^+ \rightarrow K_s^0 \pi^+) &= -(0.07 \pm 0.25)\% \end{aligned}$$

where the central values are blind, i.e. biased by a random shift, as this analysis still needs to be reviewed by the LHCb collaboration before being published. The errors reported are only statistical. The systematic uncertainties are discussed, but not evaluated as this study is beyond the aim of the thesis work.

Sommario

Il lavoro riportato in questa tesi descrive una misura preliminare di ricerca violazione CP diretta mediante i decadimenti Cabibbo soppressi $D_s^+ \rightarrow K_s^0 \pi^+$ e $D^+ \rightarrow \phi \pi^+$ realizzata analizzando le collisioni protone-protone ad un'energia nel centro di massa di 13 TeV, corrispondenti ad una luminosità integrata di circa 2 fb^{-1} . I dati analizzati sono stati rivelati dall'esperimento LHCb durante la presa dati del 2018. Le misure delle asimmetrie di CP , A_{CP} , sono determinate dalle cosiddette asimmetrie raw ottenute dall'adattamento ai dati di funzioni che descrivono le distribuzioni di massa invariante dei decadimenti $D_s^+ \rightarrow K_s^0 \pi^+$ e $D^+ \rightarrow \phi \pi^+$. Il modello di adattamento ai dati è stato ottenuto tramite lo studio di un grande campione di dati Monte Carlo. Questo studio ha permesso un miglioramento delle incertezze sistematiche legate al modello di fit rispetto alla stessa analisi realizzata da LHCb con un campione di dati diverso. I valori di A_{CP} sono determinati grazie ai campioni di controllo, necessari a determinare le asimmetrie di produzione e di rivelazione. I decadimenti meglio indicati per cancellare queste asimmetrie sono i Cabibbo favoriti $D^+ \rightarrow K_s^0 \pi^+$ e $D_s^+ \rightarrow \phi \pi^+$, essendo la violazione di CP , in questi decadimenti, attesa essere trascurabile. I risultati finali sono

$$\begin{aligned} A_{CP}(D_s^+ \rightarrow \phi \pi^+) &= -(0.57 \pm 0.04)\% \\ A_{CP}(D_s^+ \rightarrow K_s^0 \pi^+) &= -(0.07 \pm 0.25)\% \end{aligned}$$

dove il valore centrale è volutamente alterato da una variazione casuale poichè questa analisi ancora necessita di essere revisionata dalla collaborazione LHCb prima di essere pubblicata. Gli errori riportati sono solo statistici. Le incertezze sistematiche sono state discusse, ma non valutate non essendo questo studio previsto nel lavoro di tesi.

Contents

Introduction	6
1 CP-violation in charm sector	7
1.1 Preface	7
1.2 The Glashow-Winberg-Salam model	8
1.3 CKM Quark-Mixing-Matrix	12
1.4 Phenomenology of CP violation in meson decays	15
1.4.1 Neutral D meson formalism	16
1.4.2 Charm and CP violation	19
1.4.3 Search for CP violation in the $D^+ \rightarrow \phi\pi^+$ and $D_s^+ \rightarrow K_s^0\pi^+$	19
2 LHCb Experiment	23
2.1 Large Hadron Collider (LHC)	24
2.2 The LHCb Detector	27
2.2.1 Vertex Locator (VELO)	27
2.2.2 The Silicon Tracker (ST)	29
2.2.3 Tracker Station	32
2.2.4 Magnet	33
2.2.5 Tracking algorithm and performances	34
2.2.6 The LHCb particle identification system	36
2.2.7 The calorimeters system	39
2.2.8 The muon system	42
2.2.9 Trigger in LHCb	44
2.2.10 Data management and computing	46
3 Analysis and results	49
3.1 Introduction	49
3.2 Analysis Overview	49

3.3	Data samples and event selection	51
3.4	Cut-based selection and analysis	54
3.5	Selection of the $D_{(s)}^+ \rightarrow K_S^0 \pi^+$	57
3.5.1	Physical background	63
3.6	Selection of the $D_{(s)}^+ \rightarrow \phi \pi^+$	65
3.7	Fit model	67
3.7.1	The Monte Carlo generation	67
3.8	Results	69
3.9	Final Results for CP -violating asymmetries	74
3.10	Systematic Uncertainties	74
3.10.1	K^0 interactions in VELO detector	74
3.10.2	Secondary $D_{(s)}^+$ decays	75
3.10.3	Differences in signal and control channels kinematics	75
	Conclusions	77
	Appendices	78
A	Kinematic separation of $D^\pm \rightarrow K_S^0 h^+$ and $K_S^0 \rightarrow \pi^+ \pi^-$ decays	79

Introduction

The violation of charge conjugation and parity symmetry, i.e. CP -violation, is one of the necessary conditions to explain the matter-antimatter asymmetry observed in the universe. In the Standard Model (SM), CP violation arises from a non-reducible phase into the Cabibbo-Kobayashi-Maskawa matrix (CKM) which describes the transitions within the three families of quark. The amount of CP violation measured so far, cannot explain the presence of observed baryogenesis. For this reason, it's important to continue the research in this complex field. The realization of CP -violation in nature has been well established in the K - and B -mesons system by several experiments and recently its existence has been proved also in the charm sector [1]. In charm decays, CP -violation asymmetries are expected tiny $\sim 10^{-4} \div 10^{-3}$, due to low-energy strong effects. [2] The study of CP -violation in charm transitions is a powerful probe of physics beyond SM theories, in particular when this couples to the up-type quarks. The LHCb experiment offer the largest sample ever of charm hadrons and it is the ideal environments for these searches. CP -violation in the charm sector involves the charmed mesons, i.e. D^0 D^+ and D_s^+ . Among several charm decays, the D mesons decaying into a neutral kaon or ϕ meson coupled with a bachelor hadron, are the most promising. This thesis reports the preliminary studies for the measurements of the CP asymmetries in the Cabibbo suppressed decays, $D^+ \rightarrow K_S^0 \pi^+$, and $D^+ \rightarrow \phi \pi^+$, using a data sample recorded by LHCb during the 2018 data taking campaign, corresponding to an integrated luminosity of 2 fb^{-1} . This thesis uses, moreover, control channels the Cabibbo-favoured decays, such as $D^+ \rightarrow K_S^0$ and $D_s^+ \rightarrow \phi \pi^+$ (where CP violation is expected to be negligible) to eliminate most of systematic uncertainties. (see Section 3).

This thesis is structured as follows. In the first Chapter, a brief description of historical and theoretical aspects related to this measurement is reported. The second Chapter a description of all the components of the LHCb experiment and the apparatus needed to collect data for the analysis is given. The third Chapter describes in detail the analysis method and the final results with the conclusions.

Chapter 1

CP-violation in charm sector

1.1 Preface

Nature is governed by the concept of symmetries. In a physical systems it is possible to define discrete symmetries, such as temporal inversion (T), parity (P) and charge current (C) conjugations. The concept of parity, or space inversion, is related to a transformation of an object, in which the coordinates are reflected. Charge conjugation is a mathematical operation that transforms a particle into its antiparticle, inverting the sign of all charges while leaving unaffected the other quantities. Moreover, the last but not least important symmetry is the time reversal. This transformation permits the inversion of time.

Before the early 50's, it was assumed that the C, P and T transformations were symmetric for electromagnetic and strong interactions. However, some discoveries profoundly changed our knowledge. The discovery of parity violation in the weak interactions in 1956 certainly falls into this illustrious category. In 1964 The discovery of CP -violation in neutral kaon system by Christenson, Cronin, Fitch and Turlay at Brookhaven National Lab (BNL) that established the new paradigm that even in microscopic regime symmetries should not be assumed to hold a priori, but have to be subject to determined experimental scrutiny [3]. At that time, C and P symmetry were incorporated in the basic structure of the electroweak theory, represented by the $SU(2)_L \otimes U(1)_Y$ group. The theory was originally proposed by Glashow Weinberg and Salam to describe the leptons and then extended to the quarks by Nicola Cabibbo, in 1963, by introducing the homonymous angle θ_C , to explain electroweak interaction including the strange quark. In this theory the object that couples with the up quarks is described as the superposition of down states of different families (*i.e.* $d = d \cos \theta_C + s \sin \theta_C$). This theoretical extension permits the universality of weak interactions [4, 5]. Few years later, in 1970, Glashow, Iliopoulos and

Maiani proposed to explain the non observation of Flavour Changing Neutral Current (FCNC), processes with the existence of a fourth quark, the charm (GIM mechanism). Before the 1973, the model has no explanation for the K mesons behaviour. These particles, in fact, are formed by strong interactions, but decay weakly. This is due by the strangeness, a quantum number conserved in strong and electromagnetic interactions, but not in weakness ones [6]. That was, however, an open problem until Kobayashi and Maskawa noticed that CP -violation could be allowed in the electroweak interactions introducing a complex phase in the Cabibbo-Kobayashi-Maskawa matrix (CKM) governing the quark mixing. [7]. The effective existence of the charm and bottom quarks were established after few years, respectively in 1974 at SLAC and BNL [8, 9], and 1977 at Fermilab [10], moreover the top quark (an up-like quark) was observed for the first time, in 1995 at Fermilab [11]. An important discovery was the observation of mixing in the neutral B system by ARGUS collaboration in 1987 [12]. Only after several years, two collaborations BABAR at SLAC and Belle at KEK, have independently established CP -violation in the B^0 system.

CP -violation is of particular interest because it could reveal the presence of New Physics beyond Standard Model. This aspects has a great importance in cosmology whereas violation could be connected to baryon asymmetry. SM predictions, reveal that CP -violation is too smaller to explain the absence of anti-matter in the universe. Several extensions of the SM, foresees other sources of CP -violation, hence any observation, in principle, could be a sign of New Physics [13]. It is therefore essential to understand, at this time, the picture of CP -violation arising in the framework of Standard Model, where the Kobayashi–Maskawa mechanism plays a key role.

1.2 The Glashow-Winberg-Salam model

The Glashow-Weinberg-Salam (GWS) model is a Yang-Mills non-abelian quantum field theory based on the $SU(2) \times U(1)$ gauge symmetry group, and provides a unified and experimentally established picture of electroweak interactions. The Standard Model (SM) of particle physics is obtained expanding the GWS model with the $SU(3)$ symmetry of strong interactions and the Brout-Englert-Higgs spontaneous symmetry breaking mechanism. The SM describes all the known elementary particles (quarks, leptons, fermions, gauge and Higgs bosons) and their fundamental interactions, with the exception of gravity. The Lagrangian of the GWS model can be divided into four main terms [4].

$$\mathcal{L} = \mathcal{L}_B + \mathcal{L}_f + \mathcal{L}_H + \mathcal{L}_Y. \quad (1.1)$$

Here \mathcal{L}_B is the kinetic term of the four gauge fields: W_μ^a (the weak isospin fields with $(a = 1, 2, 3)$) and B_μ (the hypercharge field). Denoting $W_{\mu\nu}^a$ and $B_{\mu\nu}$ as their field strength tensors, this term is equal to

$$\mathcal{L}_B = -\frac{1}{4}W^{a\mu\nu}W_{\mu\nu}^a - \frac{1}{4}B^{\mu\nu}B_{\mu\nu}. \quad (1.2)$$

The second term describes the kinetics of the fermions and how they interact with the gauge bosons

$$\mathcal{L}_f = \bar{Q}^j i \not{D}_L Q^j + \bar{u}_R^j i \not{D}_R u_R^j + \bar{d}_R^j i \not{D}_R d_R^j + \bar{L}^j i \not{D}_L L^j + \bar{e}_R^j i \not{D}_R e_R^j, \quad (1.3)$$

where Q^j are the left-handed SU(2) quark doublets, u_R^j and d_R^j are the up and down right-handed quark singlets, while L^j are the left-handed lepton doublets and e_R^j the right-handed charged-lepton singlets. The contracted form $\not{D} = \gamma^\mu D_\mu$ is used, where γ^μ is the Dirac matrix. The explicit form of the doublets involves the left-handed fields u_L^j , d_L^j , ν_L^j and e_L^j

$$Q^j = \begin{pmatrix} u_L^j \\ d_L^j \end{pmatrix}, \quad (1.4)$$

$$L^j = \begin{pmatrix} \nu_L^j \\ e_L^j \end{pmatrix}. \quad (1.5)$$

In Eq. 1.3, a sum over j is assumed, where j is the flavour (or generation) index, which runs from 1 to 3. The presence of $D_{L\mu}$ and $D_{R\mu}$, that are the covariant derivatives for the left-handed and right-handed fermion fields, is needed to keep the Lagrangian invariant under the SU(2) \times U(1) local gauge transformation. The covariant derivatives are defined differently depending on which field they are applied to

$$D_{L\mu} = \partial_\mu + igW_\mu^a \frac{\sigma^a}{2} + ig' \frac{Y}{2} B_\mu, \quad (1.6a)$$

$$D_{R\mu} = \partial_\mu + ig' \frac{Y}{2} B_\mu, \quad (1.6b)$$

where Y is the hypercharge of the field on which D_μ operates, σ^a are the Pauli matrices, g and g' are the coupling constants.

Since Q^j and L^j are SU(2) doublets, they have weak isospin $T = 1/2$, with third component $T_3 = \pm 1/2$ for up- and down-type fields, respectively. The right-handed fermion fields are SU(2) singlets, so they have $T = 0$. The electromagnetic charge Q of a field can be expressed in terms of its hypercharge Y and third component of weak

Table 1.1: Third component of the weak isospin T_3 , hypercharge Y and electromagnetic charge Q of leptons and quarks.

Fermion	T_3	Y	Q
u_L	$1/2$	$1/3$	$2/3$
d_L	$-1/2$	$1/3$	$-1/3$
u_R	0	$4/3$	$2/3$
d_R	0	$-2/3$	$-1/3$
ν_L	$1/2$	-1	0
e_L	$-1/2$	-1	-1
e_R	0	-2	-1

isospin T_3 as

$$Q = \frac{Y}{2} + T_3. \quad (1.7)$$

The values of the hypercharges of all fermionic doublets and singlets can therefore be obtained according to their electromagnetic charge. The values of T_3 , Y and Q of the fermion fields are reported in Table 1.1.

The third term of Eq. 1.1 describes the Higgs field and its coupling with the gauge bosons [14, 15].

$$\begin{aligned} \mathcal{L}_H &= (D^\mu \phi^\dagger)(D_\mu \phi) - V(\phi^\dagger \phi) = \\ &= (D^\mu \phi^\dagger)(D_\mu \phi) - \left(-\mu^2 \phi^\dagger \phi + \frac{\lambda^2}{2} (\phi^\dagger \phi)^2 \right), \end{aligned} \quad (1.8)$$

where λ and μ are positive real parameters and ϕ is the SU(2) Higgs doublet with hypercharge 1

$$\phi = \begin{pmatrix} \phi^+ \\ \phi^0 \end{pmatrix}, \quad (1.9)$$

with ϕ^+ and ϕ^0 electromagnetic charged and neutral complex scalar fields. Since ϕ is a SU(2) doublet with hypercharge 1, the covariant derivative that operates on it is

$$D_\mu = \partial_\mu + igW_\mu^a \frac{\sigma^a}{2} + \frac{1}{2} ig' B_\mu. \quad (1.10)$$

The Yukawa interaction between the fermion fields and ϕ , needed to generate the fermion masses, is given by the last term of Eq. 1.1

$$\mathcal{L}_Y = -\lambda_d^{ij} \bar{Q}^i \phi d_R^j - \lambda_u^{ij} \bar{Q}^i (i\sigma^2 \phi) u_R^j - g_e^i \bar{L}^i \phi e_R^i + \text{h.c.}, \quad (1.11)$$

where a sum over indices i and j is assumed, g_e^i are coupling constants and $\lambda_{d,u}^{ij}$ are general complex-valued matrices.

The Higgs potential $V(\phi^\dagger\phi)$ is at its minimum value when $\phi^\dagger\phi = \mu^2/\lambda^2 \equiv v^2/2$, where $v/\sqrt{2}$ is the vacuum expectation value (VEV) of ϕ ($v \simeq 246$ GeV). The SU(2) gauge invariance allows the four degrees of freedom of ϕ to be reduced to one. Hence the Higgs doublet can be written in the unitarity gauge and expanded around its own VEV

$$\phi = \frac{1}{\sqrt{2}} \begin{pmatrix} 0 \\ v + H(x) \end{pmatrix}, \quad (1.12)$$

where $H(x)$ is the Higgs field, that is scalar and real. In this way a specific direction of vacuum has been chosen, so the symmetry has been spontaneously broken and the Lagrangian is no longer SU(2) invariant.

The physical gauge fields are defined as

$$W_\mu^\pm = \frac{W_\mu^1 \mp iW_\mu^2}{\sqrt{2}}, \quad (1.13a)$$

$$Z_\mu = W_\mu^3 \cos \theta_W - B_\mu \sin \theta_W, \quad (1.13b)$$

$$A_\mu = W_\mu^3 \sin \theta_W + B_\mu \cos \theta_W, \quad (1.13c)$$

where θ_W is the Weinberg angle ($\sin^2\theta_W \simeq 0.23$). The mass terms of the gauge fields are then obtained by substituting Eq. 1.12 in Eq. 1.8

$$-\frac{1}{8}g^2v^2(W^{+\mu}W_\mu^+ + W^{-\mu}W_\mu^-) - \frac{1}{8}v^2(g^2 + g'^2)Z^\mu Z_\mu - \frac{1}{2}\lambda^2v^2H^2. \quad (1.14)$$

From Eq. 1.14 it is apparent that the masses of the gauge and H bosons are

$$M_H = \lambda v, \quad (1.15a)$$

$$M_W = \frac{1}{2}gv, \quad (1.15b)$$

$$M_Z = \frac{1}{2}\sqrt{g^2 + g'^2}v, \quad (1.15c)$$

$$M_\gamma = 0. \quad (1.15d)$$

The three weak bosons acquire mass, while the photon remains massless. By substituting Eq. 1.12 in Eq. 1.11 one obtains

$$\mathcal{L}_Y = -\frac{v}{\sqrt{2}}\lambda_d^{ij}\bar{d}_L^i d_R^j - \frac{v}{\sqrt{2}}\lambda_u^{ij}\bar{u}_L^i u_R^j - \frac{v}{\sqrt{2}}g_e^i e_L^i e_R^i + \text{h.c.}, \quad (1.16)$$

i.e. the mass of e^i is equal to

$$\frac{v}{\sqrt{2}}g_e^i, \quad (1.17)$$

proportional to the coupling between the electron (muon, tau) and the Higgs boson, while the neutrinos remain massless.

1.3 CKM Quark-Mixing-Matrix

The mass and mixing of quarks have a common origin in the Standard Model. They arise from the Yukawa interactions with the Higgs field,

$$\mathcal{L}_Y = -Y_{ij}^d \bar{Q}_{Li}^I \phi d_{Rj}^I - Y_{ij}^u \bar{Q}_{Li}^I \epsilon \phi^* u_{Rj}^I + h.c. \quad (1.18)$$

where $Y^{u,d}$ are 3×3 complex matrices, ϕ is the Higgs field, i, j are generators labels, and ϵ is the 2 antisymmetric tensor. Q_L^I are left handed quark doublets, d_{Rj}^I and u_{Rj}^I are right handed singlets in weak-eigenstates basis. When ϕ acquires a vacuum expectation values $\langle \phi \rangle = (0, v/\sqrt{2})$, 1.18 yields mass terms to quarks. The mean eigenstates are obtained diagonalizing $Y^{u,d}$ matrix by four unitary matrices called $V_{L,R}^{u,d}$. As a result, the charged current W^\pm boson interact with the u_{Li} and d_{Lk} quarks with couplings given by:

$$\frac{-g}{\sqrt{2}} (\bar{u}_L \quad \bar{c}_L \quad \bar{t}_L) \gamma^\mu W_\mu^\dagger V_{CKM} \begin{pmatrix} d_L \\ s_L \\ b_L \end{pmatrix} + h.c. \quad (1.19)$$

$$V_{CKM} = \begin{pmatrix} V_{ud} & V_{us} & V_{ub} \\ V_{cd} & V_{cs} & V_{cb} \\ V_{td} & V_{ts} & V_{tb} \end{pmatrix} \quad (1.19)$$

V_{CKM} is the CKM matrix a 3 unitary matrix [5, 7]. It can be parametrized by three mixing angles and a complex phase [7]. Of the may possible conventions, a standard choice has become:

$$V_{CKM} = \begin{pmatrix} 1 & 0 & 0 \\ 0 & c_{23} & s_{23} \\ 0 & -s_{23} & c_{23} \end{pmatrix} \begin{pmatrix} c_{13} & 0 & s_{13}e^{-i\delta} \\ 0 & 1 & 0 \\ -s_{13}e^{i\delta} & 0 & c_{13} \end{pmatrix} \begin{pmatrix} c_{12} & s_{12} & 0 \\ -s_{12} & c_{12} & 0 \\ 0 & 0 & 1 \end{pmatrix} \quad (1.20)$$

$$= \begin{pmatrix} c_{12}c_{13} & s_{12}c_{13} & s_{13}e^{-i\delta} \\ -s_{12}c_{23} - c_{12}s_{23}s_{13}e^{i\delta} & F_{12}c_{23} - s_{12}s_{23}s_{13}e^{i\delta} & s_{23}c_{13} \\ s_{12}s_{23} - c_{12}c_{23}s_{13}e^{i\delta} & -c_{12}s_{23} - s_{12}c_{23}s_{13}e^{i\delta} & c_{23}c_{13} \end{pmatrix}$$

where $s_{ij} = \sin \theta_{ij}$, $c_{ij} = \cos \theta_{ij}$, and δ is the phase responsible for all CP -violating phenomena in flavour changing processes in the SM. It is known experimentally that $s_{13} \ll s_{23} \ll s_{12} \ll 1$, and it is convenient to exhibit this hierarchy using the Wolfenstein parameterization, i.e. expanding in power of $\lambda = s_{12}$:

$$V_{CKM} = \begin{pmatrix} 1 - \frac{\lambda^2}{2} & \lambda & A\lambda^3(\rho - i\eta) \\ -\lambda^2 & 1 - \frac{\lambda^2}{2} & A\lambda^2 \\ A\lambda^3(1 - \rho - i\eta) & -A\lambda^2 & 1 \end{pmatrix} + (\lambda^4), \quad (1.21)$$

where $\lambda \sim 0.23$, $A \sim 0.81$, $\rho \sim 0.12$ and $\eta \sim 0.36$ are the four CKM parameters [16]. The CKM matrix is almost diagonal, almost symmetric and the matrix elements gets smaller as more they move away from the diagonal. Is possible to define a CP violating quantity in V_{CKM} that is independent of the parameterization [17]. This quantity is called Jarlskg invariant J_{CP} , defined through:

$$\mathfrak{Im} [V_{ij}V_{kl}V_{il}^*V_{kj}^*] = J_{CP} \sum_{m,n=1}^3 \epsilon_{ikm}\epsilon_{jln}, \quad (i, j, k, l = 1, 2, 3) \quad . \quad (1.22)$$

CP is violated only if $J_{CP} \neq 0$. The current experimental value is [16]

$$J_{CP} = (3.04_{-0.20}^{+0.21}) \cdot 10^{-5}. \quad (1.23)$$

The unitary of CKM imposes $\sum_i V_{ij}V_{ik}^* = \delta_{jk}$ and $\sum_i V_{ij}V_{kj}^* = \delta_{ik}$ that leads to a set of nine equations among the matrix elements. The six vanishing combination:

$$\underbrace{V_{ud}V_{us}^*}_{\mathcal{O}(\lambda)} + \underbrace{V_{cd}V_{cs}^*}_{\mathcal{O}(\lambda)} + \underbrace{V_{td}V_{ts}^*}_{\mathcal{O}(\lambda)^5} = 0, \quad (1.24)$$

$$\underbrace{V_{ud}V_{cd}^*}_{\mathcal{O}(\lambda)} + \underbrace{V_{us}V_{cs}^*}_{\mathcal{O}(\lambda)} + \underbrace{V_{ub}V_{cb}^*}_{\mathcal{O}(\lambda)^5} = 0, \quad (1.25)$$

$$\underbrace{V_{us}V_{ub}^*}_{\mathcal{O}(\lambda)^4} + \underbrace{V_{cs}V_{cb}^*}_{\mathcal{O}(\lambda)^2} + \underbrace{V_{ts}V_{tb}^*}_{\mathcal{O}(\lambda)^2} = 0, \quad (1.26)$$

$$\underbrace{V_{cd}V_{td}^*}_{\mathcal{O}(\lambda)^4} + \underbrace{V_{cs}V_{ts}^*}_{\mathcal{O}(\lambda)^2} + \underbrace{V_{cb}V_{td}^*}_{\mathcal{O}(\lambda)^2} = 0, \quad (1.27)$$

$$\underbrace{V_{ud}V_{ub}^*}_{\mathcal{O}(\lambda)^3} + \underbrace{V_{cd}V_{cb}^*}_{\mathcal{O}(\lambda)^3} + \underbrace{V_{td}V_{tb}^*}_{\mathcal{O}(\lambda)^3} = 0, \quad (1.28)$$

$$\underbrace{V_{ud}V_{td}^*}_{\mathcal{O}(\lambda)^3} + \underbrace{V_{us}V_{ts}^*}_{\mathcal{O}(\lambda)^3} + \underbrace{V_{ub}V_{tb}^*}_{\mathcal{O}(\lambda)^3} = 0, \quad (1.29)$$

can be represented as triangles in a complex plane, of which those obtained by taking scalar products of neighboring rows or columns are nearly degenerate.

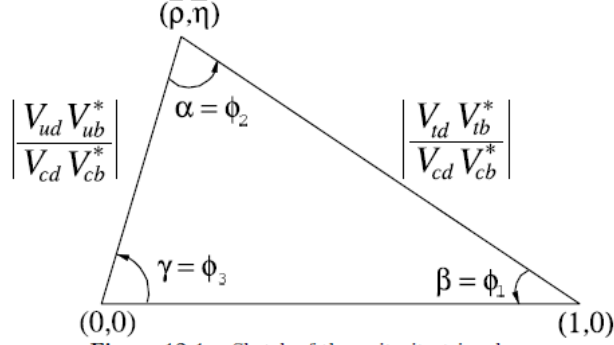


Figure 12.1: Sketch of the unitarity triangle.

Figure 1.1: Rescaled unitarity triangle corresponding to 1.28

These "unitarity triangles" have the same areas which have value $|J_{CP}|/2$. The relation between Jarlskog's measure of CP -violation J_{CP} and the Wolfenstein parameters is given by $J_{CP} \simeq \lambda^6 A^2 \eta$. Among all the unitarity triangles, one of the most interesting from an experimental point of view is the one related to Eq. 1.28 and is referred as the Unitarity Triangle (UT).

The UT has two vertices of this rescaled unitarity triangle are thus fixed at $(0, 0)$ and $(0, 1)$. The last vertex coordinates are in the (ρ, η) plane, such as shown in Fig 1.1 and the area is $|\eta|/2$. The two complex sides are:

$$R_u \equiv \sqrt{\rho^2 + \eta^2} = \frac{1}{\lambda} \left| \frac{V_{ub}}{V_{cb}} \right|, \quad R_t \equiv \sqrt{(1 - \rho)^2 + \eta^2} = \frac{1}{\lambda} \left| \frac{V_{td}}{V_{cb}} \right|. \quad (1.30)$$

The tree angles are denoted as α , β and γ and are related to the CKM matrix elements:

$$\alpha \equiv \arg \left[-\frac{V_{td}V_{tb}^*}{V_{ud}V_{ub}^*} \right], \quad \beta \equiv \arg \left[-\frac{V_{cd}V_{cb}^*}{V_{td}V_{tb}^*} \right], \quad \gamma \equiv \arg \left[-\frac{V_{ud}V_{ub}^*}{V_{cd}V_{cb}^*} \right]. \quad (1.31)$$

The current experimental knowledge is:

$$V_{CKM} = \begin{pmatrix} 0.97434_{-0.00012}^{+0.00011} & 0.22506 \pm 0.00050 & 0.00357 \pm 0.00015 \\ 0.22492 \pm 0.00050 & 0.97351 \pm 0.00013 & 0.0411 \pm 0.0013 \\ 0.00875_{-0.00033}^{+0.00032} & 0.0403 \pm 0.0013 & 0.99915 \pm 0.00005 \end{pmatrix} \quad (1.32)$$

as reported by the Particle Data Group [16].

1.4 Phenomenology of CP violation in meson decays

In this section, the phenomenology of CP violation in meson decays is given.

We define the decay amplitudes of particle M and its conjugate neutral mesons to a multi-particle final state f and its CP conjugate \bar{f} as

$$\begin{aligned} A_f &= \langle f | \mathcal{H} | M \rangle, & \bar{A}_f &= \langle f | \mathcal{H} | \bar{M} \rangle, \\ A_{\bar{f}} &= \langle \bar{f} | \mathcal{H} | M \rangle, & \bar{A}_{\bar{f}} &= \langle \bar{f} | \mathcal{H} | \bar{M} \rangle, \end{aligned} \quad (1.33)$$

where \mathcal{H} is the Hamiltonian governing weak interactions. The action of CP on these states introduces phases ξ_M and ξ_f that depend on their flavour content, according to

$$CP|M\rangle = e^{+i\xi_M}|\bar{M}\rangle, \quad CP|f\rangle = e^{+i\xi_f}|\bar{f}\rangle, \quad (1.34)$$

with

$$CP|\bar{M}\rangle = e^{-i\xi_M}|M\rangle, \quad CP|\bar{f}\rangle = e^{-i\xi_f}|f\rangle, \quad (1.35)$$

so that $(CP)^2 = 1$. The phases ξ_M and ξ_f are arbitrary and unobservable because of the flavour symmetry of the strong interaction. If CP is conserved then A_f and $\bar{A}_{\bar{f}}$ have the same magnitude and the same unphysical relative phase [16]:

$$\bar{A}_{\bar{f}} = e^{i(\xi_f - \xi_M)} A_f. \quad (1.36)$$

CP asymmetry in the decay is defined as:

$$\mathcal{A}_{CP} = \frac{|A_f|^2 - |\bar{A}_{\bar{f}}|^2}{|A_f|^2 + |\bar{A}_{\bar{f}}|^2} \quad (1.37)$$

and appears as a result of interference among various terms in the decay amplitude. As

an example, let us consider a decay process with several amplitudes:

$$\begin{aligned} A_f &= \sum_j |A_j| e^{i(\xi_{fj} + \xi_{Mj})} = \sum_j |A_j| e^{i(\delta_j + \phi_j)} \\ \bar{A}_f &= \sum_j |A_j| e^{i(\xi_{fj} - \xi_{Mj})} = \sum_j |A_j| e^{i(\delta_j - \phi_j)} \end{aligned} \quad (1.38)$$

where ξ_f (δ) and ξ_M (ϕ) are respectively the strong (CP conserving) and weak (CP violating) phases. Then to observe CP -violation there must be a contribution from at least two processes with different weak and strong phases in order to have a non vanishing interference term:

$$|A_f|^2 - |\bar{A}_f|^2 = -2 \sum_{i,j} |A_i| |A_j| \sin(\delta_i - \delta_j) \sin(\phi_i - \phi_j) \quad (1.39)$$

1.4.1 Neutral D meson formalism

The phenomenology of CP violation in neutral D meson is enriched by the presence of flavour mixing or oscillation, *i.e.* the quantum mechanics $D^0 \leftrightarrow \bar{D}^0$ transition. In fact, due to the structure of the weak interaction, an initially pure flavour eigenstate. A superposition of $|D^0\rangle$ and $|\bar{D}^0\rangle$,

$$|\psi(t=0)\rangle = a(0)|M^0\rangle + b(0)|\bar{M}^0\rangle. \quad (1.40)$$

will evolve in time as

$$|\psi(t)\rangle = a(t)|D^0\rangle + b(t)|\bar{D}^0\rangle + \sum_i c_i(t)|f_i\rangle, \quad (1.41)$$

where f_i are all the possible decay final states. The mixing is described by Schrödinger equation

$$i \frac{\partial}{\partial t} \begin{pmatrix} a(t) \\ b(t) \end{pmatrix} = \left(\mathbf{M} - \frac{i}{2} \mathbf{\Gamma} \right) \begin{pmatrix} a(t) \\ b(t) \end{pmatrix}, \quad (1.42)$$

where the elements of the mass matrix \mathbf{M} and decay matrix $\mathbf{\Gamma}$ are related to the Hamiltonian of the weak interactions.

$$\begin{aligned} M_{ij} &= m_0 \delta_{i,j} + \langle M_i | \mathcal{H}_w | M_j \rangle + \sum_k \text{P} \left(\frac{\langle_i | \mathcal{H}_w | f_k \rangle \langle f_k | \mathcal{H}_w | M_j \rangle}{m_0 - E_{f_k}} \right) \\ \Gamma_{ij} &= 2\pi \sum_k \delta(m_0 - E_{f_k}) \langle M_i | \mathcal{H}_w | f_k \rangle \langle f_k | \mathcal{H}_w | M_j \rangle \end{aligned} \quad (1.43)$$

where $M_1 = M^0$, $M_2 = \overline{M}^0$, \mathcal{H}_w is the weak Hamiltonian and m_0 is the neutral meson mass. Both the matrices are Hermitian, while a combination of them, i.e. $\mathbf{H} = \mathbf{M} - \frac{i}{2}\mathbf{\Gamma}$ is not. Inspecting the combination matrix \mathbf{H} we found the diagonal elements associated with flavour conserving transition and the other ones not. The eigenvectors of $\mathbf{H} = \mathbf{M} - \frac{i}{2}\mathbf{\Gamma}$ matrix define the masses and decay widths of the mass eigenstates, and are equal to

$$|D_H\rangle = p|D^0\rangle - q|\overline{D}^0\rangle, \quad |D_L\rangle = p|D^0\rangle + q|\overline{D}^0\rangle, \quad (1.44)$$

where p and q are complex number with $|p|^2 + |q|^2 = 1$ and

$$\frac{q}{p} = \sqrt{\frac{M_{12}^* - \frac{i}{2}\Gamma_{12}^*}{M_{12} - \frac{i}{2}\Gamma_{12}}}. \quad (1.45)$$

The corresponding eigenvalues are

$$\lambda_{H,L} = M_{11} - \frac{i}{2}\Gamma_{11} \pm \frac{q}{p} \left(M_{12} - \frac{i}{2}\Gamma_{12} \right). \quad (1.46)$$

The masses of the eigenstates are the real part of the eigenvalues, while the decay widths are proportional to the imaginary part.

$$\begin{aligned} m_{H,L} &= \Re(\lambda_{H,L}) = M_{11} \pm \Re\left[\frac{q}{p} \left(M_{12} - \frac{i}{2}\Gamma_{12} \right)\right], \\ \Gamma_{H,L} &= -2\Im(\lambda_{H,L}) = \Gamma_{11} \mp 2\Im\left[\frac{q}{p} \left(M_{12} - \frac{i}{2}\Gamma_{12} \right)\right]. \end{aligned} \quad (1.47)$$

If a state is an initially pure $|D^0\rangle$ or $|\overline{D}^0\rangle$ at time t one has

$$\begin{aligned} |D^0(t)\rangle &= g_+(t)|D^0\rangle - \frac{q}{p}g_-(t)|\overline{D}^0\rangle, \\ |\overline{D}^0(t)\rangle &= g_-(t)|\overline{D}^0\rangle - \frac{p}{q}g_+(t)|D^0\rangle, \end{aligned} \quad (1.48)$$

where

$$g_{\pm} = \frac{1}{2} \left(e^{-im_H t - \frac{1}{2}\Gamma_H t} \pm e^{-im_L t - \frac{1}{2}\Gamma_L t} \right). \quad (1.49)$$

This means that the time-dependent decay rate of an initially pure $|D^0\rangle$ state is

$$\begin{aligned} \Gamma(D^0(t) \rightarrow f) = & \Gamma \left[\left(|A_f|^2 + \left| \frac{q}{p} \bar{A}_f \right|^2 \right) \cosh(y\Gamma t) \right. \\ & + \left. \left(|A_f|^2 - \left| \frac{q}{p} \bar{A}_f \right|^2 \right) \cos(x\Gamma t) \right. \\ & \left. + 2\Re \left(\frac{q}{p} A_f^* \bar{A}_f \right) \sinh(y\Gamma t) - 2\Im \left(\frac{q}{p} A_f^* \bar{A}_f \right) \sin(x\Gamma t) \right] \end{aligned} \quad (1.50)$$

where x , y and Γ are defined as

$$\Gamma = \frac{\Gamma_H + \Gamma_L}{2}, \quad x = \frac{\Delta m}{\Gamma} = \frac{m_H - m_L}{\Gamma}, \quad y = \frac{\Delta\Gamma}{2\Gamma} = \frac{\Gamma_H - \Gamma_L}{2\Gamma} \quad (1.51)$$

In the Eq. 1.51 the terms depend on the square of the amplitude A are associated to decays taking place without oscillations, while the other ones depending on $|(q/p)\bar{A}_f|^2$ and $|(p/q)A_f|^2$ involve an oscillation. Other terms are the interference terms between decay and non-decay. The decay rates for the \bar{f} final states can be obtained changing A_f with $\bar{A}_{\bar{f}}$.

It is possible to observe CP violation in different ways

1. CP violation in the decay, happening when $|A_f/\bar{A}_{\bar{f}}| \neq 1$. This is the only source present also in charged-meson decays. The CP asymmetry is defined as

$$A_{CP}(f) = \frac{\Gamma(D^0 \rightarrow f) - \Gamma(\bar{D}^0 \rightarrow \bar{f})}{\Gamma(D^0 \rightarrow f) + \Gamma(\bar{D}^0 \rightarrow \bar{f})} = \frac{1 - |\bar{A}_{\bar{f}}/A_f|^2}{1 + |\bar{A}_{\bar{f}}/A_f|^2}. \quad (1.52)$$

2. CP violation in mixing, which takes place when $|q/p| \neq 1$. In this case a useful observable is the time-dependent version of Eq 1.52

$$A_{CP}(f, t) = \frac{\Gamma(D^0(t) \rightarrow f) - \Gamma(\bar{D}^0(t) \rightarrow \bar{f})}{\Gamma(D^0(t) \rightarrow f) + \Gamma(\bar{D}^0(t) \rightarrow \bar{f})}. \quad (1.53)$$

3. CP violation in the interference between decay and oscillation, occurring when $\Im(\lambda_f) \neq 0$ with

$$\lambda_f = \frac{q}{p} \frac{\bar{A}_{\bar{f}}}{A_f}. \quad (1.54)$$

Due to the presence of the interference term, the CP violation can occur even when

$|A_f/\bar{A}_f| = 1$ and $q/p = 1$, i.e. when there is no CP violation in the decay or mixing.

1.4.2 Charm and CP violation

The existence of charm quark was predicted in the late 1960s to explain the GIM mechanism [18]. The first experimental evidence was the discovery of the J/Ψ particle, also called charmonium resonance, while the first open charm meson (D^0, D^+) was found by the Mark I experiment in the 1976 [19]. The lagrangian responsible of the Cabibbo favoured charm decays is

$$\mathcal{L} = 4G_F\sqrt{2}V_{cs}V_{ud}^*(\bar{s}_L\gamma_\mu c_L)(\bar{u}_L\gamma^\mu d_L) + h.c. \quad (1.55)$$

where the Dirac spinor fields for the *up*, *down*, *charm* and *strange* quarks are denoted by the appropriate letter and G_F is the Fermi constant. However, the mass of the charm quark m_c of about $\simeq 1 \text{ GeV}/c^2$ makes perturbative expansions difficult as neither m_c nor $1/m_c$ are small. In addition, the many final state interactions and rescattering possibilities make it challenging to match theoretical predictions to experimental data. In 2007, the first evidence for the mixing of neutral charm mesons was found at the B -factory experiments by the BaBar and Belle collaborations [1, 20, 21]. This is now well established, and the most recent study at LHCb [13, 22] measures $y' = (0.69_{-0.07}^{+0.06}) \times 10^{-2}$ and $x' = (0.32 \pm 0.14) \times 10^{-2}$ [13, 23–25] those numbers are the world average for HFLAV collaboration. This two parameters are significantly smaller for the charm with respect to the K or B systems, and their small size means that most of neutral D mesons will decay before appreciable mixing can take place.

1.4.3 Search for CP violation in the $D^+ \rightarrow \phi\pi^+$ and $D_s^+ \rightarrow K_s^0\pi^+$

As discussed previously direct CP violation in charm decays requires the interference of two amplitudes to the same final state with different strong and weak phases. Obviously the amplitudes must have about the same size to create an appreciable interference. Those requirements are found in the singly-Cabibbo suppressed decays, where tree and loop (penguin) diagrams with comparable matrix elements, can occur. This document reports the result of a preliminary analysis aiming to search for CP violation in the singly-Cabibbo-suppressed channels $D_s^\pm \rightarrow K_s^0\pi^\pm$ and $D^\pm \rightarrow \phi\pi^\pm$. CP violation can arise from the interference between the amplitudes which involves elements of the CKM matrix and $V_{cd}^*V_{ud}$ or $V_{cs}^*V_{us}$ penguin amplitudes induced by heavy virtual particle, such as the b quark. Examples of diagrams decays are given in Fig. 1.2. Other (not shown)

possible diagrams, *e.g.* with different levels of colour- and OZI-suppression¹, exist for the D_s^+ decays which contribute to the overall matrix element. Unlike in neutral D meson decays, there is no possibility for W exchange diagrams. However, as shown in the Feynman diagrams of Fig. 1.2, the contribution to CP asymmetry of these amplitudes is strongly suppressed by the small value of $V_{cb}^*V_{ub}$. CP asymmetry is expected to be $\sim \mathcal{O}(0.1\%)$ or below [19] Fig. 1.3 reports also diagrams for control channels. Hence, for decays which contain a K^0 , at first order one would expect to observe an asymmetry consistent only with the CP violation in the neutral kaon system.

The current knowledge on CP violation in $D_{(s)}^\pm \rightarrow K_S^0 h^\pm$ and $D^\pm \rightarrow \phi \pi^\pm$ decays is given by the most important experiments CLEO [26], BaBar [27, 28], Belle [24, 29, 30] and LHCb experiments data [31–33]. The results indicate no evidence for CP violation so far and are reported in Tab. 1.2.

	$\mathcal{A}_{CP}[\%]$	Experiment (dataset)
$D_s^\pm \rightarrow K_S^0 \pi^\pm$	$0.60 \pm 2.00 \pm 0.30$	BaBar [27]
	$+5.45 \pm 2.50 \pm 0.33$	Belle [29]
	$+0.61 \pm 0.83 \pm 0.14$	LHCb (2011) [31]
	$+0.38 \pm 0.46 \pm 0.17$	LHCb (2011-2012) [32]
	$(1.3 \pm 1.9 \pm 0.5) \times 10^{-3}$	LHCb(2019) [33]
$D^\pm \rightarrow \phi \pi^\pm$	$0.35 \pm 0.30 \pm 0.15$	BaBar [28]
	$+0.51 \pm 0.28 \pm 0.05$	Belle [24]
	$-0.04 \pm 0.14 \pm 0.14$	LHCb (2011) [31]
	$(0.05 \pm 0.42 \pm 0.29) \times 10^{-3}$	LHCb(2019) [33]

Table 1.2: Summary of previous measurements of CP -violating asymmetries in $D_{(s)}^\pm \rightarrow K_S^0 h^\pm$ and $D^\pm \rightarrow \phi \pi^\pm$ decays. The errors correspond to statistical and systematic uncertainties

The latest LHCb results are the most precise, but they do not contain 2012 and 2018 data samples, and lots of improvements can be done to suppress the systematic uncertainties. After the first observation of CP violation in charm sector the work which starts with this thesis has the final goal to obtain a result comparable with ΔA_{CP} in precision after a full RUN 1 - RUN 2 analysis.

¹The OZI rule states that any strongly occurring process with a Feynman diagram that can be split in two by cutting only internal gluon lines will be suppressed.

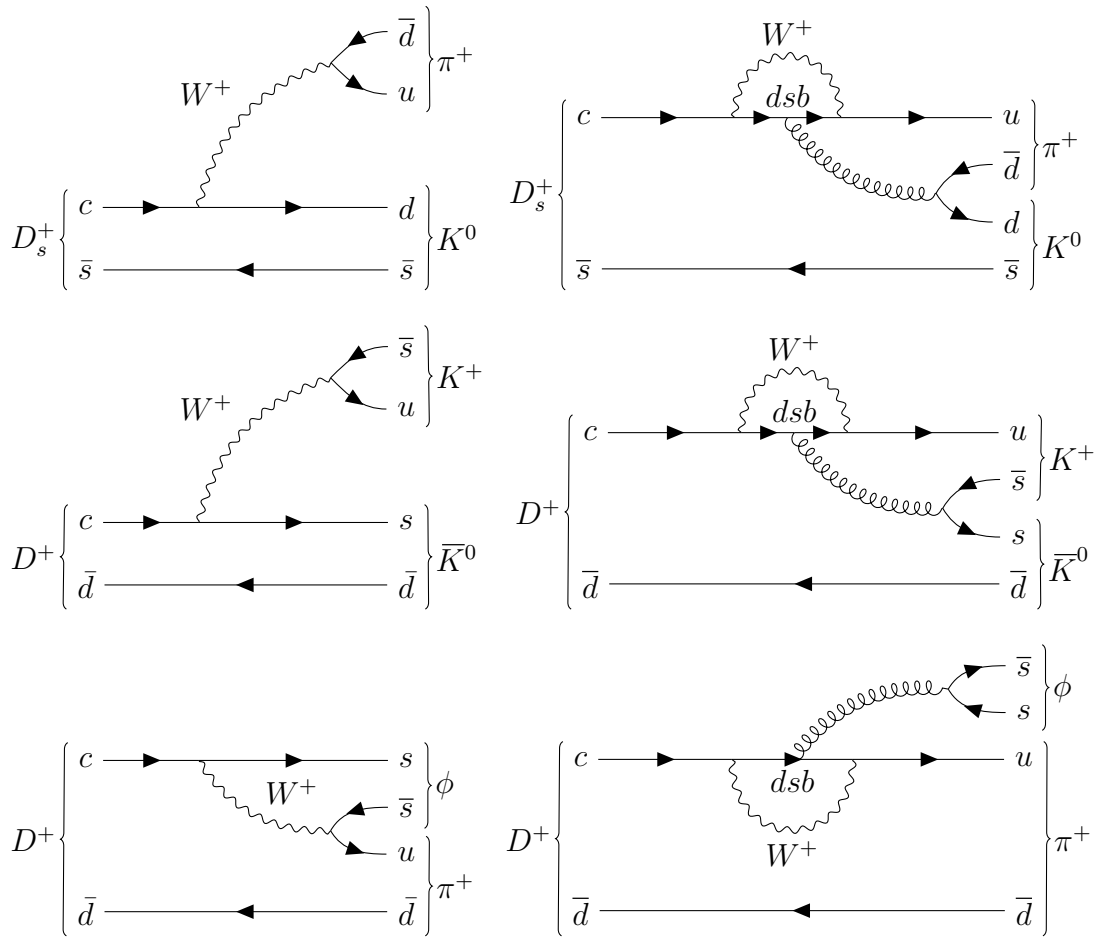


Figure 1.2: Feynman diagrams of the possible CS decays for the D -meson, respectively from above $D_s^+ \rightarrow K_S^0 \pi^+$, and $D^+ \rightarrow \phi \pi^+$. The diagrams on left side are so called tree diagrams and on the right side the so called penguin diagrams.

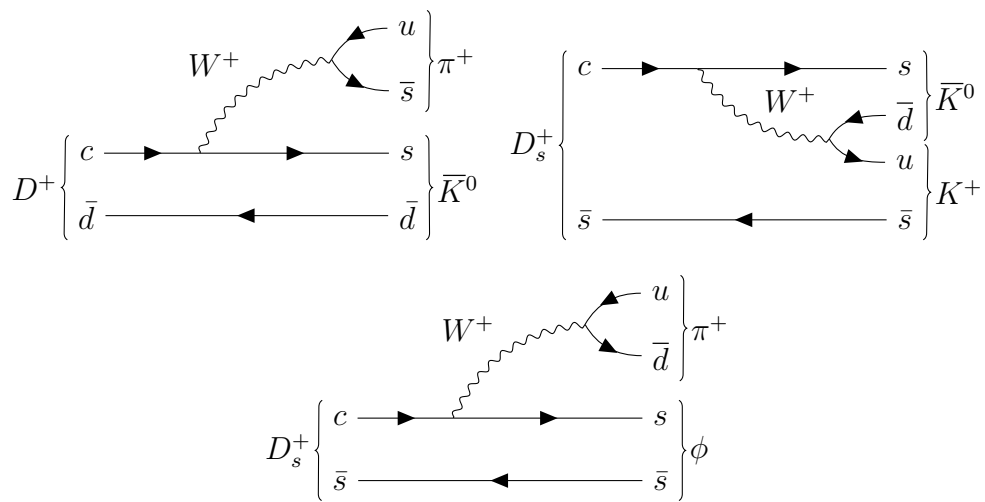


Figure 1.3: Feynman diagrams of Cabibbo-favored decays of D -mesons respectively, from the left-top side, $D^\pm \rightarrow K_S^0 \pi^\pm$, $D_s^\pm \rightarrow K_S^0 K^\pm$ and $D_s^\pm \rightarrow \phi \pi^\pm$.

Chapter 2

LHCb Experiment

The Large Hadron Collider beauty (LHCb) experiment [34] is dedicated to the study of heavy flavour physics at the Large Hadron Collider (LHC) [35] at CERN in Geneva. The main goal of this experiment is to study the CP violation, *i.e.* the CP -violating processes that involve the decays of charm mesons and the rare beauty ones. This research is to look forward, considering New Physics (NP) theories on CP -violation systems, in order to explain the baryogenesis of the universe.

Many models of new physics indeed produce contributions that change the expectations of the CP violating phases, rare decay branching fractions, and may generate decay modes which are forbidden in the Standard Model. To examine such possibilities, CP violation and rare decays of B_d , B_s and D mesons must be studied with much higher statistics and using many different decay modes [34]. The design of this experiment is made up of several detector in order to exploit the great production cross-section of $b\bar{b}$ pairs in pp collisions at the LHC energies, measured to be $\sigma(pp \rightarrow b\bar{b}X) = (154.3 \pm 1.5 \pm 14.3)\mu\text{b}$ at the energy of center of mass $\sqrt{s} = 13\text{TeV}$ and within the LHCb acceptance [36].



Figure 2.1: Logo for LHCb experiment, looking at the style, is clearly visible the principal aim of the experiment, the study of CP violating systems.

Instead to search the high p_T decay products that could indicate new particles, such as ATLAS and CMS experiment, LHCb approach to search New Physics with an aim

totally different. In fact, this experiment wants to measure the existence of new particle indirectly, by their virtual quantum effects. Moreover, in this Collaboration, are studied the heavy-flavour spectroscopy and production of gauge bosons, and searching for new exotic particles. In this chapter is described how the experiment works, *i.e.* the instruments and detectors utilized for this analysis of CP violation.

2.1 Large Hadron Collider (LHC)

The Large Hadron Collider is the world's largest and most powerful particle accelerator. It first started up on 10 September 2008, and remains the latest addition to CERN's acceleration complex. The LHC is a two-ring-superconducting-hadron accelerator and collider installed in the existing 26.7 km tunnel that was constructed between the 1984 and 1989 for the CERN LEP machine. The tunnel has eight straight sections and eight arcs and lies between 45 m and 170 m below the surface on a plane inclined as 1.4% sloping towards the Léman Lake. There are two transfer tunnels that linking the LHC to the CERN accelerator complex that acts as injector. The LHC design depends on some basic principles linked with the latest technology. Being a particle-particle collider, there are two rings with counter-rotating beams, unlike particle-antiparticle colliders that can have both beams sharing the same phase space in a single ring. The tunnel geometry was originally designed for the electron-positron machine LEP, and there were eight crossing points flanked by long straight sections for RF cavities that compensated the high synchrotron radiation losses. This collider is equipped only with four of the possible eight interaction regions, as shown in Fig.2.2, and to suppress beam crossing in order to prevent unnecessary disruptions of the beams. The aim of the LHC is to reveal the physics beyond the Standard Model with center of mass collision energies of up to 14 TeV with an instantaneous luminosity of $10^{34} \text{ cm}^{-2}\text{s}^{-1}$. The LHC is therefore designed as a proton-proton collider with separate magnet fields (of about 8 T) and vacuum chambers in the main arcs and with common sections only at the insertion regions where the experimental detectors are located. The magnets are made up by superconducting materials (Nb-Ti) cooled by super-fluid helium (1.9 K or -271.3° C). The accelerator complex at CERN is a succession of machines that accelerate particles to increasingly higher energies. Each machine boosts the energy of a beam of particles, before injecting the beam into the next machine in the sequence. Most of the other accelerators in the chain have their own experimental halls where beams are used for experiments at lower energies [37] The proton source is a simple bottle of hydrogen gas. An electric field is utilized to strip gas atoms from their electrons to yield proton. It is impossible to accelerate directly protons from their quasi-rest condition up to 6.5 TeV, for this reason

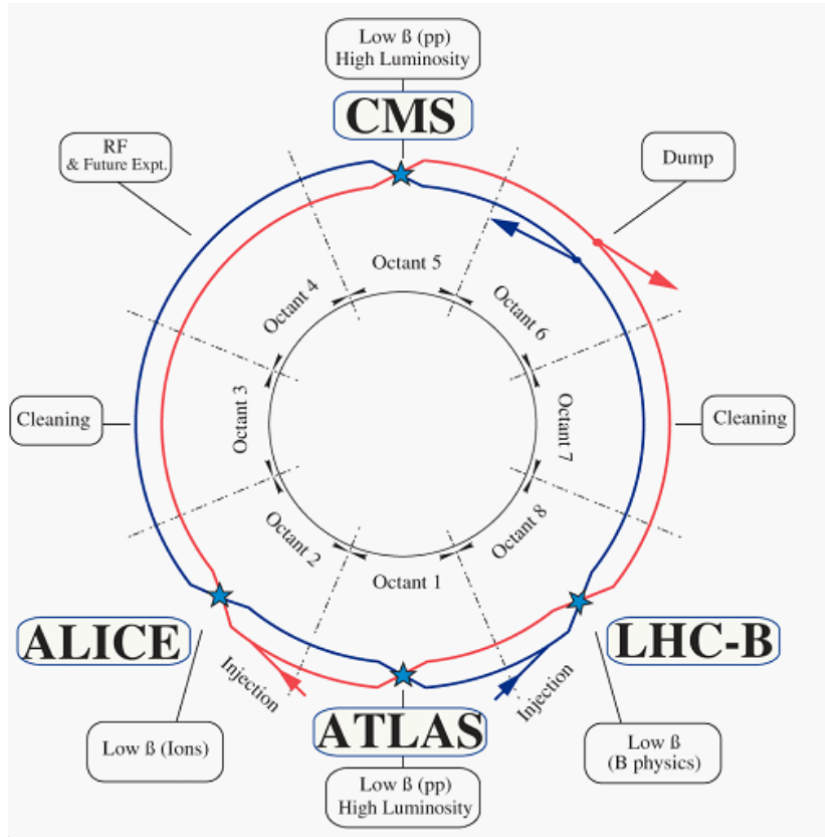


Figure 2.2: Experiments along the LHC ring

is necessary to make a preacceleration through complex systems. First of all, protons are injected in LINAC2, a linear accelerator that provides the Proton Synchrotron Booster (PSB) with proton bunches up to 50 MeV energy. Successively protons are injected in the PSB mechanism to reach 1 GeV of energy, after that, they are moved to the Proton Synchrotron, in order to accelerate the particle at 26 GeV. Then, the PS passes them to the Super Proton Synchrotron (SPS), where they are accelerated for the last time up to an energy of 450 GeV, before being injected in the LHC via two tunnels, called T12 and T18. After the two rings are filled, the machine is ramped to its nominal energy over about 28 minutes. The two beams are brought into collision inside four detectors (ALICE, ATLAS, CMS and LHCb) where the total energy at the collision point is equal to 13 TeV. The complex system could accelerate also ions utilized for ALICE experiment. Lead ions are generated by the vaporization of a highly pure lead sample at 800° C and successively ionized by an electron current. There are different charged ions produced, the selected

ones are accelerated to 4.2 MeV/u before passing through another mechanism to increase the number of nucleons in this ions (from ^{29}Pb to ^{54}Pb). The beam is accumulated then accelerated to 72 MeV/u in the Low Energy Ion Ring (LEIR), which carry them to the PS. At this point another boost occurs leading ions to 5.9 GeV/u sending them to SPS with another increasing mechanism (^{82}Pb). The procedure utilized to increase nucleus into ions is a stripping. The final step is marked by the LHC acceleration up to 2.56 TeV/u. The collisions Pb-Pb happen with a peak luminosity of about $10^{27}\text{cm}^{-2}\text{s}^{-1}$. Returning on the $p - p$ collision the LHC ring store 2808 proton bunch per ring, each containing 1.1^{11} protons colliding with a frequency of about 40 MHz. In this years LHC has performed very well in data taking and allowed the LHCb experiment to cross the threshold fo 6fb^{-1} of integrated luminosity over LHC Run-1 and Run-2, collecting data with an efficiency of over 90%. This implies that an unprecedented sample of D and B hadron has been collected, allowing the LHCb collaboration to perform high precision measurements, improving previous results coming form other phenomenal experiments such as BaBar, Belle ad CDF collaborations, showing the CP violation effects of charmed and beauty hadrons.

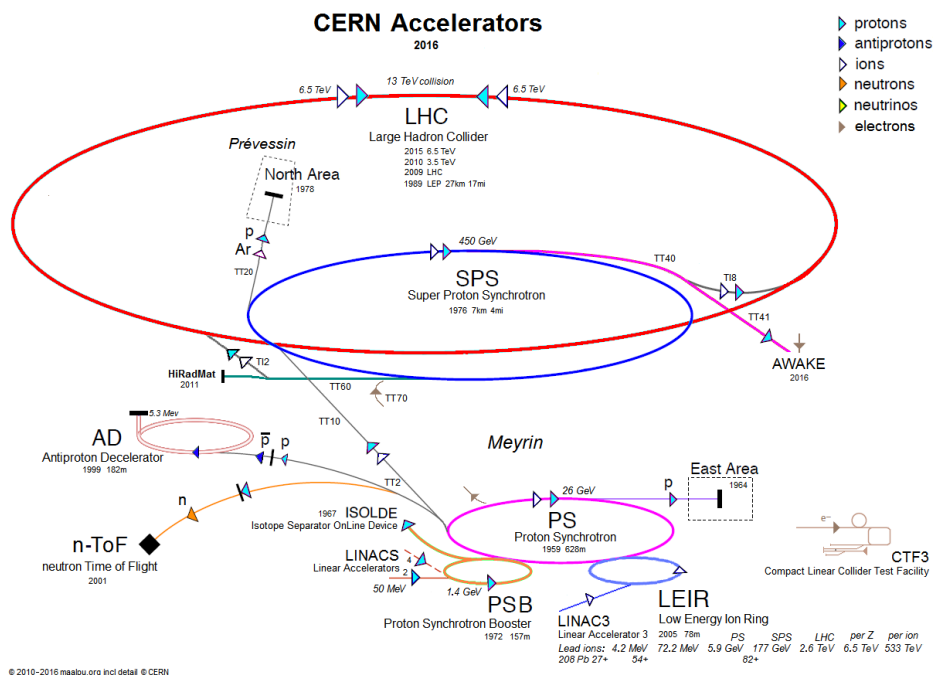


Figure 2.3: Scheme representing the CERN injection complex, with all the accelerator mechanism such as the LINACS, PBS, PS, SPS.

2.2 The LHCb Detector

LHCb detector is a single-arm spectrometer with a forward angular coverage ranging from approximately 10 mrad to 300 (200) mrad in the bending (non-bending) plane. The choice of the detector geometry is justified by the fact that at the high energies the B hadrons are predominately produced at the same forward or backward cone. Indeed, the average imbalance in momentum of two partons that collide during a pp interaction means that the b quarks are produced with a strong boost along the beam line. This spectrometer is completely viewed by the sketch in Fig.2.4. The principal features that compound this detector are:

- an efficient, robust and flexible trigger in order to cope with the harsh hadronic environment. The trigger must be sensitive to many different final states;
- a high precision VELO detector able to reconstruct all the interaction and decay vertexes from B and D hadron. Thanks to this feature is possible to study the neutral mesons oscillation and CP violation, with proper-times.
- a good PID (particle identification) made up the several detector located in this experiment.
- a data acquisition system with high bandwidth and powerful online data processing capability, required to optimize the data taking.

2.2.1 Vertex Locator (VELO)

The VERtEX LOcator provides precise measurements of track coordinates close to the interaction region, which are used to identify the displaced secondary vertices which are a distinctive feature of b and c -hadron decays [38]. The VELO consist in a series of silicon modules, each providing a measure of the r and ϕ coordinates, arranged along beam direction as is possible visualize in the Fig.2.5. Two planes perpendicular to the beam line and located upstream of the VELO sensors are called the pile-up veto system. The VELO sensors are placed at a radial distance from the beam which is smaller than the aperture required by the LHC during injection and must therefore be retractable. The detectors are mounted in a vessel that maintains vacuum around the sensors and is separated from the machine vacuum by a thin walled corrugated aluminum sheet. Fig.2.5 shows an expanded view from inside one of the boxes, with the sides cut away to show the staggered and overlapping modules of the apposite detector half. The corrugated foils,

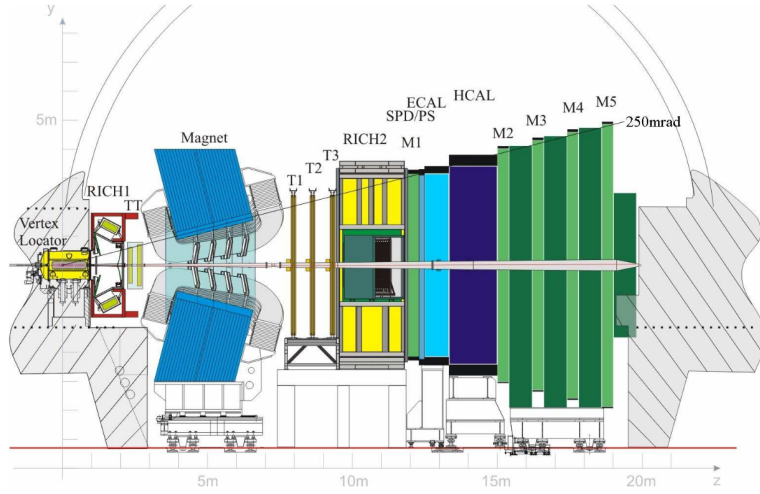


Figure 2.4: Design of LHCb detector. The right-handed coordinate system adopted has the z -axis along the beam, and the y one along the vertical. From the left side are visible all the sub-detectors that made the detector: VELO, RICH1, TT, Magnet, Trackers, RICH2, ECAL, HCAL, Muon detectors (composed by MWPC).

hereafter referred to as RF-foils, form the inner faces of the boxes (RF-boxes) within which the modules are housed.

Each silicon modules is divided in two halves to allow the positioning of the VELO during the data taking phase (closed) or during the beam stabilization phase (open), as can be seen in the bottom of Fig.2.5. For this reason, the modules are installed on a movable device placed inside a vacuum vessel; it is important to note that the two halves of a module partly overlap in the closed VELO configuration, in order to achieve a better geometrical coverage. The modules are composed of two planes of $220\mu\text{m}$ thick silicon micro-strip sensors able to measure the distance from the beam (radial distance, R) and the polar angle ϕ of hits generated by the ionizing particles that cross the VELO. The structure of such R and ϕ sensors is reported in Fig.2.6. The third coordinate z is simply given by the module position. The R sensors are divided into four parts per halve, each one covering an angle of about 45° ; the micro-strips composing these parts are modelled in a semi-circular shape and their width increases as the distance from the center becomes grater, because the majority of the particles is expected to be near the beam axis (*i.e.* in the high η^1 regions). The micro-strips width ranges from $40\mu\text{m}$

¹The pseudo-rapidity η is defined as a approximate for the Lorentz-invariant rapidity y

$$\eta = -\ln(\tan(\theta/2)) \sim \frac{1}{2} \ln \left(\frac{\vec{p} + p_z}{\vec{p} - p_z} \right) = y$$

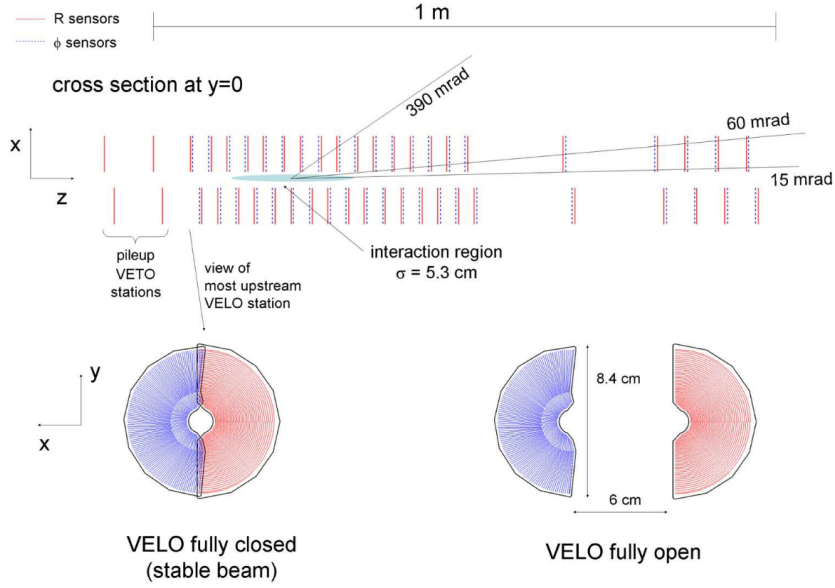


Figure 2.5: Cross section in the (x, z) plane of the VELO silicon sensors. On the top the fully-close mode. Below the frontal view in two configurational mode fully-closed and open.

near the centre to $92\mu\text{m}$ far from the beam. The ϕ sensors are divided in a inner and outer region. Those ones have different skew to the radial direction to improve patter recognition: they are tilted by 20° and 10° respectively. Moreover, to improve the track reconstruction the longitudinally adjacent ϕ sensors have apposite skew to each other.

Another thing to take into account is the resolution on those two coordinates (x, y) ranging form $40\mu\text{m}$ to $10\mu\text{m}$ depending on the number of track fitted. Regarding, instead, the coordinate z along the beam pipe has a range resolution of 250 to $50\mu\text{m}$.

2.2.2 The Silicon Tracker (ST)

The Silicon Tracker (ST) comprises two detectors: the Trigger Tracker(TT) and the Inner Tracker (IT) [38]. Both of those detectors use silicon microstrip sensor with a strip pitch of about $200\mu\text{m}$. The TT is a 150cm wide and 130cm high planar tracking station that is located up-stream of the LHCb dipole magnet and covers the full acceptance of the experiment. The IT, instead, covers a 120 cm wide and 40 cm high cross shaped region in the centre of the three tracking stations downstream of the magnet. The

where θ is the angle between the particle and the beam line p_z is the longitudinal momentum

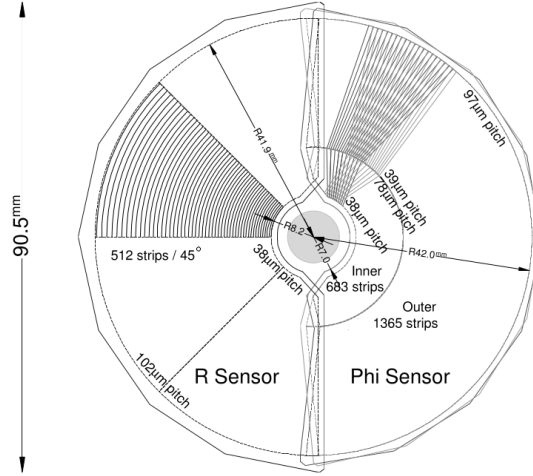


Figure 2.6: Sketch illustrating the $r\phi$ geometry of the VELO sensors. The different arrangement of the bonding pads leads to the slightly larger radius of the R -sensor; the sensitive area is identical.

main design choices for the Silicon Tracker detectors were largely driven by the following considerations:

Spatial resolution: simulation studies have demonstrated that a single-hit resolution of about $50\mu\text{m}$ is adequate for both the TT and IT. The momentum resolution of the spectrometer is then dominated by multiple scattering over almost the full range of particle momenta. Readout strip pitches of about μm meet this requirement and were therefore chosen for both detectors.

Hit occupancy: Charged particle densities of about 5×10^2 per cm^2 for minimum bias events are expected in the innermost regions of the TT and about two order of magnitudes lower on the outermost regions. For this reasons different readout strip lengths were chosen for different regions of the detector to keep maximum strip occupancies at the level of a few percent while minimizing the number of readout channels.

Signal shaping time: In order to avoid pile-up of events from consecutive LHC bunch crossings, fast front-end amplifiers with a shaping time of the order of the bunch crossing interval of 25ns have to be used.

Single-hit efficiency: Each detection layer should provide full single-hit efficiency for

minimum ionising particles while maintaining an acceptably low noise hit rate. The critical parameter is the signal-to-noise ratio, defined as the most probable signal amplitude for a minimum ionising particle divided by the RMS of the single strip noise distribution. Deterioration from radiation damage is expected after ten years at nominal luminosity.

Trigger Tracker

All four detection layers of the TT are housed in one large light tight and thermally and electrically insulated detector volume, in which a temperature below 5°C is maintained [39]. The detector volume is continuously flushed with nitrogen to avoid condensation on the cold surfaces. To aid track reconstruction algorithms, the four detection layers are arranged in two pairs, (x, u) and (v, x) , that are separated by approximately 27 cm along the LHC beam axis. The layout consists of a row of seven silicon sensors organized into either two or three readout sectors. The readout hybrids for all readout sectors are mounted at one end of the module. The regions above and below the LHC beam-pipe are covered by one such half module each. A main advantage of this detector design is that all front-end hybrids and the infrastructure for cooling and module supports are located above and below the active area of the detector, outside of the acceptance of the experiment. The TT task is to provide reference segments used to combine the track reconstructed in the tracking stations, with those ones in the VELO, in order to improve the momentum and coordinate resolution. Since in the space between the VELO and the TT stations an integrated magnetic field of 0.15Tm is present, the track transverse momentum can be estimated with a resolution of $\delta p_T/p_T = 25\%$ at $p_T = 1 \text{ GeV}/c$.

Inner Tracker

Each of the three IT stations consists of four individual detector boxes that are arranged around the beam pipe as shown in Fig. 2.8. The detector boxes are light tight and electrically and thermally insulated, and a temperature below 5°C is maintained inside them. They are continuously flushed with nitrogen to avoid condensation on the cold surfaces. Each detector box contains four detection layers and each detection layer consists of seven detector modules. This is done to improve the precision of the track reconstruction.

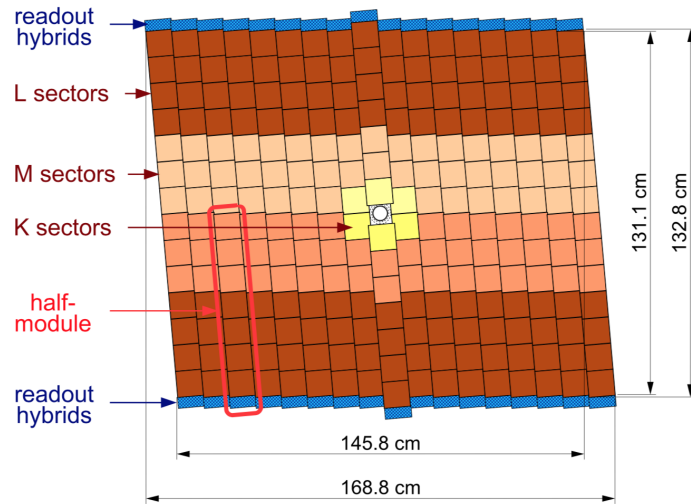


Figure 2.7: Layout of the third TT detection layer. Different readout sectors are indicated by different shadings

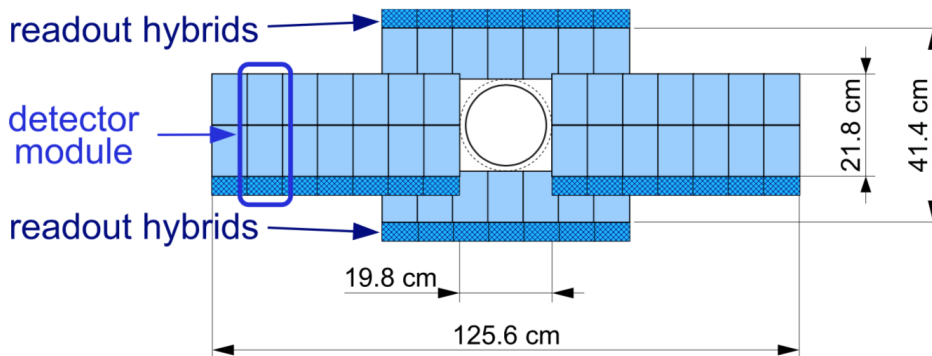


Figure 2.8: The inner Tracker layout

2.2.3 Tracker Station

The three Tracking Stations T1, T2 and T3 are placed behind the magnet. They are divided in two main parts, depending on the distance from the beam pipe. The inner part of the Tracking Stations, is called Inner Tracker (IT), while the outer part is called Outer Tracker (OT). They adopt different technologies to detect particles: the former is composed of silicon micro-strips sensors, while the latter consists of drift straw tubes. The Inner Tracker [39] covers around the beam-pipe region and it is arranged in a cross-

shaped geometry, that grants optimal coverage while conserving surface; each station consists of four independent boxes arranged as shown in Fig. 2.8. As for the TT, the first and fourth planes of the IT have the sensors parallel to the vertical plane, while the second and the third have the sensors tilted by $+5^\circ$ and -5° . The side boxes have two ladders of micro-strips, where the lower sensors are connected in series with the upper ones to a single readout channel, while the top and the bottom boxes have only one micro-strip ladder. The total IT size is about 1.2 m in the bending plane and about 40 cm in the vertical plane. Instead, the OT is a gas filled straw tubes detector it covers about 99% of the T1-T3 tracker stations. Every tracker station is covered by four planes of straw tubes. Each plane has got two rows of tubes, arranged as a honeycomb structure as in Fig. 2.9. Straw tubes are cylinders with a 5cm of radius filled by a mixture of Ar-CF₄-CO₂. At the ends are displaced locator pieces, those support and centre the anode wire with a precision up to $100\mu\text{m}$. Moreover, the OT measures drift times rather than pulse heights. Concerning the readout times is taken into account that the time window exceeds a single LHC bunch crossing interval, this effect is given by the limited drift speed of the gas mixture, but the OT resolution obtained is better than $200\mu\text{m}$.

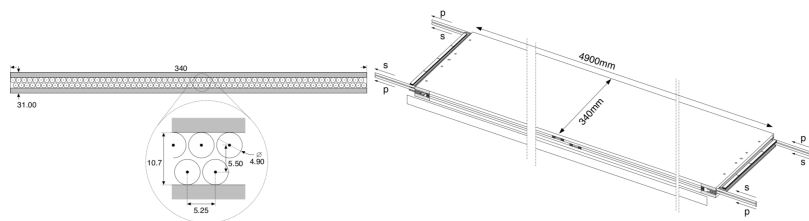


Figure 2.9: Cross section of a straw-tubes module (left) and its design (right).

2.2.4 Magnet

A dipole magnet is used in the LHCb experiment to measure the momentum of the charged particles. The measurement covers the forward acceptance of ± 250 mrad vertically and of ± 300 mrad horizontally. The super-conducting magnet proposed initially [40], would have required unacceptably high investment, costs and a lot of construction time. This magnet is replaced by another worm one, but constructed properly in order to have the required acceptance.

LHCb dipole magnets

The magnet is formed by two coils placed with a small angle with respect to the beam axis, to increase the opening window with z in order to *follow the acceptance* of LHCb detector. The main component of the magnetic field is along the y -axis, this feature permits to take the xz -plane as the bending plane. The maximum strength attainable from this dipole is of 1T, while its integral along the length of the detector is about $\int \vec{B} \cdot d\vec{l} = 4\text{Tm}$. As we will see in Fig. 2.10, all the tracker detectors are placed outside the magnetic dipole. Before the data-taking period whit Hall probes to obtain a precise map, is usually measured the strength of this field, because is crucial to have a good resolution in momenta and consequently a good mass resolution. Another unique feature of this detector is the possibility of reversing the magnet polarity, in fact those two configuration are called *MagDown* or *MagUp*. The main reason of this feature is to allow precise control of the left-right asymmetries introduced by the detector. Indeed, particles hit preferentially one side of the detector, depending on their charge, generating asymmetries if the detector is not properly symmetric. This polar switching (once every two weeks approximatively), then, allows the cancellation of this systematic asymmetries. As we will see later in the next chapters, there will be the measure of two samples taken with different polarity.

2.2.5 Tracking algorithm and performances

The tracks generated by the particles going through the LHCb detector could be categorized into five labels.

Long tracks: particles that hit all the sub-detectors.

VELO tracks: hits produced only inside the VELO detector. This is possible when the particles are produced with a wide angle respect the beam pipe and exiting the acceptance of the detector.

Upstream tracks: particles with low momenta hitting VELO and TT detectors then are kicked out from the acceptance by the magnetic field. Measure of their momenta is also possible with the residual magnetic field into the VELO detector, but with the 20% of uncertainty.

Downstream tracks: long lived neutral particles can decay between VELO and the TT detectors, producing charged particles that generate hits only into TT and tracking stations.

T tracks: hits generated only in the tracking stations.

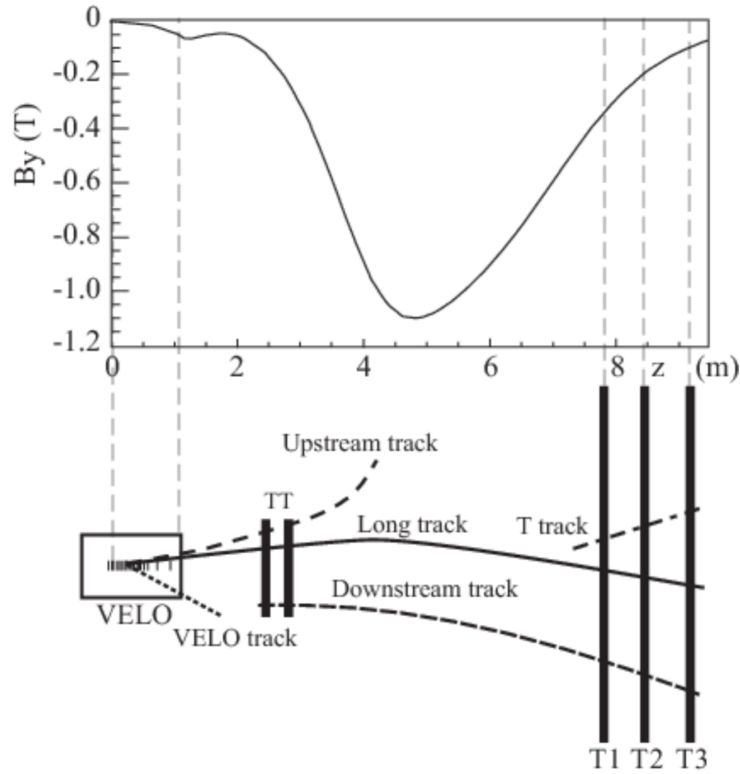


Figure 2.10: Sketch illustrating the various track types: long, VELO, upstream, downstream and T tracks. For reference the main B-field component (B_y) is plotted above as a function of the z coordinate [41].

The reconstruction of tracks is made in a hierarchical way in fact the first step is an algorithm based on tries to reconstruct long tracks and after that picks up unused segment to reconstruct up and downstream tracks. The track reconstruction process is organized in a hierarchical way: the algorithm tries firstly to reconstruct long tracks and then it picks up unused segment to reconstruct downstream and upstream tracks. Long tracks are reconstructed with two algorithms: the first extrapolates VELO segment to the tracking stations, adding to the track the compatible hits in the TT. The second matches VELO and tracking station segments one to each other, extrapolating VELO segments in the forward direction and tracking station segments in the backward direction. Downstream tracks are reconstructed starting from tracking station segments and then adding the compatible hits in the TT to those segments. Upstream tracks are

obtained extrapolating VELO segments to the TT, adding compatible hits and requiring a non-compatibility with any of the tracking station segments.

The reconstruction of tracks is divided in two steps: track finding and track fitting. The first starts with the definition of segments in the various sub-detectors: inside the VELO, segments are created matching all hits that lie on a straight line. In the tracking stations, a segment is created matching the hits contained in a region of the first and third station, using the information given only by one plane of vertically oriented micro-strips sensors. Then, under the hypothesis of a parabolic trajectory, the algorithm calculates the position of the hit in the middle stations and searches for compatible hits. If a signal is found, it is added to the segment and it is used to better determine parameters of the trajectory. Finally, the compatible hits coming from the other planes of sensors are also added, in order to have a 3-dimensional segment. Afterwards, a bi-directional Kalman filter [42] is applied to better determine the track parameters and then a clone-killer algorithm compares the reconstructed tracks, two by two: if a pair of tracks shares more than a fixed percentage of hits they are considered clones and only that with more hits (or the best χ^2 from the track fitting) is stored.

2.2.6 The LHCb particle identification system

In this section all the LHCb sub-detectors used for the particles identification (PID) are described. They consists in two Ring Imaging Cherenkov (RICH1 and RICH2) detectors, the electromagnetic calorimeter (ECAL), the hadronic calorimeter (HCAL) and finally the muon stations.

The RICH detectors

Particle identification is of fundamental importance in CP violation measurements. The LHCb experiment exploits two RICH detectors, the first one installed immediately after the VELO and the second one positioned after the tracking stations, to discriminate between charged pions, kaons and protons in a momentum range from few GeV/c up to about 150 GeV/c. Cherenkov light detectors exploit the light emitted by particles that travel in a medium faster than light in the same medium. The relation between the Cherenkov photon emission angle θ_c and the refraction index n of the radiator is

$$\cos(\theta_c) = \frac{1}{\beta n}, \quad (2.1)$$

where $\beta = v/c$ is the particle velocity relative to the speed of light in the vacuum. The Cherenkov light emission only occurs when the particles exceeds the threshold value of

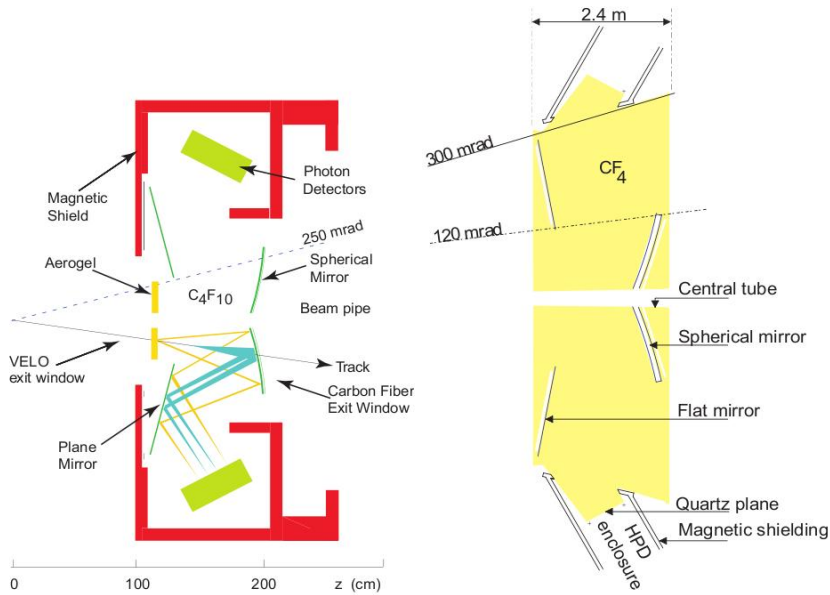


Figure 2.11: Left: schematic view of the RICH1 sub-detector [34]. The Cherenkov light is emitted with different angles from the Aerogel (yellow) and the C_4F_{10} (light blue) radiators. Right: schematic view of the RICH2 sub-detector, filled with CF_4 gas [34].

$\beta_{th} = 1/n$ (*i.e.* $\theta_c = 0$) while each radiator has a maximum emission angle $\theta_c^{max} = \arccos(1/n)$ which is obtained when $v = c$. It is evident that for particles approaching the speed of light the Cherenkov angle will saturate to θ_c^{max} and it is therefore necessary to have different radiators in order to discriminate particles in a wide range of momenta.

The RICH1 [34] is optimized to identify tracks with a relatively low momentum, between 1 GeV/c and about 50 GeV/c. The structure of the apparatus is reported in the left part of Fig. 2.11. The geometrical acceptance (from 25 mrad to 330 mrad) of the device is enough to cover the whole LHCb detector acceptance. During Run-1, there were two different types of radiators inside RICH1: the first was a 5 cm thick Aerogel layer with $n = 1.03$, suitable for low momentum particles, while the second was gaseous (C_4F_{10}) with $n = 1.0015$ filling the remaining part of the detector and was employed to detect particles with higher momenta. The Aerogel radiator was removed in the operational shut down before Run-2 as its ability to provide particle ID was compromised by the total number of photons in RICH1 in such a high track multiplicity environment [43].

The structure of the RICH2 [34] sub-detector is reported in the right part of Fig. 2.11. Its geometrical acceptance, ± 120 mrad (horizontal) and ± 100 mrad (vertical), covers the region of the detector where most of high momentum particles are found. The radiator chosen is CF_4 with a refraction index $n = 1.00046$, optimal for the higher momentum,

up to about 150 GeV/c.

In both the detectors, the Cherenkov light is focused, through a system of spherical and plane mirrors, onto a lattice of photo detectors, the Hybrid Photon Detector (HPD). The HPDs are placed in both the RICH sub-detectors, outside the experiment acceptance and they are shielded against the residual magnetic field. Indeed, the photo-electrons created in the photomultipliers would be bent by the residual magnetic field reducing the HPD's performances.

Particle identification method

RICH detectors are able to discriminate between the various mass hypothesis for a given particle. Indeed, as shown in Fig. 2.12, the photon emission angle is related to the particle mass and to its momentum. Since the Cherenkov light emission covers the full solid angle, rings with radius proportional to θ_c are expected on the HPD plane. Measuring the photons hit positions, it is then possible to discriminate the various mass hypotheses.

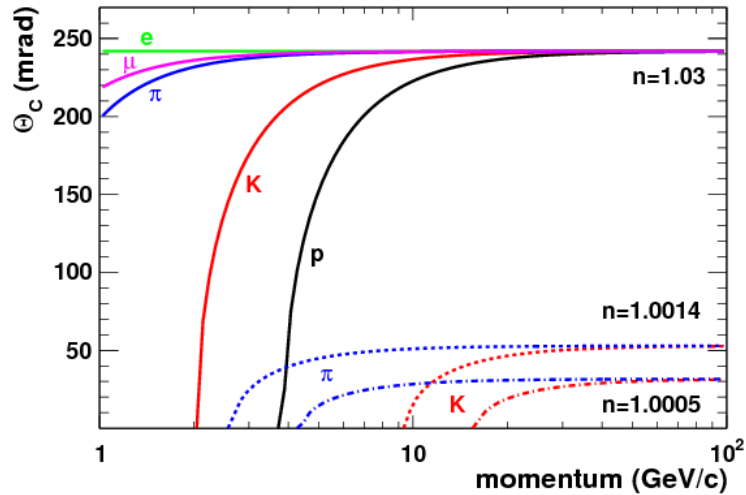


Figure 2.12: Cherenkov angles as a function of momentum for different particle species and for the three different values of the refractive index n corresponding to the three radiator materials used in the RICH setup [44].

Due to an irreducible background, given by photons coming from other particles, and due to the complexity of the problem, the following approach has been chosen to achieve the best particle discrimination. For a given set of mass hypotheses, the probability for a single photon to be detected on a single HPD pixel is computed; then, the expected

contribution from all sources is compared with the observed number of photons and a likelihood is calculated (the change in the likelihood value depends only on the mass hypothesis assigned to the tracks). Only five mass hypotheses are considered for the tracks detected: electron, muon, pion, kaon and proton. Since the computation of the likelihood for all tracks would be unfeasible, a different approach is adopted. In fact, the pion mass hypothesis is used for all the tracks detected and a first global likelihood is computed. Then the hypothesis is changed to e, μ, K and p for one particle at a time and the change in the global likelihood is computed. The chosen mass hypothesis is the one that returns the maximum improvement in the global likelihood. This process is repeated for all tracks, until no improvement is observed in the likelihood value.

The discriminating variable is the so-called $\Delta \log(\mathcal{L})_{X-\pi}$ which is the difference between the logarithm of the likelihood under the X (e, μ, K or p) and π hypothesis for the observed track:

$$\Delta \log(\mathcal{L})_{X-\pi} = \log(\mathcal{L}_X) - \log(\mathcal{L}_\pi). \quad (2.2)$$

For example, a large positive value of $\Delta \log(\mathcal{L})_{K-\pi}$ corresponds to a high probability that the particle is a kaon, while a large negative value corresponds to a high probability that the particle is a pion.

The efficiency of this discriminating method had been widely studied using real data sample with high purity final states selectable only using kinematical cuts, due to their particular kinematic characteristics (*e.g.* $K_S^0 \rightarrow \pi^+\pi^-$, $\Lambda^0 \rightarrow p\pi^-$, and $D^{*+} \rightarrow D^0(\rightarrow K^-\pi^+)\pi^+$).

2.2.7 The calorimeters system

The calorimeters system [45] is used to measure hadron, electron and photon energies, thus giving information for their identification. Moreover, it provides important information for the Level-0 trigger (L0), evaluating hadron, electron and photon transverse energy E_T . The calorimeters system is divided into four sub-detectors:

- Scintillator Pad Detector (SPD).
- Pre-Shower (PS).
- Electromagnetic Calorimeter (ECAL).
- Hadronic Calorimeter (HCAL).

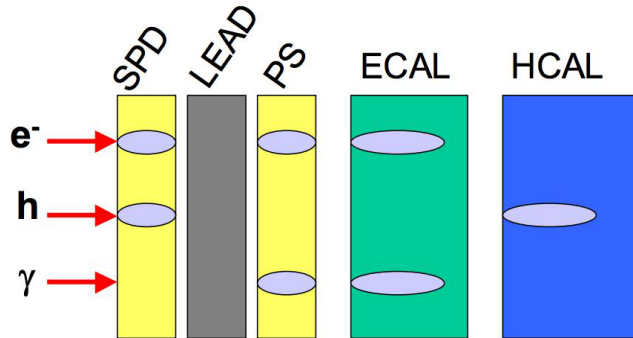


Figure 2.13: Signal deposited on the different parts of the calorimeter by an electron, a hadron and a photon [34].

A sketch of the calorimeters system and the response of each detector with the particle types is reported in Fig. 2.13. Each sub-detector is divided into regions where differently sized sensors are used. SPD, PS and ECAL are divided in three regions (inner, middle and outer), while HCAL is divided only in two regions (inner and outer). The sensor size increases as the distance from the beam pipe is greater to reach a compromise between occupancy and the number of readout channels.

The SPD and the PS are auxiliary sub-detectors of the Electromagnetic calorimeter and they are placed in front of it. The SPD is used to discriminate between charged and neutral particles, as the former emit light when crossing a scintillator material while the latter do not. The PS is instead used to obtain a better discrimination between electrons and pions. Both the sub-detectors consist of scintillating pads with a thickness of 15 mm, inter-spaced with a 2.5 radiation lengths² lead converter. The light produced by the scintillator material is collected using wavelength-shifting fibers (WLS). These fibers are used to transmit the light to multi-anode photomultipliers (MAPMTs) located outside the detector. The SPD and PS contain about 6000 pads each.

The ECAL is a sampling calorimeter separated in independent modules. In each module, the scintillation light is read out via WLS fibers running perpendicularly to the converter/absorber plates: this technique offer the combination of an easy assembly,

²The radiation length is defined as

$$X_0 = \frac{A \cdot 716.4 \text{g/cm}^3}{Z(Z+1) \ln(287\sqrt{Z})}$$

where A is the mass number and Z is the atomic number of the considered material. The radiation length corresponds to the distance over which the energy of an electron is reduces by a factor $1/e$ only due to radiation loss.

good hermicity and fast time response. A sketch of the ECAL is given in Fig. 2.14. Each ECAL module is composed of 66 lead converter layers (2 mm thick), each one installed between two plastic scintillator layers 4 mm thick. In total, all the layers installed in the ECAL correspond to about 25 radiation lengths and 1.1 nuclear interaction lengths³. The WLS fibers bring the light produced by the scintillator material to the readout photomultipliers in the back part of the module. The module size and the number of readout channels differ depending on the region where the module is installed. In the inner region each module has a section of $4 \times 4 \text{ cm}^2$ and 9 readout channels. Finally, the outer region is composed of $12 \times 12 \text{ cm}^2$ modules with one channel each.

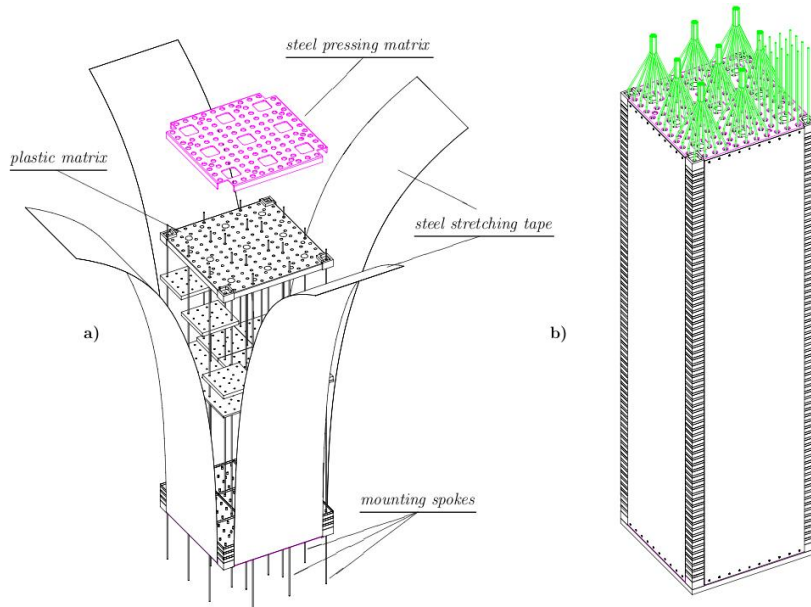


Figure 2.14: Left: representation of an ECAL module during the assembly phase. The lead/scintillator layers are clearly visible. Right: representation of an assembled ECAL module. The green lines connected to an end are the WLS fibers connecting the calorimeter to the photomultipliers [45].

The HCAL main task is to measure the energies of hadronic showers. This informa-

³The nuclear interaction length is defined as

$$\lambda = \frac{A}{N_A \rho \sigma_{inel}}$$

where N_A is the Avogadro constant, A is the mass number and ρ is the density of the considered material while $\sigma_{inel} \sim \sigma_{pp} A^{2/3}$ is the inelastic cross section between the particle and the nucleus. The nuclear interaction length is the mean path length required to reduce the numbers of relativistic charged particles by the factor $1/e$ as they pass through matter.

tion is fundamental for the Level-0 trigger. The HCAL structure is very similar to the ECAL structure, with the difference that each module is composed of scintillator layers 4 mm thick interleaved with steel layers 16 mm thick. This corresponds to roughly 5.6 nuclear interaction lengths in total. In the inner region modules have a section of 13×13 cm², while in the outer region their dimensions are 26×26 cm².

Calorimeters system resolution

The calorimeters system performances have been evaluated from many test beams made before the start of the data taking. Energy resolutions are given by $\sigma(E)/E = \frac{(8.5-9.5)\%}{\sqrt{E}} \oplus 0.8\%$ for ECAL and $\sigma(E)/E = \frac{(69 \pm 5)\%}{\sqrt{E}} \oplus (9 \pm 2)\%$ for HCAL. The ECAL calibration is achieved by reconstructing resonances decaying to two photons like $\pi^0 \rightarrow \gamma\gamma$ and $\eta \rightarrow \gamma\gamma$. Calibration of the HCAL can be realized by measuring the ratio E/p between the energy E measured in the calorimeter for a hadron with momentum p , measured by the tracking system.

2.2.8 The muon system

The final part of the LHCb detectors consists of five muon stations, that altogether form the muon sub-detector [46]. Muons with high p_T are very important particles since several final products of B-hadron decay chains contain muons. The five stations (M1-M5) cover an angular acceptance of ± 300 mrad in the horizontal plane and ± 200 mrad in the vertical plane. The geometrical efficiency for the detection of muons coming from B-hadrons is nearly 46%. The first muon station M1 is placed before the calorimeters, to avoid possible muon multiple scattering effects, that could modify the particle trajectory. The remaining stations (M2-M5) are placed after the calorimeter system, at the end of the LHCb detector. A schematic view of the muon sub-detector is reported in Fig. 2.15.

Each muon station is divided into four regions (R1-R4) around the beam pipe. The dimensions of the chambers increase as they are more and more distant from the beam pipe. Moreover, also the segmentation of each region increases as the distance from the beam pipe becomes greater in a ratio 1:2:4:8. In this way, the charged particle occupancy is expected to be about the same in each region. All the chambers are Multi-Wire Proportional Chambers (MWPCs), except for the inner region of the M1 station where Gas Electron Multipliers (GEMs) detectors are employed. The latter consist of three GEM foils sandwiched between anode and cathode planes. MWPCs have four overlapped gaps, each one 5 mm thick and with a distance between wires of about 2 mm. In total, the muon detector contains 1380 MWPCs.

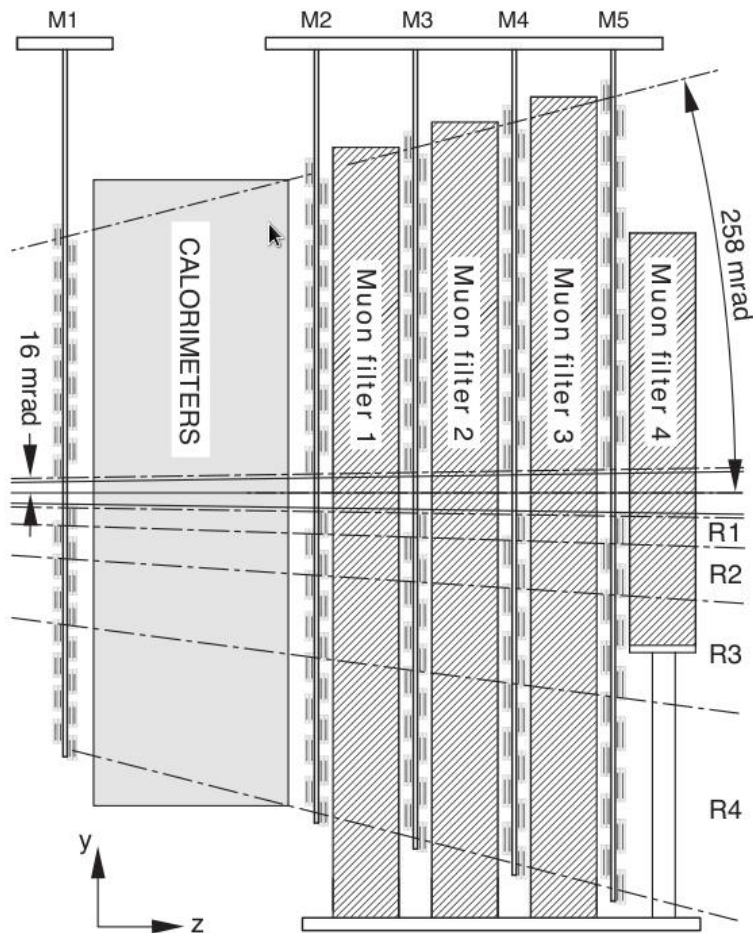


Figure 2.15: Lateral view of the muon detector. The first muon station M1 is placed before the calorimeters while the other stations are placed at the end of the LHCb detector [46].

Muon-ID algorithm performances

The algorithm of muon identification in the hardware trigger starts from the hits in the M3 station. For each hit, a straight line is extrapolated to the interaction region defining a "field of interest", that takes into account also the magnetic field kick, around such a trajectory. Hits coming from long and downstream tracks that are found around the extrapolated trajectory are fitted together to form a muon track. To consider the track as a muon it is requested to have hits in M1-M3 if the track momentum is between 3 and 3.5 GeV/c and in M1-M4 if the track momentum is between 3.5 and 4.5 GeV/c. Finally, it is required to have hits in all the five chambers if the track momentum is higher than

4.5 GeV/c. After this, complex algorithms compute the muon likelihood for each muon track, used as a particle identification discriminator.

2.2.9 Trigger in LHCb

As already mentioned, the production cross-section of $b\bar{b}$ and $c\bar{c}$ pairs are quite large, but they represent the 10% of the total pp inelastic cross-section. For this reason is necessary a good trigger system in order to accept only the interesting events and rejecting the other ones. High ratios in the LHC have to be triggered for this reason is necessary to have a trigger that works at bunch crossing frequency. In order to reach this frequencies is necessary to divide the trigger into different levels, each processing the output of the previous one. The LHCb levels are three.

Level-0 (L0): this is the first trigger level and it is based on custom electronics. It is designed to perform a first filtering of the events, reducing the input rate of about 40MHz to 1MHz.

High Level Trigger 1 (HLT 1): this is the second trigger level and it is software based. The task of HLT1 is to filter events in an inclusive way and to reduce the rate of accepted events to 50 KHz.

High Level Trigger 2 (HLT2): this is the last trigger level and it is completely software based. The HLT2 apply an exclusive selection of beauty and charm decays, performing a full reconstruction of the events which is finally sent to mass storage. At the beginning of Run-1 HLT2 operated with an output rate of about 3.5kHz. Improvements have been made over the years and the output rate have been increased up to about 12.5 kHz.

The Level-0 trigger

The L0 trigger uses information coming mainly from the tracking system and from the calorimeter system. In fact, at this level, the trigger decides to keep or discard events based on measures of p_T and E_T of the particles composing the event. The system uses three independent systems running in parallel:

L0Photon/Electron This trigger uses the information given by the SPD, PS and ECAL detectors. Custom boards are programmed to measure the energy of electromagnetic showers. The event is accepted if there is at least one cluster with E_T greater than a certain threshold.

L0Hadron This trigger exploits the information given by the HCAL detector. The way in which it works is the same as the electron/photon trigger: the event is accepted if there is at least one cluster with enough transverse energy.

L0Muon It uses the information given by the five muon stations. Tracks are reconstructed defining field of interest around particle hits and then connecting hits in the same field of interest. Events are accepted if at least one muon candidate has a transverse momentum exceeding a given threshold. Moreover, the trigger contains a line to select muon pairs, asking that the sum of their transverse momentum is greater than a threshold.

The High Level Trigger 1

The task of this trigger level is to reduce the input rate from the L0 trigger to a more manageable level. This is done rejecting events with an OT occupancy larger than 20%, because they would take more than the ~ 25 ms allowed to the HLT1 to take a decision. After this first rough selection, the remaining events are reconstructed, considering that:

- B hadrons and their production mechanism imply that the particles produced in their decays have a large momentum p and transverse momentum p_T compared to other hadrons composed by light quarks.
- The average decay length of B hadrons produced at the LHC is about 1 cm. As a consequence, their decay products will have a large impact parameter (IP) with respect to their primary vertex (PV).
- VELO reconstruction time is fast enough to allow the full information on the primary vertex to be used by the HLT1.
- The full reconstruction can be performed only for a limited number of tracks due to limited time available.

The last two points are the reason why the reconstruction is divided in two steps. In the first step VELO tracks and PV are reconstructed. The tracks are selected requiring large impact parameter with respect to the closest PV and a minimum number of hits in the sub-detector. If the difference between the expected and observed number of hits in the VELO is greater than a certain value, the track is rejected. For example, a typical choice of the cut values used is: $IP > 125\mu\text{m}$, $N_{\text{hits}}^{\text{obs}} > 9$ and $N_{\text{hits}}^{\text{exp}} - N_{\text{hits}}^{\text{obs}} < 3$. After this, forward reconstructed tracks are further selected, requiring minimal p and p_T

thresholds. Finally, remaining tracks are fitted using a bi-directional Kalman filter⁴ with outlier removal, in order to obtain an offline-quality value for the tracks (χ^2) as well as an offline-quality covariance matrix at the first state of the tracks, allowing a cut on the IP significance squared ($\chi^2(IP)$). Cut on $\chi^2(IP)$ is very efficient in rejecting background, while track χ^2 is suitable in rejecting ghost tracks.

The High Level Trigger 2

Its filtering is mainly based on three inclusive selections, the so-called topological lines. In addition, a few dedicated lines for the LHCb core analysis are used.

Topological lines consist in the building of multi-body candidates with the following strategy:

- two particles combined to form a two-body object;
- another input particle is added in order to form a three-body object and so on;
- the pion mass hypothesis is adopted for all tracks.

In this way, n -body objects are built combining the $(n-1)$ -body candidate with another particle (it saves CPU time with respect to combining n particles directly). Particles are added to an object only if they respect a cut on the distance of closest approach (DOCA). For example, the two particles forming a two body object need to have DOCA ≤ 0.15 mm.

In addition, HLT2 contains lines which exploit tracks identified as muons. Dimuon candidates are formed and, depending on their mass, cuts are applied on the flight distance and p_T of the dimuon candidate. Single muon candidates are accepted requiring a large p_T or a combination of $\chi^2(IP)$ and p_T cuts.

2.2.10 Data management and computing

The basic LHCb computing model is based on a series of distributed multi-tier regional centres of different dimensions. LHCb (as well as the other three major experiment at the LHC) requires a large amount of memory disks as well as CPU power in order to store and process the data coming from the detector and to perform analysis task (*e.g.*

⁴The Kalman filter is a recursive method for track finding and fitting. Its particularity is that the track parameters (*e.g.* momentum and direction of the track) are local and are included in the so-called state vector which evolves following the real trajectory of the particle, from the first measure to the last, including noisy effects (*e.g.* coulomb multiple scattering and energy losses).

n-tuple production). The computing system is divided in different tiers dedicated to specific duties. The Tier0 is the CERN data centre and provides to LHCb about 20% of the total resources required by the experiment and it is connected to the Tier1 centres via a private network of 10 Gbit/s optical-fiber links (LHCOPN). Moreover, Tier0 stores the RAW data, also providing a copy distributed among the Tier1 centres. There are 6 LHCb Tier1 centres worldwide that are responsible for storing a proportional share of raw and reconstructed data, as well as performing large-scale processing and storing the corresponding output. Furthermore, the Tier1 centres have to distribute the data to the Tier2 centres and to store a part of the simulated data coming from them (*i.e.* Tier2 centres mainly provide CPU resources). Each Tier1 is connected to a number of Tier2 centres, usually in the same geographical area. Finally, Tier3 resources consist of local clusters in a centre of research or a university department; they are dedicated to specific jobs needed by the research team who owns them. This system is collectively referred to as the World LHC Computing Grid (WLCG).

Data processing

The data processing involves several phases that normally follow each other in a sequential manner. The real raw data come from the detector and they are reconstructed via the online Event Filer Farm. Obviously, the first step is to collect the events of interest with an appropriate trigger system. The raw data are then processed using optimized and highly specialized algorithms implemented by the HLTs. The software applies the necessary calibration corrections during the reconstruction of the properties of the particle and imposes requirements based on physics criteria. The raw events accepted by the trigger are then transferred to the CERN Tier0 centre in order to be archived and afterwards forwarded to the Tier1 centres for further processing.

For what concerns the simulated data, the events are generated from a simulation of the LHCb detector, that includes the best understanding of the LHCb detector response, trigger response and passive material budget. The format of this type of data is the same of raw data.

Whether the data are real or simulated, they must be reconstructed in order to provide physical meaningful quantities: for example, one must determine the energy of electromagnetic and hadronic showers measuring calorimeter clusters, or hits in the tracking system have to be associated to tracks. Furthermore, the information about PID coming from the RICH sub-detectors must also be reconstructed to provide particle identification. The reconstruction process produces a new type of data, the so-called Data Summary Tape (DST).

The information contained in the DST (tracks, energies, clusters, PID) is further analysed with specific algorithms, in order to identify candidates that could form composite particles. These algorithms are designed to select only certain categories of events (*e.g.* the B2HH algorithm selects only B candidates decaying to two hadrons) and are called *stripping lines*. Such lines are written for each channel of interest and they produce the output used for further analyses. The output of the stripping stage is referred to as full DST. In addition, an event tag is also created for faster reference to the selected events. The tag contains a little summary of the event characteristics together with the results of the pre-selection algorithms and a reference to the events contained in the DST dataset. In Run-2, few changes to the data flow included the possibility to perform the full event reconstruction in the trigger, thus bypassing the offline reconstruction and discarding the raw event. This new strategy is particularly interesting for charm physics that mostly suffers the trigger output rate constraints. In the *Turbo stream* [47], the HLT directly writes out a DST containing all information necessary for analyses, and this allows an increased output rate and thus higher average efficiencies. Event pre-selection algorithms (lines) are used for data reduction and designed to identify specific decay channels. The sample of data used in this thesis comes from various Turbo stream lines, as described in Chapter 3.

Chapter 3

Analysis and results

3.1 Introduction

The research for CP violation in the Cabibbo-suppressed $D^+ \rightarrow \phi\pi^+$ and $D_s^+ \rightarrow K_s^0\pi$ decays make use of Cabibbo-favoured (CF) control samples $D_s^+ \rightarrow K_s^0\pi^+$ and $D_s^+ \rightarrow \phi\pi^+$ decays, to constraint the detection and production asymmetries.

CP -violation is expected to be in the range $10^{-3} \div 10^{-4}$ in the SM [20], therefore the amount of CP violation in the CF decay can be assumed to be negligible, if compared to the CS ones. The analysis presented in this document is based on data collected by LHCb in Run 2 during 2018, corresponding to approximately 2fb^{-1} of integrated luminosity.

The CP asymmetries are measured from the so-called raw asymmetries of signal decays after subtracting possible nuisance asymmetries due to production and detection effects using the control samples. The kinematic of the $D_s^+ \rightarrow K_s^0\pi^+$ ($D_s^+ \rightarrow \phi\pi^+$) samples is weighted to match that of the $D^+ \rightarrow \phi\pi^+$ ($D^+ \rightarrow K_s^0\pi^+$) sample to ensure an accurate cancellation of the nuisance asymmetries.

3.2 Analysis Overview

The raw asymmetry between the observed yields, N , of $D_{(s)}^+ \rightarrow f^+$ and $D_{(s)}^- \rightarrow f^-$ decays, defined as

$$A(D_{(s)}^+ \rightarrow f^+) \equiv \frac{N(D_{(s)}^+ \rightarrow f^+) - N(D_{(s)}^- \rightarrow f^-)}{N(D_{(s)}^+ \rightarrow f^+) + N(D_{(s)}^- \rightarrow f^-)}, \quad (3.1)$$

receives contribution from the CP asymmetry

$$A_{CP}(D_{(s)}^+ \rightarrow f^+) \equiv \frac{\Gamma(D_{(s)}^+ \rightarrow f^+) - \Gamma(D_{(s)}^- \rightarrow f^-)}{\Gamma(D_{(s)}^+ \rightarrow f^+) + \Gamma(D_{(s)}^- \rightarrow f^-)}, \quad (3.2)$$

and from the detection and reconstruction of the final state particles defined as

$$A_D(f^+) \equiv \frac{\epsilon(f^+) - \epsilon(f^-)}{\epsilon(f^+) + \epsilon(f^-)}. \quad (3.3)$$

For small asymmetries and assuming factorization of efficiencies for the final state of particles the raw asymmetries of these decays can be approximated as

$$A(D_s^+ \rightarrow K_s^0 \pi^+) \simeq A_{CP}(D_s^+ \rightarrow K_s^0 \pi^+) + A_P(D_s^+) + A_D(\pi^+) - A_D(\bar{K}^0) \quad (3.4)$$

$$A(D^+ \rightarrow \phi \pi^+) \simeq A_{CP}(D^+ \rightarrow \phi \pi^+) + A_P(D^+) + A_D(\pi^+) \quad (3.5)$$

The asymmetry $A_D(\bar{K}^0)$ takes into account the detection asymmetry between K^0 and \bar{K}^0 mesons due to the regeneration mechanism and the presence of mixing and CP violation in the K^0 - \bar{K}^0 system. Its value can be estimated using the known evolution of the neutral kaons system in matter and the distribution of the material inside LHCb detector. Equations 3.4 to 3.5 assume that the decay products of the K_s^0 and ϕ mesons have the same kinematic distributions such that any kinematic dependent detection asymmetry cancels in the charge symmetric final state made of two identical hadrons. Assuming negligible CP violation in Cabibbo-favoured charm transition, the decay $D^+ \rightarrow K_s^0 \pi^+$ is used as control channels to correct for detection and production asymmetries, as the raw asymmetries of the Cabibbo-favoured can be written as:

$$A(D^+ \rightarrow K_s^0 \pi^+) \simeq A_P(D^+) + A_D(\pi^+) + A_D(\bar{K}^0), \quad (3.6)$$

$$A_{CP}(D_s^+ \rightarrow \phi \pi) \simeq A_P(D_s^+) + A_D(\pi^+). \quad (3.7)$$

Combining the raw asymmetries is possible to determined the CP -asymmetries as follows

$$A_{CP}(D_s^+ \rightarrow K_s^0 \pi^+) \simeq A(D_s^+ \rightarrow K_s^0 \pi^+) - A(D_s^+ \rightarrow \phi \pi^+), \quad (3.8)$$

$$A_{CP}(D^+ \rightarrow \phi \pi^+) \simeq A(D^+ \rightarrow \phi \pi^+) - A(D^+ \rightarrow K_s^0 \pi^+), \quad (3.9)$$

where we have omitted the contributions from the neutral kaon asymmetry, which in this analysis is subtracted from any of the measured asymmetries where it is present. The nuisance asymmetries may vary as a function of the $D_{(s)}^\pm$ and the h^+ kinematics. They

could accurately cancel in the Eqs. 3.8 and 3.9.

3.3 Data samples and event selection

The analysis here presented is performed using the data recorded by the LHCb detector during 2018. The total data sample corresponds to approximately 2 fb^{-1} of integrated luminosity. The candidates for the decays of interest are reconstructed from the following dedicated triggers in order to perform an online preliminary selection. In fact there are three online algorithms called Turbo lines:

for $D_{(s)}^+ \rightarrow K_s^0 \pi^+$	of the HLT2CharmHaDp2KS0pip_KS0LLTurbo
for $D^+ \rightarrow \phi \pi^+$	of the HLT2CharmHaDpToKmKpPipTurbo
for $D_s^+ \rightarrow \phi \pi^+$	of the HLT2CharmHaDspToKmKpPipTurbo

where $K_s^0 \rightarrow \pi^+ \pi^-$ decays are always reconstructed using pairs of pions made of long tracks¹ to limit the material interactions and therefore the size of the neutral kaon asymmetry. The requirements applied in the online selection are reported in the Table 3.1 and 3.2 for $D_{(s)}^+ \rightarrow K_s^0 h^+$ and $D_{(s)}^+ \rightarrow \phi \pi^+$, respectively. Variables used include: the flight distance χ^2 from the best primary vertex (BPVVD χ^2); the proper lifetime of the particle (BPVLTIME); the direction angle between the momentum and displacement vector from the Primary vertex PV (DIRA) and the impact parameter $\chi^2 \text{IP(PV)}$, which is the minimum change in χ^2 when the particle is included in the vertex fit to the PV. VZ is the decay vertex position of the K_s^0 projected along the z -axis. $\text{DLL}_{K\pi}$ is the likelihood variable that describes the probability of a track to be a kaon (if the value is greater also the probability is). The information of this variable is based on the system of the RICH detectors. The selection requirements consider the different D^+ and D_s^+ lifetime, in fact, they are assumed to be independent from the invariant mass in the following. Therefore, the invariant-mass distributions will always be shown jointly for the D^+ and D_s^+ samples.

¹A long track is a track reconstructed using all the tracking system hence the K_s^0 considered decays in the VELO system.

Particle	Variable	Requirement
$D_{(s)}^+$	Mass	[1789, 2049] MeV/ c^2
	Flight-Distance χ^2	> 30
	Decay Time	> 0.25 ps
	Direction Angle	17.3 mrad
K_s^0	$ m(\pi^+\pi^-) - m_{K_s^0}^{PDG} $	< 35 Mev/ c^2
	Impact-Parameter χ^2	> 9
	Decay-Time (wrt th PV)	0.5 ps
	z coordinate of the decay vertex	[-100, 500] mm
	Vertex fit	< 30
Bachelor h^+	DLL $_{K\pi}$	< 5(π) or > 5(K)
	Impact-Parameter χ^2	36
	p_T	200 Mev/ c
K_s^0 decay products	Track-fit χ^2/ndf	< 3
	Impact-Parameter χ^2	> 36
	Track type	<i>long</i>

Table 3.1: Online trigger requirements utilized to select $D_{(s)}^+ \rightarrow K_s^0 h^+$ decays.

Particle	Variable	Requirement
D^+	Mass	[1789, 2949] MeV/ c^2
	Flight-Distance χ^2	> 150
	Decay Time	> 0.4 ps
	Direction Angle	10.0 mrad
	Vertex fit χ^2/ndf	< 6
D_s^+	Mass	[17792159] Mev/ c^2
	Flight-Distance χ^2	> 100
	Decay-Time	> 0.2 ps
	Direction angle	< 14.1 mrad
	Vertex fit χ^2/ndf	< 6
	DLL $_{K\pi}$	< 5(π) or > 5(K)
	Impact-Parameter χ^2	36
	p_T	200 Mev/ c
Decay products	$\sum p_T$	> 3 GeV
	DLL $_{K\pi}$	< 5(π) or > 5(K)
2 out of 3	Impact-Parameter χ^2	> 4
	Impact-Parameter χ^2	> 10
1 out of 3	p_T	> 400 Mev/ c
	Impact-Parameter χ^2	> 50
	p_T	> 1 Gev/ c

Table 3.2: Online trigger requirements utilized to select $D_{(s)}^+ \rightarrow K^+ K^- \pi^+$ decays.

3.4 Cut-based selection and analysis

To exclude kinematic regions where large detection asymmetries are present, the bachelor hadron is required to be within the fiducial region defined in ref. [48]. The aim of this requirement is to avoid all of the secondary or thirdly decay products that could interfere with the measure. Using the Boolean variable defined as

```
FiducialCut = !inDeadRegion & !(closetoBeamPipe & closetoBeamPipeVertical)
```

Where with the expression `inDeadRegion` corresponds to $|p_x| > 0.317(p - 2400)$ MeV/c, with `closetoBeamPipe` $|p_x| < 0.01605 p_z + 497$ MeV/c and `closetoBeamParticleVertical` $|p_y/p_z| < 0.02$. The requirements removes respectively about 22% and 6% of the $D_{(s)}^+ \rightarrow K_s^0 \pi^+$ and $D_{(s)}^+ \rightarrow \phi \pi^+$. In Fig. 3.2 is shown the effects of their requirements and the (px, pz) plane of the h^+ bachelor. Another requirements consist in removing secondary $D_{(s)}^+$ decaying from beauty-hadrons. For this reason is requested that the Transverse Impact Parameter (TIP) is smaller than $40 \mu\text{m}$. The TIP is defined as the distance of closest approach of the trajectory of the $D_{(s)}^+$ meson to the beam axis, *i.e.*

$$TIP = \frac{\hat{n}_z \otimes \vec{p}}{|\hat{n}_z \otimes \vec{p}|} (\vec{x}_{DV} - \vec{x}_{PV}), \quad (3.10)$$

where \vec{p} is the momentum vector of the $D_{(s)}^+$ meson, \hat{n}_z is the unit vector along direction of the beam axis, and \vec{x}_{DV} (\vec{x}_{PV}) is the vector defining the position of $D_{(s)}^+$ decay vertex (portion of PV).

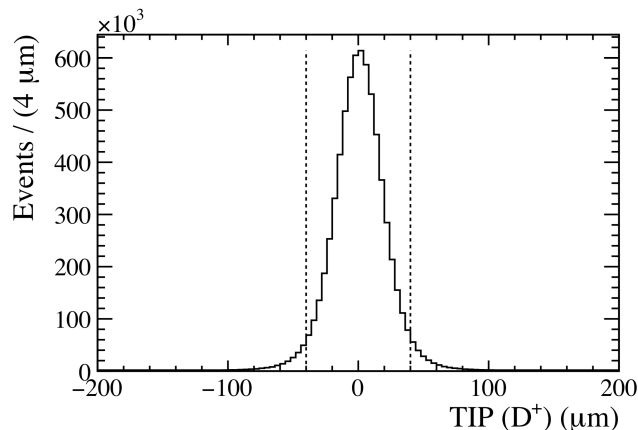


Figure 3.1: Distribution of the TIP for the $D_{(s)}^+ \rightarrow K_s^0 \pi^+$ candidates reconstructed in a subsample of 2018 magnet-down data as example of. Vertical dashed lines show the boundaries set to reject secondary $D_{(s)}^+$ mesons derived from beauty-hadrons.

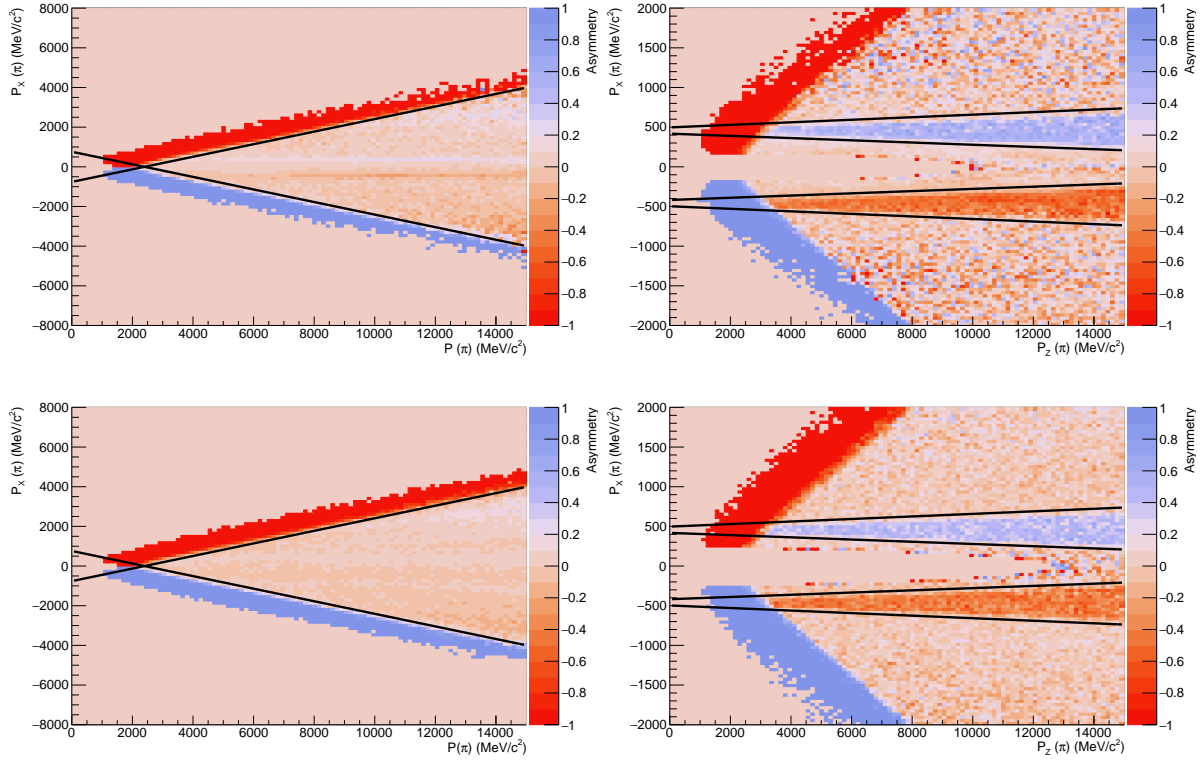


Figure 3.2: Distributions of the raw asymmetries in the (left) (p_x, p) plane and (right) (p_x, p_z) plane of the bachelor hadron, separately for (top) $D_{(s)}^+ \rightarrow K_s^0 \pi^+$ and (bottom) $D_{(s)}^+ \rightarrow \phi \pi^+$ candidates reconstructed in a subsample of 2018 magnet-down data as an example. The black lines show the boundaries of the large asymmetry regions which are excluded by the fiducial cuts.

Another important effect to be considered is the possible interaction of particles with the RF foil of the VELO detector. Those interactions derives produce unwanted charmed D mesons or other particles that mimic the signal. In order to remove those candidates, the signed distance R_{xy} between the D^+ decay vertex (DV) and the PV in the transverse plane defined as

$$R_{xy} = \text{sgn}(DV_x) \sqrt{(DV_x - PV_x)^2 + (DV_y - PV_y)^2} \quad (3.11)$$

is used. This allows to reject all the particles produced from secondary interaction with the RF foil. As shown in Fig. 3.3, all the particles that have R_{xy} greater than 5mm are rejected.

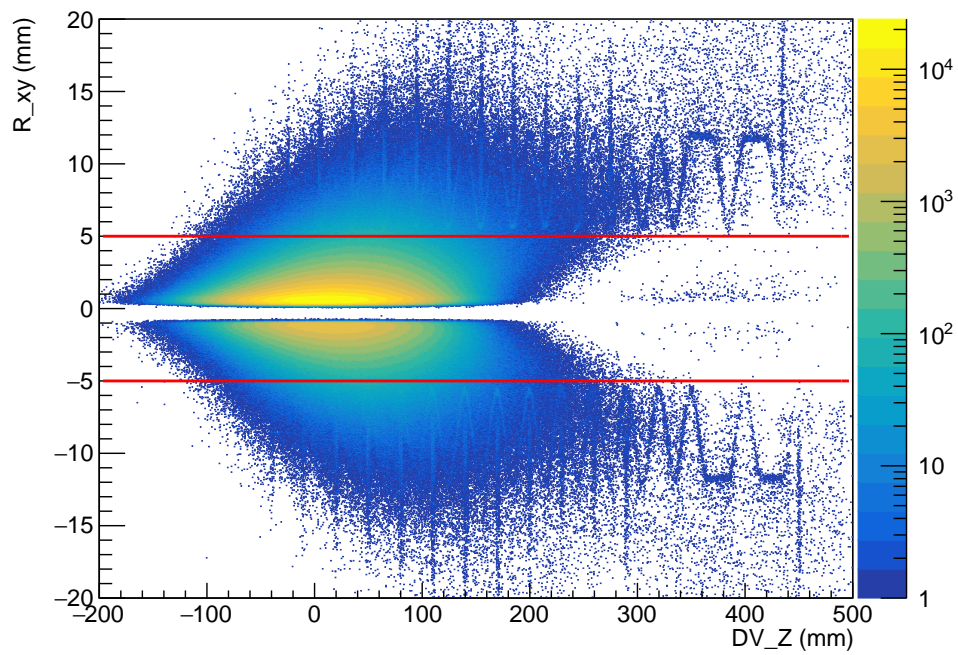


Figure 3.3: Distribution of signed radial distance, R_{xy} , for D^0 decay vertices. The visible structures are due to secondary interaction with the RF-foil and to the VELO layers. The red line represents the requirement applied, $|R_{xy}| < 5$ mm.

3.5 Selection of the $D_{(s)}^+ \rightarrow K_S^0 \pi^+$

Concerning the $D_{(s)}^\pm \rightarrow K_S^0 h^\pm$, the charmed mesons are reconstructed to form a $K_S^0 \rightarrow \pi^+ \pi^-$ candidate combined with a bachelor charged hadron. All the tracks are required to be categorized as *long tracks* and the K_S^0 mass is constrained to its known value when the $D_{(s)}^\pm$ vertex is formed. For this reason the invariant mass of the $\pi^+ \pi^-$ pair is required to be within three standard deviations of the invariant mass resolution model from the nominal value of the K_S^0 mass.

The selection of those decays consist in several criteria aimed to reduce the background from specific processes that could take place in these interactions. The criteria adopted are essentially analysis requirements, in fact, in order to reduce the background coming from $D_{(s)}^+ \rightarrow \pi^+ \pi^- \pi^+$ the mass of the pions forming the K_S^0 candidate have to be within $15 \text{ MeV}/c^2$ of the nominal K_S^0 mass and have a flight distant greater than 20mm.

Particle	Variable	Requirement
$D_{(s)}^\pm$	TIP	$< 40\mu\text{m}$
K_S^0	$ m(\pi^+ \pi^-) - m_{K_S^0}^{PDG} $	$> 15\text{MeV}$
	Flight Distance	$> 20\text{mm}$
Bachelor π^+	Fiducial cuts	yes

Table 3.3: Offline selection for $D_{(s)}^\pm \rightarrow K_S^0 \pi^+$.

After this selection, for this analysis is utilized a neural-network, based on the Multilayer Perceptron Algorithm (MPA) available in the TMVA package of Root ???. This tool is used to reduce the combinatorial background under the $D_s^+ \rightarrow K_S^0 \pi^+$ peak. The training of the MPA has been performed using background-subtracted candidates for the signal proxy and sideband candidates for background one. In this analysis it has been utilized the sideband-subtraction method to obtain the signal distribution. Two signal regions $[1848, 1888] \text{ MeV}/c^2$ for D^+ candidates $[1948, 1988] \text{ MeV}/c^2$ for D_s^+ candidates, the three background region $[1808, 1828] \text{ MeV}/c^2$, $[1908, 1928] \text{ MeV}/c^2$ and over $2000 \text{ MeV}/c^2$ (where the first two are used for D^+ candidates and the last for D_s^+ candidates) are also considered. The method consists in subtracting the distribution of the variable used for the training of the MPA between signal and background region with a proper weight. the main difference between the two decays consists in the D_s^+ meson having a lifetime that is about two times shorter than that of the D^+ meson. For this reason, in the training it is avoided the usage of input variables that are correlated with the decay time. To ensure no bias in the background mass shape after the MPA selection,

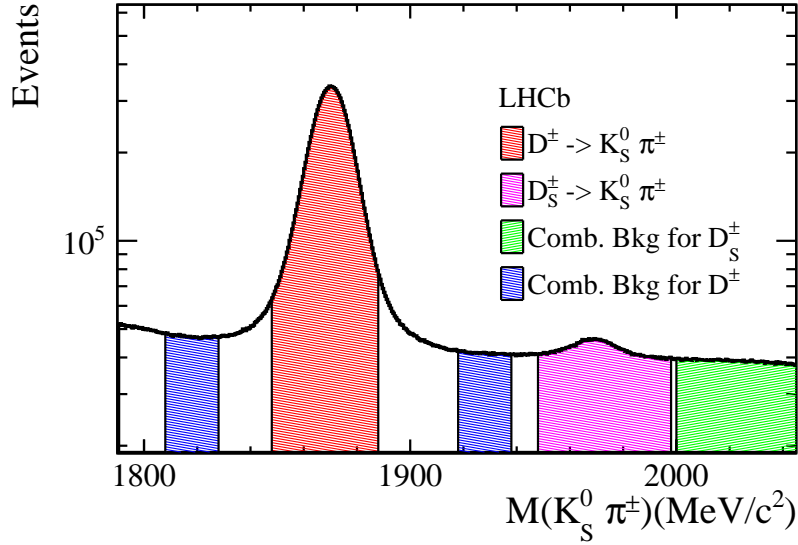


Figure 3.4: Mass invariant plot with highlighted the signals regions and sidebands utilized for the TMVA analysis.

a check on the correlation of the variable output of MPA with the $K_S^0 h$ mass has been performed. The neural network is trained on 40k $D^+ \rightarrow K_S^0 \pi^+$ background-subtracted and 40k background candidates randomly sampled from 2018 data. Input variables used in the training for background region are shown in Fig. 3.7 and reported in Table 3.5 together with the separation power defined as

$$\langle S^2(y) \rangle = \frac{1}{2} \int \frac{[\text{pdf}_S(y) - \text{pdf}_B(y)]^2}{\text{pdf}_S(y) + \text{pdf}_B(y)} dy, \quad (3.12)$$

where $\text{pdf}_{S,B}$ are the signal and background probability density functions. The resulting output distribution of the MPA response (BDTG), separately for signal and background, and for training and testing samples, are shown in the Fig. 3.5. The requirement on the BDTG is optimized by maximizing the significance $S/\sqrt{S+B}$, where S is the signal and B the combinatorial background yields observed in the $K_S^0 \pi^+$ -mass range $[1.93, 2.01] \text{ GeV}/c^2$. The maximum is 0.7 for the 2018 sample. Applying a requirement $\text{BDTG} > 0.7$, an improvement on S/B of a factor 2 with respect the selection without MPA is observed.

The final set of variables chosen is listed together with their separation power Figure 3.7 and Table 3.5.

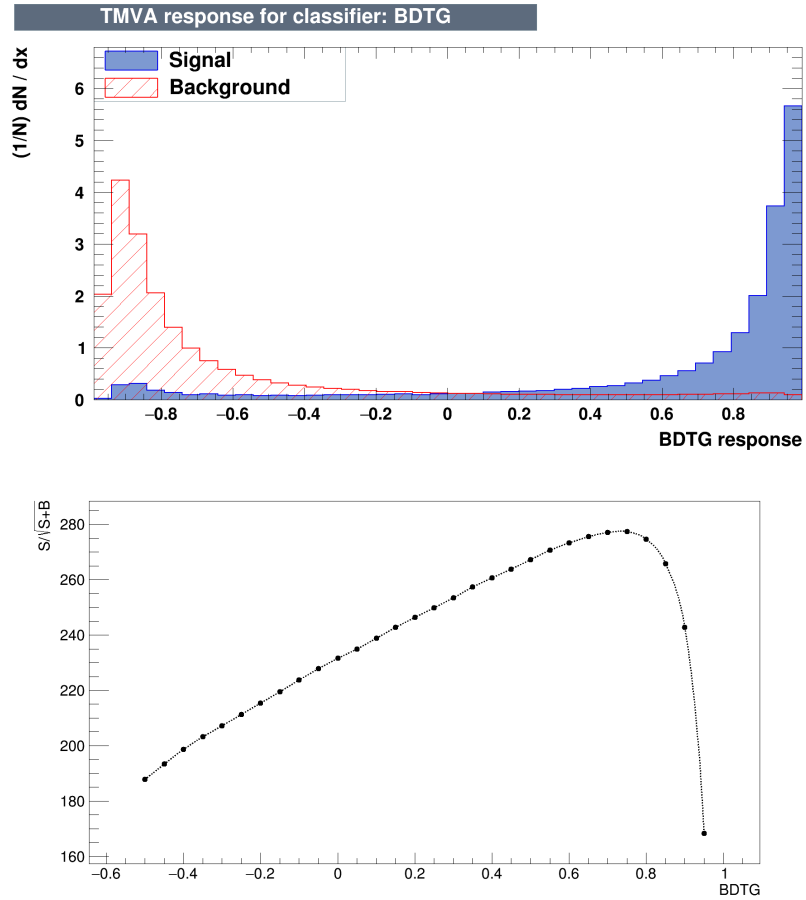


Figure 3.5: (Top) Neural-network output distribution, separately for $D^+ \rightarrow K_s^0 \pi^+$ signal and background and for training and testing samples. (Bottom) $S/\sqrt{S+B}$ vs neural network output of the $D_s^+ \rightarrow K_s^0 \pi^+$ decay. The maximum of the function is at 0.75.

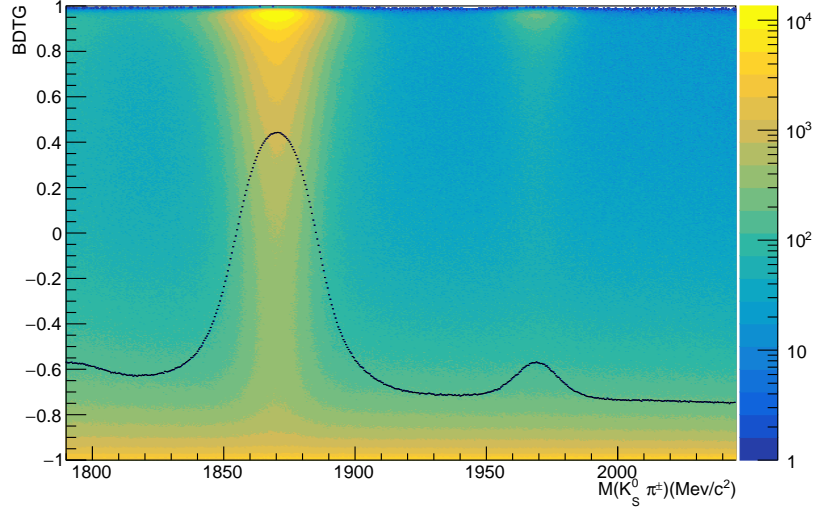


Figure 3.6: BDTG distribution and the BDTG average value (black line) as a function of $M(K_S^0 \pi^+)$ for $D_{(s)}^\pm \rightarrow K_S^0 \pi^\pm$.

Code variable	Variable	Separation power (%)
Dplus_DIRA_OWNPV	$D^+ \cos(DIRA)$	36
hplus_PT	P_{Th^+}	31
Cos_PI_PI	$\cos(\theta)_{K_S^0 \pi^+}$	30
Dplus_ETA	η_{D^+}	21
hplus_P	P_h^+	20
KSO_P	$P_{K_S^0}$	15
KSO_PT	$P_{TK_S^0}$	14
Dplus_PT	P_{TD^+}	14
hplus_ProbNN	Prob that is h^+	12
Dplus_ENVDVERTEX_CHI2	D_s^+ vertex χ^2	10
KSO_FD_Z	flight distance K_S^0	7
Cos_KSO_PI	$\cos(\theta)_{\pi^+ \pi^-}$	6

Table 3.4: variables used as input for the MVA training ordered by their separation power.

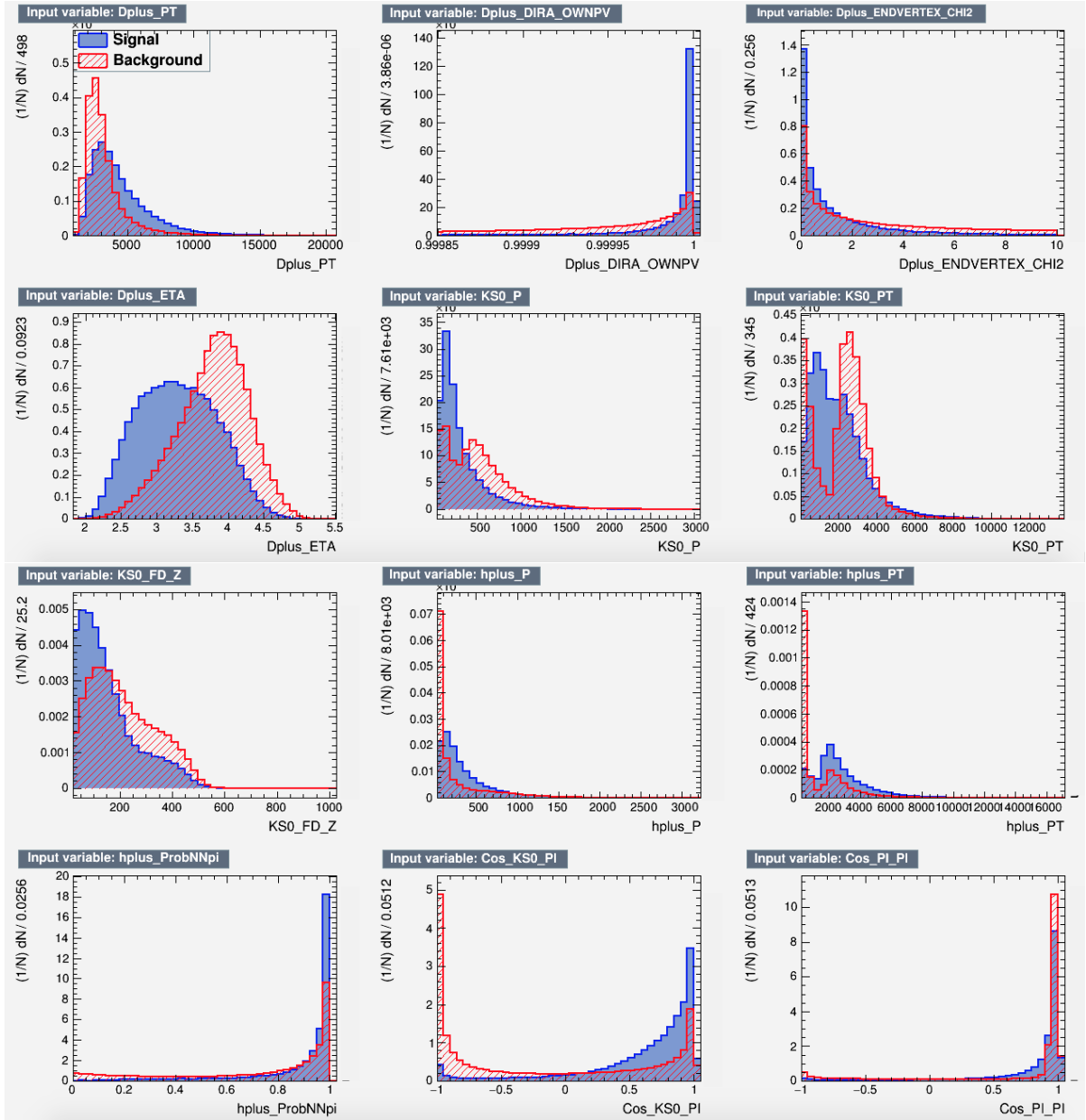


Figure 3.7: Signal and background distributions of the input variables chosen for the MVA selection in the $D_{(S)}^{\pm} \rightarrow K_S^0 \pi^{\pm}$ sample. The definition of the variables are reported in Table 3.5.

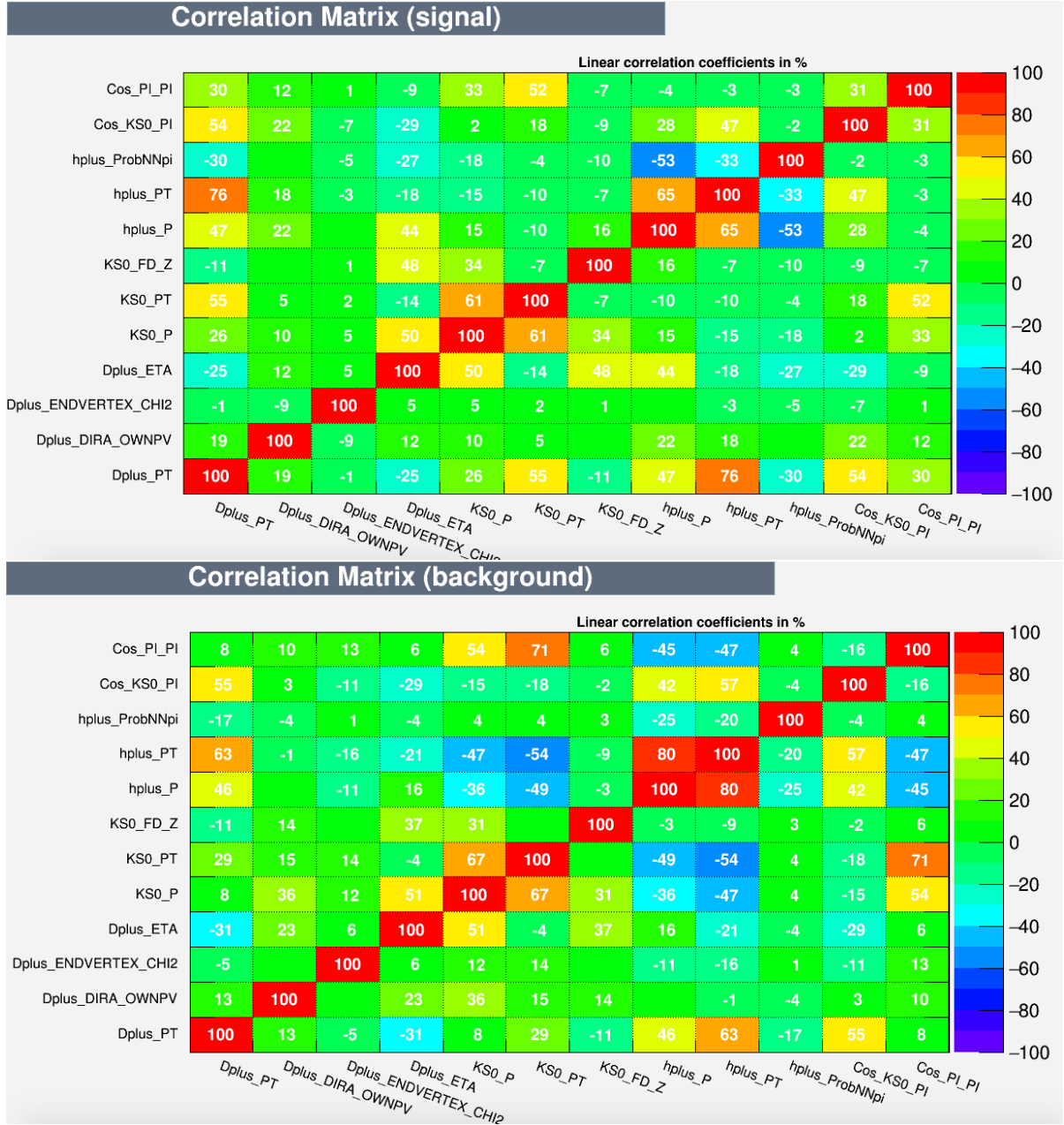


Figure 3.8: Linear correlation matrix of the input variables chosen for the MVA selection in the $D_S^\pm \rightarrow K_S^0 \pi^+$ sample. The 2018 sample is here reported. The definition of the variables are reported in Table 3.5.

3.5.1 Physical background

The K_s^0 -mass requirement applied in the analysis is efficient to reduce a physical background coming from the $\Lambda_c^+ \rightarrow \Lambda(\rightarrow p\pi^-)\pi^+$ decays, where the proton is misidentified as a pion. If two particles X and Y originate from the two-body decay of a common mother P of mass m_P , then $M_{XY} = M_P$. The wrong identification of a particle from a two bodies decay results in a shifting of the invariant mass of the other daughter particles X_1 and Y_2

$$M^2(P \rightarrow XY) [P \rightarrow X_1Y_2] = m_P^2 - \Delta M^2 \quad (3.13)$$

and this shift depends on the momentum imbalance defined as

$$\beta = \frac{p_X - p_Y}{p_X + p_Y}, \quad (3.14)$$

where X and Y are the two daughter particles of the corrected hypothesis of the decay. The shift can be calculated as a function of the corrected daughter particles X and Y and the uncorrected hypothesis given by the misidentified ones X_1 and Y_2

$$\begin{aligned} \Delta M^2 &= M_{XY}^2 - M_{X_1Y_2}^2 \\ &= (m_X^2 - m_{X_1}^2) + (m_Y^2 - m_{Y_2}^2) \\ &\quad + 2p_X p_Y \left(\sqrt{1 + \left(\frac{m_X}{p_X}\right)^2} \sqrt{1 + \left(\frac{m_Y}{p_Y}\right)^2} - \sqrt{1 + \left(\frac{m_{X_1}}{p_X}\right)^2} \sqrt{1 + \left(\frac{m_{Y_2}}{p_Y}\right)^2} \right) \\ &\approx (m_X^2 - m_{X_1}^2) + (m_Y^2 - m_{Y_2}^2) \\ &\quad + p_X p_Y \left[\left(\frac{m_X}{p_X}\right)^2 + \left(\frac{m_Y}{p_Y}\right)^2 - \left(\frac{m_{X_1}}{p_X}\right)^2 - \left(\frac{m_{Y_2}}{p_Y}\right)^2 \right] \\ &= (m_X^2 - m_{X_1}^2) \left(1 + \frac{p_Y}{p_X}\right) + (m_Y^2 - m_{Y_2}^2) \left(1 + \frac{p_X}{p_Y}\right) \\ &= \frac{2}{1 + \beta} (m_X^2 - m_{X_1}^2) + \frac{2}{1 - \beta} (m_Y^2 - m_{Y_2}^2). \end{aligned} \quad (3.15)$$

All the equations utilized are reported explicitly in the Appendix. The presence of background components, the $D_s^+ \rightarrow K_s^0 K^+$ and the $\Lambda_c^+ \rightarrow K_s^0 p$ decay where the bachelor hadrons are misidentified as a pion, is considered by looking at the dependence of $K_s^0 \pi^+$ mass as a function of the momentum imbalance between the K_s^0 meson and the bachelor pion as shown in Fig. 3.9. The figure also shows the difference between before (top) and after (bottom) the MPA selection. Even if no explicit variables are used in the MPA to

reduce the physical backgrounds, the multivariate selection is able to reduce significantly these background sources. For this reason, no further selection are considered.

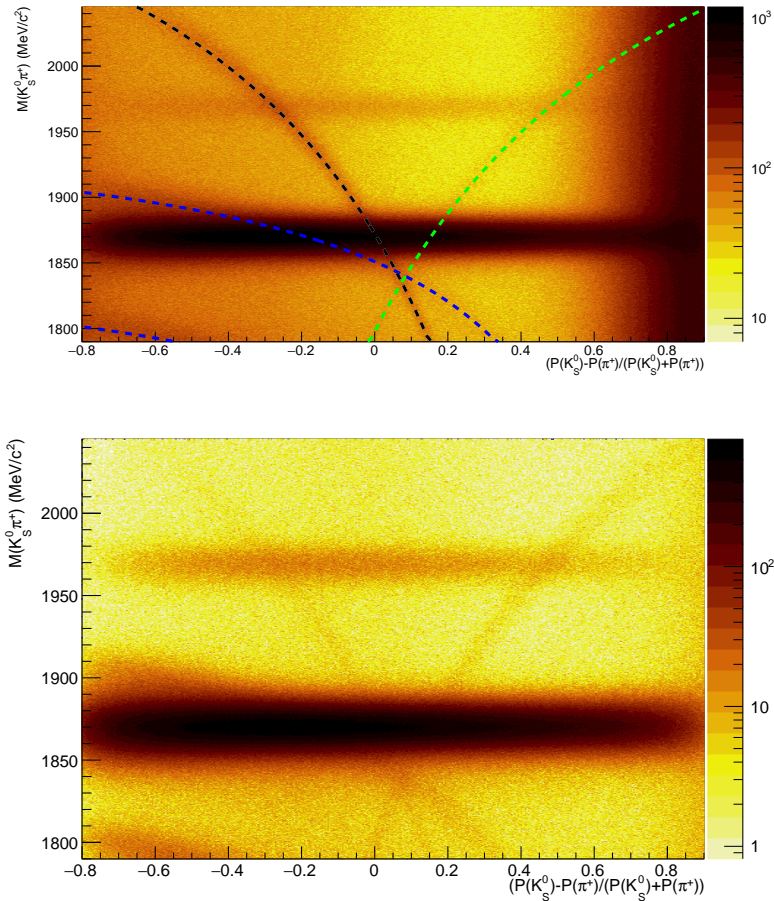


Figure 3.9: $K_s^0\pi^\pm$ invariant mass distribution as a function of the daughters particles momentum imbalance, before (top) and after (bottom) the MVA selection. The black dashed line represents the $\Lambda_c \rightarrow K_s^0 p$ decay where the proton is misidentified as a pion. The green one, instead, represents the $\Lambda_c^\pm \rightarrow \Lambda^0 \pi^\pm$ decay where $\Lambda^0 \rightarrow p\pi^\pm$ decay is wrongly identified as a K_s^0 decay. These lines are calculated on the hypothesis of perfect invariant mass resolution model. It is here reported the sample of 2018 with magnet down polarity, as an example.

3.6 Selection of the $D_{(s)}^+ \rightarrow \phi\pi^+$

The $D_{(s)}^\pm \rightarrow \phi\pi^+$ candidates are reconstructed with the different online selection for D^\pm and D_s^\pm , as reported in Table 3.2. Therefore, it is necessary to fit the two samples jointly introducing a step function at 1900 MeV/ c^2 in the fit model, to take into account the different selection efficiencies in different invariant mass window due to the trigger lines. Candidate $D_{(s)}^+$ is reconstructed from three charged tracks originating from a single vertex, since the ϕ does not travel an appreciable distance through the detector. The invariant mass of the pions pair from the ϕ is required to be within three standard deviations of the invariant mass resolution model from the ϕ nominal mass value.

For the background rejection several criteria are applied. This decays are already suppressed thanks to HTL2 with an hard cut in $DLL_{K\pi}$ to the ϕ daughters. As regards background related to the $D_{(s)}^\pm \rightarrow \phi K^\pm$ decay, it is rejected with PID requirements for the pion against the kaon hypothesis.

The rejection of $D_{(s)}^+$ mesons decaying from B mesons is ensured with requirement on the impact parameter χ^2 of the $D_{(s)}^\pm$ candidate with respect to the PV. A further irreducible background is taken into account in the fit model. It consists of the $D_{(s)}^\pm \rightarrow K^\pm K^\mp \pi^\pm \pi^\mp \pi^0$ decays where the π^0 is not reconstructed. This background lies in a region well below the nominal value of the $D_{(s)}^\pm$ invariant mass as described later. Figure 3.10 shows the $\phi\pi$ -mass distribution as a function of the momentum imbalance between the ϕ and the π momentum after the selection. Here, misidentified decays are not visible thus the remaining background is considered as only combinatorial. Furthermore, one can notice that the phase-space is limited, *i.e.* $(p_\phi - p_\pi)/(p_\phi + p_\pi)$ covers only a fraction of the interval in $[-1,1]$. This is due to the small q -value of the decay, of about 32 MeV/ c^2 .

Particle	Variable	Requirement
$D_{(s)}^\pm$	$\chi_{IP}^2(PV)$	< 9
ϕ	$ m(K^+K^-\pi^+) - m_\phi^{PDG} $	$< 10 \text{ MeV}/c^2$
bachelor hadron	fiducial cut	yes

Table 3.5: Offline selection for the $D_{(s)}^\pm \rightarrow \phi\pi^+$ decay.

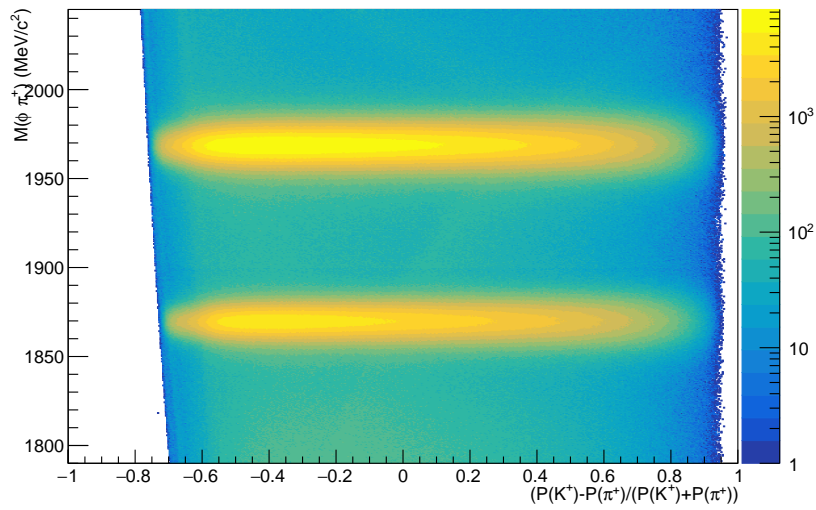


Figure 3.10: $\phi\pi$ -mass invariant mass distribution as a function of the momentum imbalance after the offline selection. The horizontal regions with high population represent the $D_{(s)}^{\pm}$ signal events.

3.7 Fit model

The raw asymmetries for the $D_{(s)}^\pm \rightarrow K_S^0 \pi^\pm$ and $D_{(s)}^\pm \rightarrow \phi \pi^\pm$ decays are determined from two separate binned extended χ^2 fits to the corresponding invariant mass distributions. All fits are performed using the RooFit framework in the 1790 - 2045 MeV/ c^2 invariant mass window. The general strategy of this analysis is to use a Monte Carlo generator in order to determine the model and the shape parameters that will be used to fit the data. Only the $D_s^+ \rightarrow \phi \pi^+$ and $D^+ \rightarrow K_S^0 \pi^+$ decays are considered as the other decays show a similar fit model. A simultaneous fit is performed to the two $V^0 h^\pm$ invariant mass distributions, where V^0 is the produced neutral meson from the decay (ϕ or K_S^0) and h^\pm are the bachelor hadrons. The Monte Carlo datasets generated for this analysis consist of about 22 millions for the $D_s^+ \rightarrow \phi \pi^+$ decay and 9 millions for $D^+ \rightarrow K_S^0 \pi^+$.

3.7.1 The Monte Carlo generation

An entirely Monte Carlo simulation of events occurring in the LHCb experiment takes a lot of computing time and making impossible to produce statistic with a reasonable time. To avoid this problem, it is used the so-called particle gun (pGun) generator. This tool permits the generation of signal particles, without the sub-leading events saving a huge amount of generation time. The fitting model consists in seven Gaussian functions. Where two Gaussian functions are convoluted with an exponential to take into account the tail of the invariant mass distribution, *i.e.*

$$F_{1(a,b)}(m|\mu, \sigma_1) = G_1(m|\mu, \sigma_1) * e^{-m\lambda_{a,b}} \quad (3.16)$$

and then summed as

$$G_1(m|\mu, \sigma_1) = f_a F_{1a} + (1 - f_a) F_{1b}. \quad (3.17)$$

The total fitting model for the signal is

$$\begin{aligned} F(m|\mu, \sigma_1 \dots \sigma_6, f_1 \dots f_5) = & f_1 G_1(m|\mu, \sigma_1) + \\ & (1 - f_1)(f_2 G_2(m|\mu, \sigma_2) + (1 - f_2)(f_3 G_3(m|\mu, \sigma_3) + \\ & (1 - f_3)(f_4 G_4(m|\mu, \sigma_4) + (1 - f_4)(f_5 G_5(m|\mu, \sigma_5) + \\ & (1 - f_5) G_6(m|\mu, \sigma_6))))). \end{aligned} \quad (3.18)$$

This function is used both for describing the D_s^+ and D^+ peaks. Figure 3.11 shows the invariant mass distributions of simulated data with the result of the fit overlaid for the $D_{(s)}^+ \rightarrow \phi \pi^+$ and $D_{(s)}^+ \rightarrow K_S^0 \pi^+$ respectively.

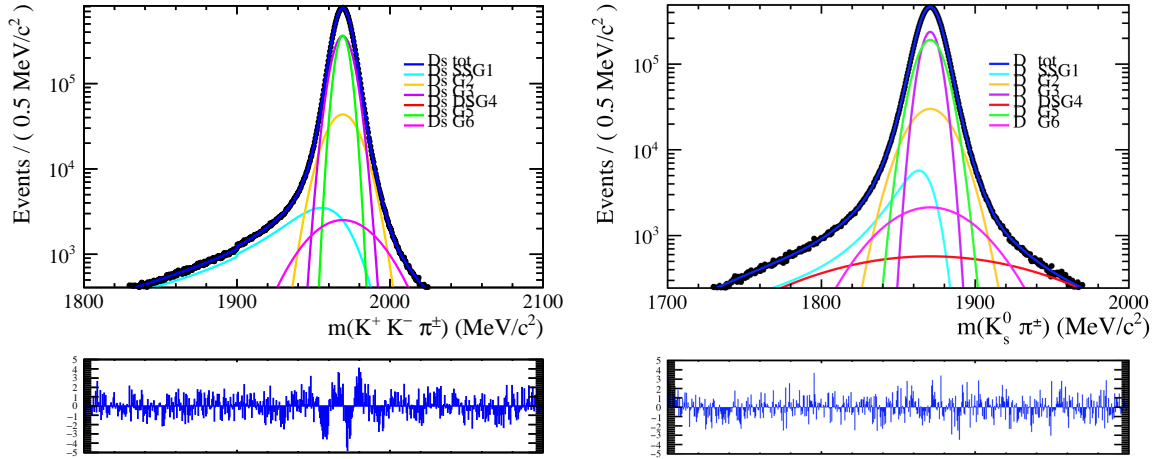


Figure 3.11: Invariant mass distribution of $D_s^+ \rightarrow \phi\pi^+$ (left) and $D^+ \rightarrow K_s^0\pi^+$ (right) simulated data with the result of the fit overlaid. The data sample corresponds to 22 and 9 million of events, respectively.

Parameter	$D_s^+ \rightarrow \phi\pi^+$ values	$D^+ \rightarrow K_s^0\pi^+$ values
$\lambda_{a,b}$	0.46	0.02
f_1	0.02	0.02
f_2	0.11	0.12
f_3	0.58	0.44
f_4	0.01	0.02
f_5	0.97	0.96
σ_1	12.46	6.67
σ_2	10.77	14.33
σ_3	6.25	5.79
σ_4	70.04	74.32
σ_5	4.21	8.50
σ_6	22.43	29.49
<i>mean</i>		

Table 3.6: Shape parameters determined from the study of MC data events for the $D_s^+ \rightarrow \phi\pi$ and $D^+ \rightarrow K_s^0\pi$ decays.

3.8 Results

Fits to the $D_{(s)}^\pm \rightarrow K_s^0 \pi^\pm$ and $D_{(s)}^\pm \rightarrow \phi \pi^\pm$ invariant mass distributions are performed to measure the raw asymmetries with the 2018 data samples, corresponding to a total integrated luminosity of approximately 2 fb^{-1} . The total fitting function is

$$F_{tot}(m) = N_{D^+} \frac{1 \pm A_D}{2} F_{D^+}(m) + N_{D_s^+} \frac{1 \pm A_{D_s^+}}{2} F_{D_s^+}(m) + N_{bkg} \frac{1 \pm A_{bkg}}{2} F_{bkg}(m) \quad (3.19)$$

where the signal function for D^+ and D_s^+ is the same described in Eq. 3.18. The description for the background is realised by means of an empirical model based on the sum of two exponential functions

$$F_{bkg}^\pm(m|\lambda_1^\pm, \lambda_2^\pm, f_1^\pm) = f_1^\pm \frac{e^{-\lambda_1^\pm m}}{n_1} + (1 - f_1^\pm) \frac{e^{-\lambda_2^\pm m}}{n_2}. \quad (3.20)$$

The low invariant mass region where are present physical backgrounds due to partially reconstructed or misidentified decays is described with an Argus function ?? convoluted with the resolution invariant mass model. The $D_{(s)}^+ \rightarrow \phi \pi$ invariant mass distribution is sculpted around $1800 \text{ MeV}/c^2$ by different trigger lines. This is taken into account in the fit by introducing a step function at $1900 \text{ MeV}/c^2$ in the invariant mass distribution with a scale factor C so that

$$F_{TOT}(m|\vec{\theta}, C) = \begin{cases} F_{TOT}(m|\vec{\theta}) & m \leq 1900 \text{ MeV}/c^2 \\ C \cdot F_{TOT}(m|\vec{\theta}) & m > 1900 \text{ MeV}/c^2. \end{cases} \quad (3.21)$$

This fitting procedure measure the raw asymmetries as reported in Tab. 3.8. $A(D_s^+ \rightarrow K_s^0 \pi^+)$ and $A(D^+ \phi \pi)$ is blinded in order to carry the analysis without any unconscious bias, because is possible that if it is expected a result, is common that the analyst unconsciously introduce a bias at the measure. The blinding procedure consist in introducing a random number included in a range between 0 and 0.1% in order to avoid this phenomenon. The $D_{(s)}^\pm \rightarrow K_s^0 \pi^\pm$ and $D_{(s)}^\pm \rightarrow \phi \pi^\pm$ fit results to the 2018 and data sample are presented separately for positive and negative charge in Figs. 3.12 and 3.13. Figures 3.14 show the raw asymmetries as a function of the invariant mass distribution with the results of the fits overlaid for the $D_{(s)}^\pm \rightarrow K_s^0 \pi^\pm$ and $D_{(s)}^\pm \rightarrow \phi \pi^\pm$ decays, respectively. Here the irregular shapes of the distributions are given by the fact that positive and negative charges have different instrumental efficiencies. As one can notice, asymmetries are well described by the fits. A summary of the total signal yields obtained from the fits is given in Tab. 3.7 and the raw asymmetry in 3.8

$D^+ \rightarrow K_s^0 \pi^+$	$D_s^+ \rightarrow K_s^0 \pi^+$
16.5 M	0.3 M
$D^+ \rightarrow \phi \pi^+$	$D_s^+ \rightarrow \phi \pi^+$
26.0 M	55 .0 M

Table 3.7: $D_{(s)}^\pm \rightarrow V^0 h^+$ signal yields obtained as result of the fits.

$A(D^+ \rightarrow K_s^0 \pi^+)$	$A(D_s^+ \rightarrow K_s^0 \pi^+)$ blind
$(0.09 \pm 0.03)\%$	$(-0.38 \pm 0.25)\%$
$A(D^+ \rightarrow \phi \pi^+)$ blind	$A(D_s^+ \rightarrow \phi \pi^+)$
$(-0.49 \pm 0.02)\%$	$(-0.30 \pm 0.01)\%$

Table 3.8: $D_{(s)}^\pm \rightarrow V^0 h^+$ raw asymmetries obtained from fits.

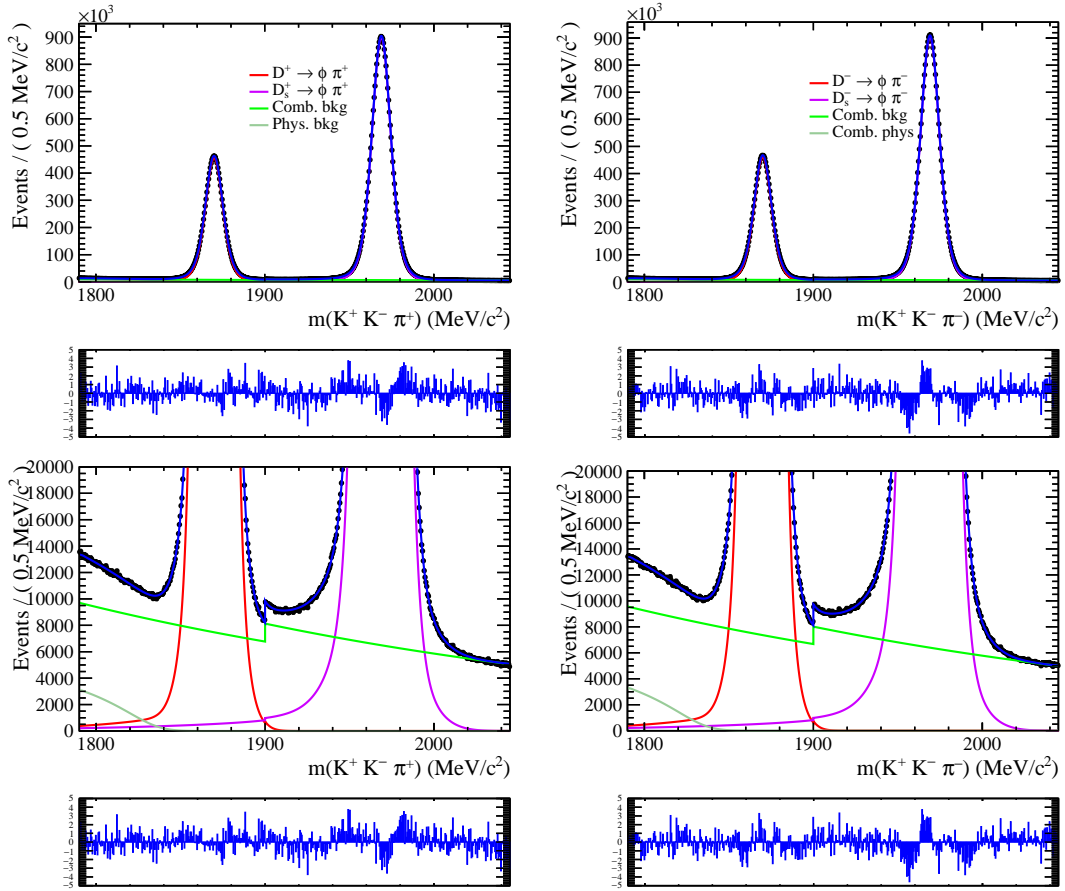


Figure 3.12: $D_{(s)}^+ \rightarrow \phi\pi^+$ invariant mass distributions with the results of the fit overlaid for the for the $D_{(s)}^+$ (left) and $D_{(s)}^-$ (right) candidates. The bottom figures residuals between data and the fitted function.

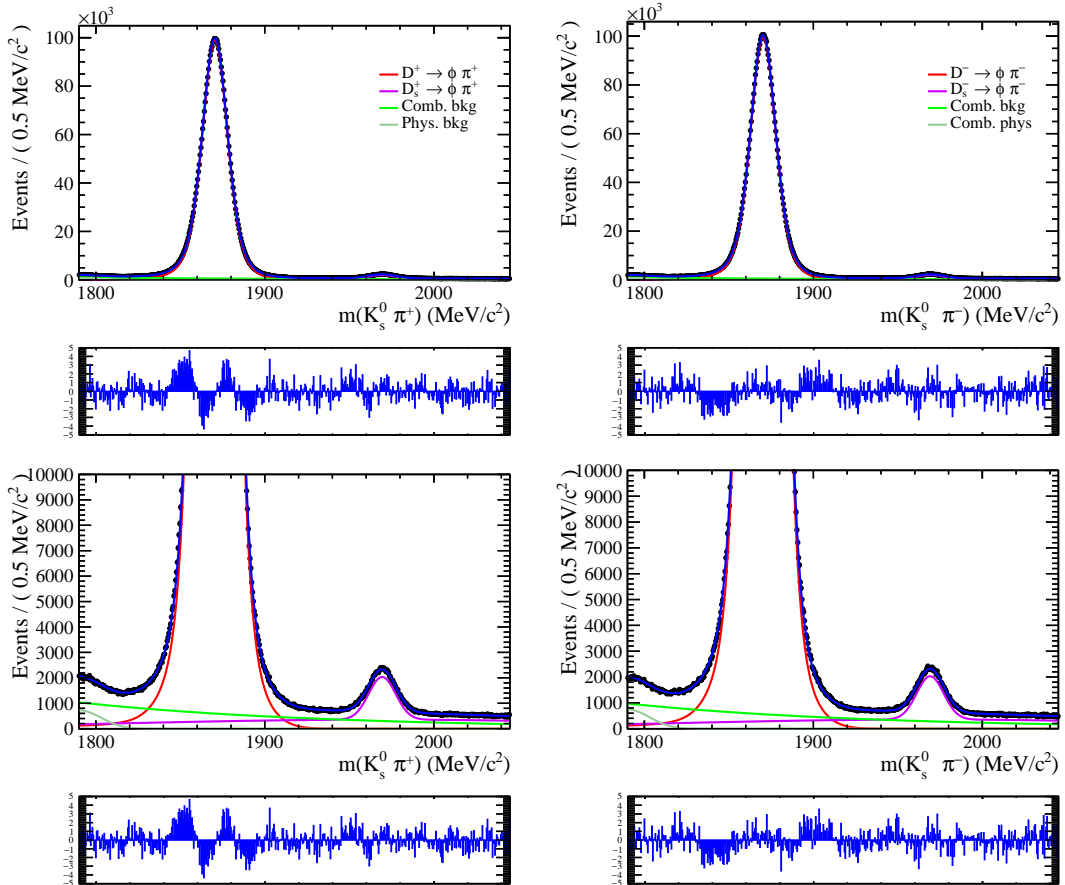


Figure 3.13: $D_{(s)}^+ \rightarrow K_s^0 \pi^+$ invariant mass distributions with the results of the fit overlaid for the for the $D_{(s)}^+$ (left) and $D_{(s)}^-$ (right) candidates. The bottom figures residuals between data and the fitted function.

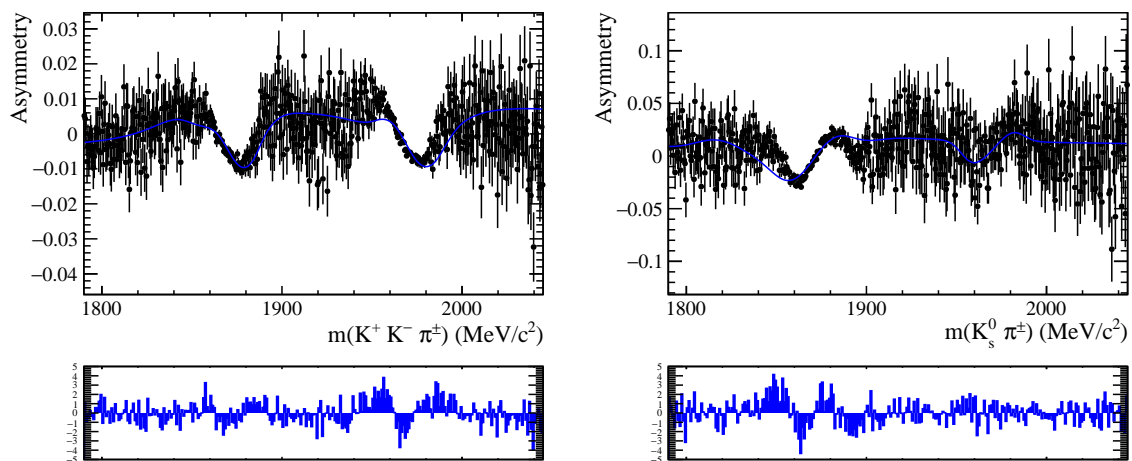


Figure 3.14: $D_{(s)}^{\pm} \rightarrow \phi \pi^+$ (left) and $D_{(s)}^{\pm} \rightarrow K_s^0 \pi^+$ (right) raw asymmetries as a function of the invariant mass.

3.9 Final Results for CP -violating asymmetries

To measure A_{CP} , the raw asymmetries obtained from fits previously described are used. The calculation of the final results need the correction given from the neutral kaon detecting asymmetry arising from the combined effect of CP violation and mixing in the neutral kaons system and the different interaction rates of K^0 and \bar{K}^0 mesons with the detector material. The uncertainty is completely dominated by the knowledge of the detector material. The value of the $A_D(\bar{K}^0)$ is taken from Ref. [49] and correspond to $A_D(\bar{K}^0) = -0.0843 \pm 0.0049$ for the $A_{CP}(D^+ \phi \pi)$ and $A_D(\bar{K}^0) = -0.0677 \pm 0.0042$ for $A_{CP}(D_s^+ K_s^0 \pi)$. The value of $A_D(\bar{K}^0)$ is subtracted from the measured raw asymmetries as described in Eqs. 3.8 and 3.9. The values of blinded A_{CP} are shown in Table 3.9. The errors reported are only statistical.

$A_{CP}(D^+ \rightarrow \phi \pi^+)$	$A_{CP}(D_s^+ \rightarrow K_s^0 \pi^+)\%$
-0.57 ± 0.04	-0.07 ± 0.25

Table 3.9: Blinded value of A_{CP} .

3.10 Systematic Uncertainties

The measured asymmetries and A_{CP} results are subject to several sources of systematic uncertainty. An overview of the main sources is reported in this section. Their evaluation are not reported as their study is beyond the aim of this thesis work.

3.10.1 K^0 interactions in VELO detector

K_S^0 and K_L^0 mesons are a mixture of K^0 and \bar{K}^0 . For this reason they could interact asymmetrically with the detector material. \bar{K}^0 mesons can be absorbed in hyperon production processes while K^0 can only scatter elastically or undergo charge exchange. It is important to note that decays of $D_{(s)}^\pm$ mesons produce a precise flavour of K^0 or \bar{K}^0 as shown in figure 1.2 and 1.3. The initially pure states of neutral kaon oscillate back forth, as they propagate through the VELO, CP eigenstates K_S^0 and K_L^0 are produced. Within the VELO, the propagating states have a non-zero chance of interacting with VELO material. The interaction of neutral kaons with matter is often called regeneration,

because it results in the production of a small number of K_S^0 mesons from an initially pure beam of K_L^0 mesons. The regenerated K_S^0 can decay into two pions miming a CP violation. The study of this decay is possible if:

- there is a true K_S^0 to two charged pions decay (CP conserving);
- the K_L^0 states interact with the VELO material and is generated as a K_S^0 which then decays into two charged pions;
- the K_L^0 states violate CP and decays with two charged pions;

One consequences of this uncertain involves the reconstruction of $D_{(s)}^+$ and $D_{(s)}^-$ meson, in fact, they could not be reconstructed with the same efficiencies. It should be noted that the K^0 detection asymmetry could theoretically vary between different $D^+(s) \rightarrow K_S^0 h^+$ modes and selections as the momentum spectra of the K_S^0 candidates are different.

3.10.2 Secondary $D_{(s)}^+$ decays

In the offline selection $D_{(s)}^+$ candidates, the $\chi^2(IP)$ requirement on the $D_{(s)}^*$ removes the majority of the background from secondary $D_{(s)}^\pm$ mesons originating from the decay of b hadron. The remaining mesons may introduce a bias in the measured CP asymmetries due to a difference in the production asymmetries for b hadrons and $D_{(s)}^\pm$ mesons. It is possible to take into account this bias modifying the production asymmetries in Eqs. 3.4,3.5 and Eqs 3.8, 3.9 as

$$A_P^{D_{(s)}^+}(corrected) = \frac{A_P^{D_{(s)}^+} + A_P^B}{1 + f} \quad (3.22)$$

where f is the fraction of secondary for $D_{(s)}^+$ candidates in a particular decay channel and A_P^B is the b -hadron production asymmetry. The fraction f can be estimated measuring D^+ , D_s^+ and b -hadron inclusive cross-sections, the branching fractions $\mathcal{B}(b \rightarrow D^\pm X)$ and $\mathcal{B}(b \rightarrow D_s^\pm X)$, where X corresponds to any other particles in the final state, the exclusive branching fractions $\mathcal{B}(D_{(s)}^+ \rightarrow V^0 h^+)$ and the estimated efficiencies.

3.10.3 Differences in signal and control channels kinematics

The production asymmetries of the $D_{(s)}^+$ candidates and the detection asymmetries of the bachelor hadrons cancel between final states if the corresponding kinematics match. This in general does not happen as shown in Figs. 3.15 where no corrections are applied. In

order to apply the corrections it is necessary to implement a so called re-weight method.

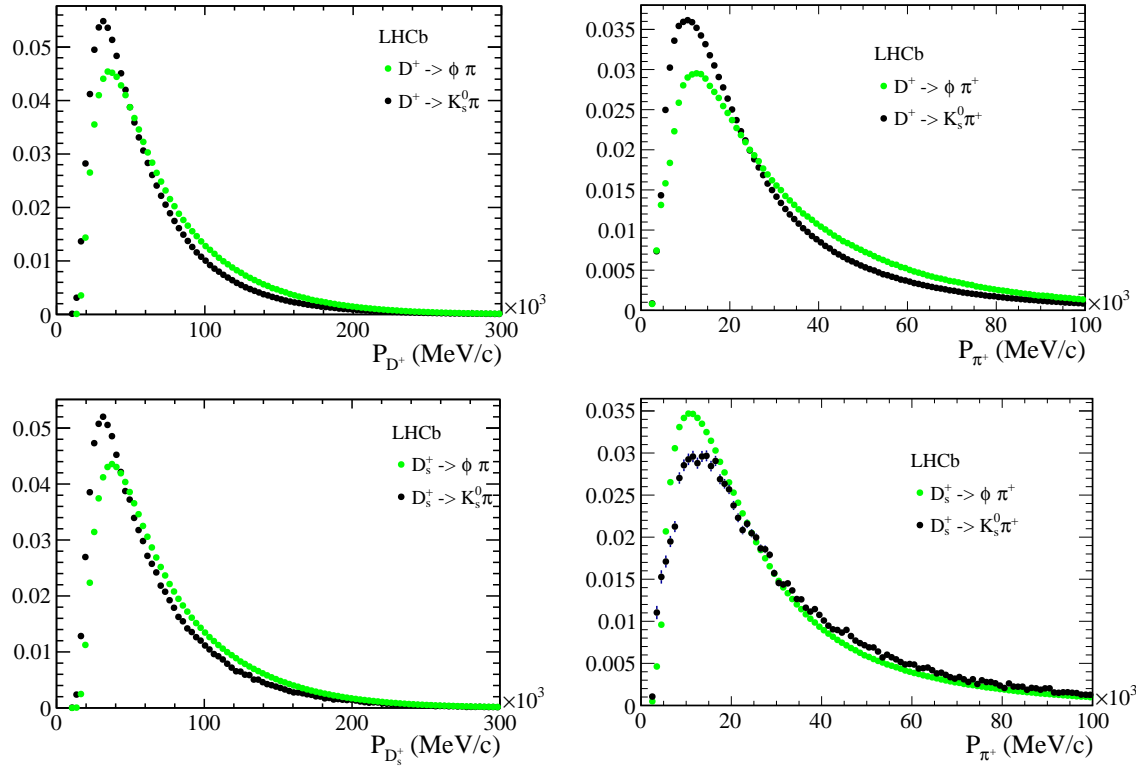


Figure 3.15: Comparison of the momentum distribution (top-left) of D^+ and (top-right) π in $D^+ \rightarrow \phi \pi^+$ CS decay and $D^+ \rightarrow K_s^0 \pi^+$ CF decay (bottom-left) and for D_s^+ and (bottom-right) π in $D_s^+ \rightarrow \phi \pi^+$ CF decay and $D_s^+ \rightarrow K_s^0 \pi^+$ CS decay.

Conclusions

In conclusion, this thesis report a preliminary measurement for the research of direct CP violation in the charm sector with the $D^+ \rightarrow \phi\pi^+$ and $D_s^+ \rightarrow K_s^0\pi^+$ decays using a data sample corresponding to about 2 fb^{-1} recorded by LHCb during the 2018.

The study of the Monte Carlo data permitted to improve the fitting model and hopefully to reduce the main systematic uncertainties. The measures reported here have to be considered preliminary and unofficial since the systematic errors have not been estimate. The blinded final measurements are

$$\begin{aligned} A_{CPblind}(D_s^+ \rightarrow \phi\pi^+) &= -(0.57 \pm 0.04)\%, \\ A_{CPblind}(D_s^+ \rightarrow K_s^0\pi^+) &= -(0.07 \pm 0.25)\%, \end{aligned}$$

assuming that CP violation in the control samples decays is negligible. In order to finalize the analysis it is necessary to complete the systematic uncertainties and the re-weighting method. These further studies will be completed within the analysis activities of the LHCb-Bologna group and the work done in this thesis will be included in a future publication. By combining this result with the previous ones performed by LHCb, it is possible to improve the final precision of about 20%.

Appendices

Appendix A

Kinematic separation of $D^\pm \rightarrow K_S^0 h^\pm$ and $K_S^0 \rightarrow \pi^+ \pi^-$ decays

The invariant mass of two particles X and Y of mass m_X and m_Y and momenta \vec{p}_X and \vec{p}_Y is defined as

$$M_{XY}^2 = \left(\sqrt{p_X^2 + m_X^2} + \sqrt{p_Y^2 + m_Y^2} \right)^2 - (\vec{p}_X + \vec{p}_Y)^2. \quad (\text{A.1})$$

If the two particles originate from the two-body decay of a common mother P of mass m_0 , then $M_{12} = m_0$. If, instead, one wrongly assigns the masses to the outgoing particles, the resulting invariant mass

$$M_{12}^2 = \left(\sqrt{p_1^2 + m_1^2} + \sqrt{p_2^2 + m_2^2} \right)^2 - (\vec{p}_X + \vec{p}_Y)^2, \quad (\text{A.2})$$

where the mass m_{X_1} (m_{Y_2}) is assigned to the particle with momentum \vec{p}_X (\vec{p}_Y), is shifted with respect to m_0 as

$$M_{X_1 Y_2}^2 = m_0^2 - \Delta M^2, \quad (\text{A.3})$$

with

$$\begin{aligned}
\Delta M^2 &= M_{XY}^2 - M_{X_1Y_2}^2 \\
&= (m_X^2 - m_{X_1}^2) + (m_Y^2 - m_{Y_2}^2) \\
&\quad + 2p_X p_Y \left(\sqrt{1 + \left(\frac{m_X}{p_X}\right)^2} \sqrt{1 + \left(\frac{m_Y}{p_Y}\right)^2} - \sqrt{1 + \left(\frac{m_{X_1}}{p_X}\right)^2} \sqrt{1 + \left(\frac{m_{Y_2}}{p_Y}\right)^2} \right) \\
&\approx (m_X^2 - m_{X_1}^2) + (m_Y^2 - m_{Y_2}^2) \\
&\quad + p_X p_Y \left[\left(\frac{m_X}{p_X}\right)^2 + \left(\frac{m_Y}{p_Y}\right)^2 - \left(\frac{m_{X_1}}{p_X}\right)^2 - \left(\frac{m_{Y_2}}{p_Y}\right)^2 \right] \\
&= (m_X^2 - m_{X_1}^2)(1 + p_Y/p_X) + (m_Y^2 - m_{Y_2}^2)(1 + p_X/p_Y) \\
&= \frac{2}{1 + \beta}(m_X^2 - m_{X_1}^2) + \frac{2}{1 - \beta}(m_Y^2 - m_{Y_2}^2),
\end{aligned} \tag{A.4}$$

where the approximation holds the first order in (m/p) and the charged momentum imbalance β is further defined as $\beta = (p_X - p_Y)/(p_X + p_Y)$. The above expression, for a $P^\pm \rightarrow X^0 Y^\pm$ decay, when using a charged $D_{(s)}$ meson, a neutral kaon and a charged pion or kaon as arbitrary mass assignments for the initial and the final state particles (*i.e.* a $D_{(s)}^\pm \rightarrow K_S^0 h^\pm$ decay), becomes:

$$M^2(D_{(s)}^\pm \rightarrow K_S^0 K^\pm)[D_{(s)}^\pm \rightarrow K_S^0 \pi^\pm] \approx m_{D_{(s)}^\pm}^2 - \frac{2}{1 - \beta}(m_K^2 - m_\pi^2), \tag{A.5}$$

$$M^2(D_{(s)}^\pm \rightarrow K_S^0 \pi^\pm)[D_{(s)}^\pm \rightarrow K_S^0 K^\pm] \approx m_{D_{(s)}^\pm}^2 - \frac{2}{1 - \beta}(m_\pi^2 - m_K^2), \tag{A.6}$$

$$M^2(\Lambda_c^\pm \rightarrow K_S^0 p)[D_{(s)}^\pm \rightarrow K_S^0 \pi^\pm] \approx m_{\Lambda_c^\pm}^2 - \frac{2}{1 - \beta}(m_p^2 - m_\pi^2), \tag{A.7}$$

$$M^2(\Lambda_c^\pm \rightarrow K_S^0 p)[D_{(s)}^\pm \rightarrow K_S^0 K^\pm] \approx m_{\Lambda_c^\pm}^2 - \frac{2}{1 - \beta}(m_p^2 - m_K^2), \tag{A.8}$$

$$M^2(\Lambda_c^\pm \rightarrow \Lambda^0 \pi^\pm)[D_{(s)}^\pm \rightarrow K_S^0 \pi^\pm] \approx m_{\Lambda_c^\pm}^2 - \frac{2}{1 + \beta}(m_{\Lambda^0}^2 - m_{K_S^0}^2). \tag{A.9}$$

For a $P^0 \rightarrow X^+ Y^-$ decay, when using a neutral kaon and a pair of charged pions as arbitrary mass assignments for the initial and the final state particles (*i.e.* a $K_S^0 \rightarrow \pi^+ \pi^-$ decay), it becomes:

$$M^2(\Lambda^0 \rightarrow p \pi^\mp)[K_S^0 \rightarrow \pi^+ \pi^-] \approx m_{\Lambda^0}^2 - \frac{2}{1 \pm \beta}(m_p^2 - m_\pi^2). \tag{A.10}$$

List of Figures

1.1	Rescaled unitary triangle corresponding to 1.28	14
1.2	Feynman diagrams of the possible CS decays for the D -meson, respectively from above $D_s^+ \rightarrow K_S^0 \pi^+$, and $D^+ \rightarrow \phi \pi^+$. The diagrams on left side are so called tree diagrams and on the right side the so called penguin diagrams.	21
1.3	Feynman diagrams of Cabibbo-favoured decays of D -mesons respectively, from the left-top side, $D^\pm \rightarrow K_S^0 \pi^\pm$, $D_s^\pm \rightarrow K_S^0 K^\pm$ and $D_s^\pm \rightarrow \phi \pi^\pm$	22
2.1	Logo for LHCb experiment, looking at the style, is clearly visible the principal aim of the experiment, the study of CP violating systems. . . .	23
2.2	Experiments along the LHC ring	25
2.3	Scheme representing the CERN injection complex, with all the accelerator mechanism such as the LINACS, PBS, PS, SPS.	26
2.4	Design of LHCb detector. The right-handed coordinate system adopted has the z -axis along the beam, and the y one along the vertical. From the left side are visible all the sub-detectors that made the detector: VELO, RICH1, TT, Magnet, Trackers, RICH2, ECAL, HCAL, Muon detectors (composed by MWPC).	28
2.5	Cross section in the (x, z) plane of the VELO silicon sensors. On the top the fully-close mode. Below the frontal view in two configurational mode fully-closed and open.	29
2.6	Sketch illustrating the $r\phi$ geometry of the VELO sensors. The different arrangement of the bonding pads leads to the slightly larger radius of the R -sensor; the sensitive area is identical.	30
2.7	Layout of the third TT detection layer. Different readout sectors are indicated by different shadings	32
2.8	The inner Tracker layout	32
2.9	Cross section of a straw-tubes module (left) and its design (right).	33

2.10	Sketch illustrating the various track types: long, VELO, upstream, downstream and T tracks. For reference the main B-field component (B_y) is plotted above as a function of the z coordinate [41].	35
2.11	Left: schematic view of the RICH1 sub-detector [34]. The Cherenkov light is emitted with different angles from the Aerogel (yellow) and the C_4F_{10} (light blue) radiators. Right: schematic view of the RICH2 sub-detector, filled with CF_4 gas [34].	37
2.12	Cherenkov angles as a function of momentum for different particle species and for the three different values of the refractive index n corresponding to the three radiator materials used in the RICH setup [44].	38
2.13	Signal deposited on the different parts of the calorimeter by an electron, a hadron and a photon [34].	40
2.14	Left: representation of an ECAL module during the assembly phase. The lead/scintillator layers are clearly visible. Right: representation of an assembled ECAL module. The green lines connected to an end are the WLS fibers connecting the calorimeter to the photomultipliers [45]. . . .	41
2.15	Lateral view of the muon detector. The first muon station M1 is placed before the calorimeters while the other stations are placed at the end of the LHCb detector [46].	43
3.1	Distribution of the TIP for the $D_{(s)}^+ \rightarrow K_s^0 \pi^+$ candidates reconstructed in a subsample of 2018 magnet-down data as example of. Vertical dashed lines show the boundaries set to reject secondary $D_{(s)}^+$ mesons derived from beauty-hadrons.	54
3.2	Distributions of the raw asymmetries in the (left) (p_x, p) plane and (right) (p_x, p_z) plane of the bachelor hadron, separately for (top) $D_{(s)}^+ \rightarrow K_s^0 \pi^+$ and (bottom) $D_{(s)}^+ \rightarrow \phi \pi^+$ candidates reconstructed in a subsample of 2018 magnet-down data as an example. The black lines show the boundaries of the large asymmetry regions which are excluded by the fiducial cuts.	55
3.3	Distribution of signed radial distance, R_{xy} , for D^0 decay vertices. The visible structures are due to secondary interaction with the RF-foil and to the VELO layers. The red line represents the requirement applied, $ R_{xy} < 5$ mm.	56
3.4	Mass invariant plot with highlighted the signals regions and sidebands utilized for the TMVA analysis.	58

3.5	(Top) Neural-network output distribution, separately for $D^+ \rightarrow K_s^0\pi^+$ signal and background and for training and testing samples. (Bottom) $S/\sqrt{S+B}$ vs neural network output of the $D_s^+ \rightarrow K_s^0\pi^+$ decay. The maximum of the function is at 0.75.	59
3.6	BTDG distribution and the BTDG average value (black line) as a function of $M(K_s^0\pi^+)$ for $D_{(s)}^\pm \rightarrow K_s^0\pi^+$	60
3.7	Signal and background distributions of the input variables chosen for the MVA selection in the $D_{(s)}^\pm \rightarrow K_s^0\pi^\pm$ sample. The definition of the variables are reported in Table 3.5.	61
3.8	Linear correlation matrix of the input variables chosen for the MVA selection in the $D_S^\pm \rightarrow K_S^0\pi^+$ sample. The 2018 sample is here reported. The definition of the variables are reported in Table 3.5.	62
3.9	$K_s^0\pi^\pm$ invariant mass distribution as a function of the daughters particles momentum imbalance, before (top) and after (bottom) the MVA selection. The black dashed line represents the $\Lambda_c \rightarrow K_s^0p$ decay where the proton is misidentified as a pion. The green one, instead, represents the $\Lambda_c^\pm \rightarrow \Lambda^0\pi^\pm$ decay where $\Lambda^0 \rightarrow p\pi^\pm$ decay is wrongly identified as a K_s^0 decay. These lines are calculated on the hypothesis of perfect invariant mass resolution model. It is here reported the sample of 2018 with magnet down polarity, as an example.	64
3.10	$\phi\pi$ -mass invariant mass distribution as a function of the momentum imbalance after the offline selection. The horizontal regions with high population represent the $D_{(s)}^\pm$ signal events.	66
3.11	Invariant mass distribution of $D_s^+ \rightarrow \phi\pi^+$ (left) and $D^+ \rightarrow K_s^0\pi^+$ (right) simulated data with the result of the fit overlaid. The data sample corresponds to 22 and 9 million of events, respectively.	68
3.12	$D_{(s)}^+ \rightarrow \phi\pi^+$ invariant mass distributions with the results of the fit overlaid for the for the $D_{(s)}^+$ (left) and $D_{(s)}^-$ (right) candidates. The bottom figures residuals between data and the fitted function.	71
3.13	$D_{(s)}^+ \rightarrow K_s^0\pi^+$ invariant mass distributions with the results of the fit overlaid for the for the $D_{(s)}^+$ (left) and $D_{(s)}^-$ (right) candidates. The bottom figures residuals between data and the fitted function.	72
3.14	$D_{(s)}^\pm \rightarrow \phi\pi^+$ (left) and $D_{(s)}^\pm \rightarrow K_s^0\pi^+$ (right) raw asymmetries as a function of the invariant mass.	73

3.15 Comparison of the momentum distribution (top-left) of D^+ and (top-right) π in $D^+ \rightarrow \phi\pi^+$ CS decay and $D^+ \rightarrow K_s^0\pi^+$ CF decay (bottom-left) and for D_s^+ and (bottom-right) π in $D_s^+ \rightarrow \phi\pi^+$ CF decay and $D_s^+ \rightarrow K_s^0\pi^+$ CS decay.	76
--	----

List of Tables

1.1	Quantum numbers of leptons and quarks	10
1.2	Summary of previous measurements of CP -violating asymmetries in $D_{(s)}^\pm \rightarrow K_S^0 h^\pm$ and $D^\pm \rightarrow \phi \pi^\pm$ decays. The errors correspond to statistical and systematic uncertainties	20
3.1	Online trigger requirements utilized to select $D_{(s)}^+ \rightarrow K_S^0 h^+$ decays.	52
3.2	Online trigger requirements utilized to select $D_{(s)}^+ \rightarrow K^+ K^- \pi^+$ decays.	53
3.3	Offline selection for $D_{(s)}^\pm \rightarrow K_S^0 \pi^\pm$	57
3.4	variables used as input for the MVA training ordered by their separation power.	60
3.5	Offline selection for the $D_{(s)}^\pm \rightarrow \phi \pi^\pm$ decay.	65
3.6	Shape parameters determined from the study of MC data events for the $D_s^+ \rightarrow \phi \pi$ and $D^+ \rightarrow K_S^0 \pi$ decays.	68
3.7	$D_{(s)}^\pm \rightarrow V^0 h^+$ signal yields obtained as result of the fits.	70
3.8	$D_{(s)}^\pm \rightarrow V^0 h^+$ raw asymmetries obtained from fits.	70
3.9	Blinded value of A_{CP}	74

Bibliography

- [1] A. et al., “Observation of CP violation in charm decays,” vol. 122, p. 211803. 12 p, Mar 2019. All figures and tables, along with any supplementary material and additional information, are available at <https://lhcbproject.web.cern.ch/lhcbproject/Publications/p/LHCb-PAPER-2019-006.html>.
- [2] D. G. Hitlin, “First CP violation results from BaBar,” in *High energy physics. Proceedings, 30th International Conference, ICHEP 2000, Osaka, Japan, July 27-August 2, 2000. Vol. 1, 2*, pp. 3–20, 2000.
- [3] M. S. Sozzi, “Discrete Symmetries and CP violation,” 2008.
- [4] A. Salam, “Weak and electromagnetic interactions,” in *Elementary Particle Theory* (W. Svartholm, ed.), (Stockholm), p. 367, Almquist and Wiksell, 1968.
- [5] N. Cabibbo, “Unitary symmetry and leptonic decays,” *Phys. Rev. Lett.*, vol. 10, pp. 531–533, Jun 1963.
- [6] D. J. Griffiths, *Introduction to elementary particles; 2nd rev. version*. Physics textbook, New York, NY: Wiley, 2008.
- [7] M. Kobayashi and T. Maskawa, “ CP Violation in the Renormalizable Theory of Weak Interaction,” *Prog. Theor. Phys.*, vol. 49, pp. 652–657, 1973.
- [8] G. S. Abrams *et al.*, “The Discovery of a Second Narrow Resonance in e^+e^- Annihilation,” *Phys. Rev. Lett.*, vol. 33, pp. 1453–1455, 1974. [Adv. Exp. Phys.5,150(1976)].
- [9] J. J. Aubert, U. Becker, P. J. Biggs, J. Burger, M. Chen, G. Everhart, P. Goldhagen, J. Leong, T. McCorrison, T. G. Rhoades, M. Rohde, S. C. C. Ting, S. L. Wu, and Y. Y. Lee, “Experimental observation of a heavy particle j ,” *Phys. Rev. Lett.*, vol. 33, pp. 1404–1406, Dec 1974.

- [10] S. W. Herb *et al.*, “Observation of a Dimuon Resonance at 9.5-GeV in 400-GeV Proton-Nucleus Collisions,” *Phys. Rev. Lett.*, vol. 39, pp. 252–255, 1977.
- [11] F. Abe *et al.*, “Observation of top quark production in $\bar{p}p$ collisions,” *Phys. Rev. Lett.*, vol. 74, pp. 2626–2631, 1995.
- [12] H. Albrecht *et al.*, “Observation of B0 - anti-B0 Mixing,” *Phys. Lett.*, vol. B192, pp. 245–252, 1987. [,51(1987)].
- [13] R. Aaij *et al.*, “Measurement of matter-antimatter differences in beauty baryon decays,” *Nature Phys.*, vol. 13, pp. 391–396, 2017.
- [14] P. W. Higgs, “Broken Symmetries and the Masses of Gauge Bosons,” *Phys. Rev. Lett.*, vol. 13, pp. 508–509, 1964. [,160(1964)].
- [15] F. Englert and R. Brout, “Broken Symmetry and the Mass of Gauge Vector Mesons,” *Phys. Rev. Lett.*, vol. 13, pp. 321–323, 1964. [,157(1964)].
- [16] C. Patrignani *et al.*, “Review of Particle Physics,” *Chin. Phys.*, vol. C40, no. 10, p. 100001, 2016.
- [17] L. Wolfenstein, “Parametrization of the Kobayashi-Maskawa Matrix,” *Phys. Rev. Lett.*, vol. 51, p. 1945, 1983.
- [18] S. L. Glashow, J. Iliopoulos, and L. Maiani, “Weak Interactions with Lepton-Hadron Symmetry,” *Phys. Rev.*, vol. D2, pp. 1285–1292, 1970.
- [19] S. Bianco, F. L. Fabbri, D. Benson, and I. , “A Cicerone for the physics of charm,” *Riv. Nuovo Cim.*, vol. 26N7, pp. 1–200, 2003.
- [20] I. I. Y. Bigi and H. Yamamoto, “Interference between Cabibbo allowed and doubly forbidden transitions in $D \rightarrow K_S, K_L + \pi$ ’s decays,” *Phys. Lett.*, vol. B349, pp. 363–366, 1995.
- [21] A. Abba, F. Bedeschi, M. Citterio, F. Caponio, A. Cusimano, A. Geraci, F. Lionetto, P. Marino, M. J. Morello, N. Neri, D. Ninci, A. Piucci, M. Petruzzo, G. Punzi, F. Spinella, S. Stracka, D. Tonelli, and J. Walsh, “A specialized track processor for the LHCb upgrade,” Tech. Rep. LHCb-PUB-2014-026. CERN-LHCb-PUB-2014-026, CERN, Geneva, Mar 2014.
- [22] R. Aaij *et al.*, “Observation of CP violation in charm decays,” 2019.

- [23] B. Aubert *et al.*, “Evidence for $D^0 - \bar{D}^0$ Mixing,” *Phys. Rev. Lett.*, vol. 98, p. 211802, 2007.
- [24] M. Staric *et al.*, “Search for CP Violation in D^\pm Meson Decays to $\phi\pi^\pm$,” *Phys. Rev. Lett.*, vol. 108, p. 071801, 2012.
- [25] Y. Amhis *et al.*, “Averages of b -hadron, c -hadron, and τ -lepton properties as of summer 2016,” *Eur. Phys. J.*, vol. C77, no. 12, p. 895, 2017.
- [26] H. Mendez *et al.*, “Measurements of D Meson Decays to Two Pseudoscalar Mesons,” *Phys. Rev.*, vol. D81, p. 052013, 2010.
- [27] J. P. Lees *et al.*, “Search for CP violation in the Decays $D^\pm \rightarrow K_S^0 K^\pm$, $D_s^\pm \rightarrow K_S^0 K^\pm$, and $D_s^\pm \rightarrow K_S^0 \pi^\pm$,” *Phys. Rev.*, vol. D87, no. 5, p. 052012, 2013.
- [28] J. P. Lees *et al.*, “Search for direct CP violation in singly Cabibbo-suppressed $D^\pm \rightarrow K^+ K^- \pi^\pm$ decays,” *Phys. Rev.*, vol. D87, no. 5, p. 052010, 2013.
- [29] B. R. Ko *et al.*, “Search for CP violation in the decays $D_{(s)}^+ \rightarrow K_S^0 \pi^+$ and $D_{(s)}^+ \rightarrow K_S^0 K^+$,” *Phys. Rev. Lett.*, vol. 104, p. 181602, 2010.
- [30] B. R. Ko *et al.*, “Search for CP Violation in the Decay $D^+ \rightarrow K_S^0 K^+$,” *JHEP*, vol. 02, p. 098, 2013.
- [31] R. Aaij *et al.*, “Search for CP violation in $D^+ \rightarrow \phi\pi^+$ and $D_s^+ \rightarrow K_S\pi^+$ decays,” *JHEP*, vol. 06, p. 112, 2013.
- [32] R. Aaij *et al.*, “Search for CP violation in $D^\pm \rightarrow K_S^0 K^\pm$ and $D_s^\pm \rightarrow K_S^0 \pi^\pm$ decays,” *JHEP*, vol. 10, p. 025, 2014.
- [33] R. e. A. Aaij, “Search for cp violation in $D_s^+ \rightarrow K_S^0 \pi^+$, $D^+ \rightarrow K_S^0 K^+$, and $D^+ \rightarrow \phi\pi^+$ decays,” *Phys. Rev. Lett.*, vol. 122, p. 191803, May 2019.
- [34] A. A. Alves, Jr. *et al.*, “The LHCb Detector at the LHC,” *JINST*, vol. 3, p. S08005, 2008.
- [35] L. Evans, “The large hadron collider,” *New Journal of Physics*, vol. 9, no. 9, p. 335, 2007.
- [36] R. Aaij *et al.*, “Measurement of the b -quark production cross section in 7 and 13 tev pp collisions,” *Phys. Rev. Lett.*, vol. 118, p. 052002, Feb 2017.
- [37] L. Evans and P. Bryant, “LHC Machine,” *JINST*, vol. 3, p. S08001, 2008.

- [38] P. R. Barbosa-Marinho *et al.*, *LHCb VELO (VERtex LOcator): Technical Design Report*. Technical Design Report LHCb, Geneva: CERN, 2001.
- [39] P. R. Barbosa-Marinho *et al.*, *LHCb inner tracker: Technical Design Report*. Technical Design Report LHCb, Geneva: CERN, 2002. revised version number 1 submitted on 2002-11-13 14:14:34.
- [40] *LHCb : Technical Proposal*. Tech. Proposal, Geneva: CERN, 1998.
- [41] R. Aaij *et al.*, “LHCb Detector Performance,” *Int. J. Mod. Phys.*, vol. A30, no. 07, p. 1530022, 2015.
- [42] R. Fruhwirth, “Application of Kalman filtering to track and vertex fitting,” *Nucl. Instrum. Meth.*, vol. A262, pp. 444–450, 1987.
- [43] A. Papanestis and C. D’Ambrosio, “Performance of the LHCb RICH detectors during the LHC Run II. Performance of the LHCb RICH detectors during the LHC Run II,” Tech. Rep. LHCb-PUB-2017-012. CERN-LHCb-PUB-2017-012, CERN, Geneva, Mar 2017. Updated authors’ details and DOI.
- [44] C. Lippmann, “Particle identification,” *Nucl. Instrum. Meth.*, vol. A666, pp. 148–172, 2012.
- [45] S. Amato *et al.*, *LHCb calorimeters: Technical Design Report*. Technical Design Report LHCb, Geneva: CERN, 2000.
- [46] A. A. Alves, Jr. *et al.*, “Performance of the LHCb muon system,” *JINST*, vol. 8, p. P02022, 2013.
- [47] S. Benson, V. V. Gligorov, M. A. Vesterinen, and J. M. Williams, “The LHCb Turbo Stream,” *J. Phys. Conf. Ser.*, vol. 664, no. 8, p. 082004, 2015.
- [48] R. e. A. Aaij, “Evidence for cp violation in time-integrated $D^0 \rightarrow h^- h^+$ decay rates,” *Phys. Rev. Lett.*, vol. 108, p. 111602, Mar 2012.
- [49] A. et Al., “Search for CP violation in $D_s^+ \rightarrow K_S^0 \pi^+$, $D^+ \rightarrow K_S^0 K^+$ and $D^+ \rightarrow \phi \pi^+$ decays,” *Phys. Rev. Lett.*, vol. 122, p. 191803. 11 p, Mar 2019. All figures and tables, along with any supplementary material and additional information, are available at <https://cern.ch/lhcbproject/Publications/p/LHCb-PAPER-2019-002.html>.

Ringraziamenti

Vorrei ringraziare per essermi stati vicino durante questo lavoro di tesi i miei familiari, Annalisa, Stefano, Barbara e Filippo, che senza di loro non avrei percorso questa strada e che mi hanno supportato durante tutti i deliri del caso. Vorrei ringraziare Greta, la mia metà, che mi ha supportato e sopportato per tutto il mio viaggio culturale e con la quale condivido tutti i momenti, belli e brutti. I miei coinquilini magnifici che mi hanno in casa tutto il giorno e che con loro non ci si annoia mai, neanche durante lo studio, William, Paolo, Walid, Giro, Corrado e Ale. La *Band of Physicists* composta dai miei coinquilini, più Matteo e Francesco che sono sempre presente nel mio cuore. Ai miei colleghi di corso con cui ho passato dei bellissimi momenti, soprattutto a Cargese. Per ultimi, ma non ultimi, vorrei ringraziare il Professor Angelo Carbone con il quale ho passato momenti deliranti e di pura follia, ma pieni di insegnamenti e la Dott.ssa Serena che senza di lei oggi probabilmente non sarei qui. Infine vorrei menzionare anche tutto il gruppo LHCb-Bologna, sono dei ragazzi meravigliosi e spero in un futuro di poterli lavorare ancora.